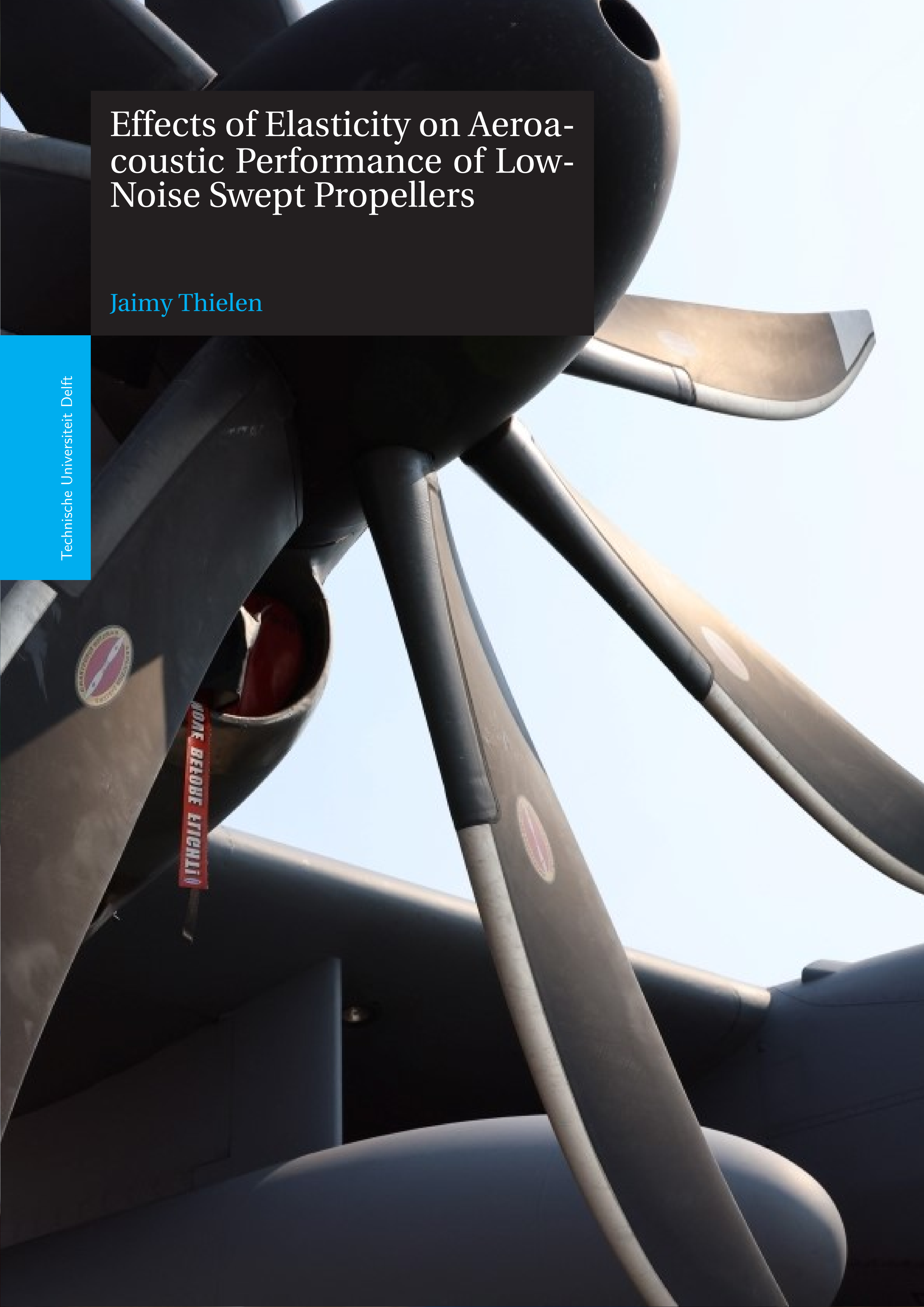

Effects of Elasticity on Aeroacoustic Performance of Low-Noise Swept Propellers

Jaimy Thielen

Technische Universiteit Delft

Effects of Elasticity on Aeroacoustic Performance of Low-Noise Swept Propellers

by

Jaimy Thielen

in partial fulfillment of the requirements for the degree of

Master of Science
in Aerospace Engineering

at the Delft University of Technology,
to be defended publicly on Thursday May 16, 2024 at 13:00.

Chairman:	Prof. dr. ing. G. Eitelburg,	TU Delft
Supervisor:	Dr.ir. T. Sinnige,	TU Delft
Thesis committee:	Dr. ir. J. Sodja,	TU Delft
	Dr. R. Merino Martinez,	TU Delft

Preface

This thesis is the result of a year of hard work during which I have been able to apply all that I have learned during my time in Delft. I'd like to thank my supervisors, Georg Eitelberg and Tomas Sinnige, for their continued support and guidance throughout the entire process. I would also like to thank Gabriel Margalida and all the other people at the FPP department, who assisted me with the models and data I used for this research.

Finishing this thesis also marks the end of my studies in Delft, which I can look back on fondly. I am grateful for everything I learned and the friends I made along the way. I now look forward to what the future entails.

Jaimy Thielen
Delft, April 2024

Abstract

The aviation industry requires continuous reductions in greenhouse gas and noise emissions, which is resulting in a shift towards hybrid and fully electric aircraft. The propeller is an attractive form of propulsion system for electric aircraft as it can achieve high efficiencies and has excellent scalability potential. However, a major concern is the high community and cabin noise levels. It is possible to mitigate the propeller noise levels by reducing the blade loading and shifting the loading inboard, though this will often adversely impact the aerodynamic efficiency. Another method of reducing noise is by introducing blade sweep. This can result in destructive interference of sound waves. The downside is that sweep may impose significant structural deformations when the blade is loaded. These structural deformations may alter both the aerodynamic and acoustic performance. The objective of this thesis is to identify how these structural deformations will impact the aerodynamic and acoustic performance of low-noise, swept propeller blades. A parametric study was performed where the blade sweep was parametrised. The aerodynamic, acoustic and structural performances of these propeller configurations were then analysed to identify the relations between these three disciplines.

A multidisciplinary propeller framework was used where aerodynamic, acoustic and structural tools could be coupled. For the aerodynamic analyses, a Vortex Lattice tool was developed, which can perform inviscid, incompressible simulations of any propeller geometry. The acoustics were calculated using Hanson's Helicoidal Surface Theory, which models the blade sweep and dihedral as phase lag effects to model the interference between sound waves. The structural tool used the Euler-Bernoulli beam theory for bending deformations and Saint-Venant's torsion theory for twisting deflections. These three tools were coupled such that the final deformed shape of a loaded propeller could be obtained and evaluated. Each tool was validated individually using high-fidelity and experimental data, confirming that accurate results may be obtained within the tool's applicable limitations.

The elastic blades were compared to their rigid counterparts to analyse how much the blade deformed, and how these deformations impacted the aerodynamic and acoustic performance. It was found that bending deformations are caused by the centrifugal forces, opposing any bending moments caused by the aerodynamic forces. The torsional deformations, mainly caused by the aerodynamic forces, result in a wash-out. Both the bending deformations and wash-out of the blade reduce the local angle of attack, reducing the aerodynamic loads acting on the propeller blades. Since these structural deformations are concentrated near the blade tip, the local loading distributions are only impacted near the tip. This effectively shifts the loading inboard. The loss in performance can be significant if substantial sweep is applied, with losses of up to 20% of the thrust and torque. The efficiency, on the other hand, does not significantly change due to elasticity. The acoustic performance was mainly altered due to the changes in aerodynamic performance, with any changes in blade geometry having negligible effects. The overall sound pressure levels reduce by up to 2.5 dB, correlating with the reduction in thrust and torque. By eliminating the noise's dependency on the overall thrust level, a clear correlation between the shifting of the local loading and the noise emissions was also found. These inboard shifting loads reduced the thrust-specific sound pressure by up to 1 dB.

It is possible to reduce the effect of elasticity by letting the structural forces impose a twisting moment, reducing the wash-out of the propeller blades. High bending deformations, or the addition of dihedral, allow the moment arm of the centrifugal loads to grow enough such that the twisting moments of the aerodynamic forces can be overcome. This can greatly diminish the aerodynamic performance loss. On the other hand, the associated increase of the peakiness of the local aerodynamic loading distributions may increase the noise emissions even when a net loss in aerodynamic performance is still present.

Clear relations between the aerodynamic, acoustic, and structural performance of elastic, swept blades were identified. These changes in aerodynamics and acoustics are too great to be ignored for highly swept blades. Analyses of such flexible, highly swept blades clearly require the inclusion of structural calculations to accurately predict the aerodynamic and acoustic performance.

CONTENTS

Nomenclature

Symbols

Since some symbols may overlap, the context of each symbol is provided: AE=Aerodynamics, AC=Acoustics, ST=Structures, PD=Propeller Design.

Symbol	Context	Definition	Unit
A_L	ST	Cross-sectional area of the blade along the local coordinate system	[m^2]
A_{conv}	AE	Wake axial velocity coefficient	[-]
A_{expan}	AE	Wake axial acceleration coefficient	[-]
a	AE	Vortex influence coefficient	[-]
B	PD	Number of blades	[-]
B_D	PD	Chord to diameter ratio	[-]
BN	AC	Blade passage frequency	[Hz]
b	AE	Influence coefficient of the trailing vortices	[-]
C_D	AE	Drag coefficient	[-]
$\overline{C}_f$	AE	Maximum force of the normalised local load distribution	[-]
C_L	AE	Lift coefficient	[-]
C_P	AE	Power coefficient	[-]
C_Q	AE	Torque coefficient	[-]
C_T	AE	Thrust coefficient	[-]
c/R	PD	Chord to radius ratio	[-]
c_0	AC	Speed of sound	[m/s]
D	AE	Drag	[N]
D	PD	Propeller diameter	[m]
dl	AE	Panel length vector	[m]
dt	AE	Time step	[s]
dV	ST	Blade section volume	[m^3]
E	ST	Elastic Modulus	[Pa]
$\boldsymbol{e}_x, \boldsymbol{e}_y, \boldsymbol{e}_z$	PD	Global coordinate system	[-]
$\boldsymbol{e}_\xi, \boldsymbol{e}_\eta, \boldsymbol{e}_\zeta$	ST	Local blade coordinate system	[-]
$\boldsymbol{e}_r$	ST	Radial vector	[-]
F_x, F_z	ST	Load applied at the tip in x- or z-direction	[N]
FA	AC	Face Alignment	[m]
f_i	AC	Frequency of the acoustic pressure	[Hz]
f_q	AC	Normalised chordwise torque distribution	[-]
f_t	AC	Normalised chordwise thrust distribution	[-]
G	ST	Shear modulus	[Pa]
H	AC	Normalised chordwise thickness distribution	[-]
I	ST	Moment of inertia	[m^4]
i	AC	Imaginary unit	[-]
J	AE	Advance ratio	[-]
J_{mB}	AC	Radiation efficiency factor	[-]
k_x	AC	Chordwise wave number	[-]
L	AE	Lift	[N]
l	ST	Total blade arc length	[m]
M	AE	Mach number	[-]
$\boldsymbol{M}$	ST	Total internal moment	[Nm]
M_ξ	ST	Torsional moment along blade axis	[Nm]
M_ζ	ST	Bending moment along major principal axis of cross section	[Nm]

Symbol	Context	Definition	Unit
M_η	ST	Bending moment along minor principal axis of cross section	[Nm]
$\boldsymbol{M}_a$	ST	Internal moment due to aerodynamic forces	[Nm]
$\boldsymbol{M}_c$	ST	Internal moment due to centrifugal forces	[Nm]
M_r	AC	Section relative Mach number	[-]
M_t	AC	Tip rotational Mach number	[-]
M_x	AC	Flight Mach number	[-]
MCA	AC	Mid-chord alignment	[m]
N_c	PD	Number of chordwise panels	[-]
N_s	PD	Number of spanwise panels	[-]
N_w	AE	Number of wake panel rows	[-]
N_b	PD	Number of blades	[-]
n	PD	Propeller rotational speed	[rad/s]
$\boldsymbol{n}$	AE	Vortex ring panel normal vector	[-]
OSPL	AC	Overall Sound Pressure Level	[dB]
P_{Dm}	AC	Complex Fourier coefficient of the drag pressure at mth harmonic	[-]
P_{Lm}	AC	Complex Fourier coefficient of the lift pressure at mth harmonic	[-]
P_{Qm}	AC	Complex Fourier coefficient of the torque pressure at mth harmonic	[-]
P_{Tm}	AC	Complex Fourier coefficient of the thrust pressure at mth harmonic	[-]
P_{Vm}	AC	Complex Fourier coefficient of the thickness pressure at mth harmonic	[-]
P_{mN_B}	AC	Complex Fourier coefficient of the total pressure at mth harmonic	[-]
p	PD	Maximum camber position	[-]
p	AC	Pressure	[Pa]
p_{ref}	AC	Reference pressure of human hearing threshold	[Pa]
p_{rms}	AC	Root-mean-square of the pressure waves	[Pa]
Q	AE	Torque	[Nm]
q	AE	Induced velocity	[m/s]
$\boldsymbol{q}_a$	ST	Loading due to aerodynamic forces	[N/m]
$\boldsymbol{q}_c$	ST	Loading due to centrifugal forces	[N/m]
q_Q	ST	Loading due to torque forces	[N/m]
q_T	ST	Loading due to thrust forces	[N/m]
R	PD	Propeller tip radius	[m]
R_h	PD	Propeller hub radius	[m]
r	AE+AC+ST	Propeller local radius parameter	[m]
$\boldsymbol{r}_a$	ST	Centre of pressure vector	[-]
$\boldsymbol{r}_q$	ST	Centre of gravity vector	[-]
s	ST	Local arc length parameter	[m]
T	AE	Thrust	[N]
$TSSP$	AC	Thrust-Specific Sound Pressure	[dB]
t	AC	Time	[s]
t/c	PD	Thickness to chord ratio	[-]
U_Ω	AE	Rotational velocity	[m/s]
U_∞	AE	Freestream velocity	[m/s]
u	AE	x-component of the velocity	[m/s]
v	AE	y-component of the velocity	[m/s]
w	AE	z-component of the velocity	[m/s]
w_{ind}	AE	Induced downwash	[m/s]
x, y, z	PD	Coordinates along the global coordinate system	[m]
y_o	AC	Observer distance	[m]
α	AE	Angle of attack	[deg]
α_d	ST	Relaxation factor for the rotational speed	[-]
α_d	ST	Relaxation factor for the structural deformations	[-]
β	AE+ST	Twist angle	[deg]
$\beta_{0.7R}$	AE+ST	Pitch angle at 70% radius	[deg]
β_L	ST	Local twist angle along the local coordinate system	[deg]

Symbol	Context	Definition	Unit
Γ	AE	Vortex strength	[-]
δ	ST	Total bending deflection at the tip	[m]
η	AE	Aerodynamic efficiency	[-]
θ	AC	Axial directivity angle	[rad]
κ	PD	Parameter for forward sweep between the root and tip	[-]
Λ	PD	Parameter for the amount of tip sweep	[-]
$d\Lambda$	PD	Parameter for the sweep curvature	[-]
ξ,ζ,η	ST	Coordinates along the local coordinate system	[m]
ρ	AE+AC	Air density	[kg/m^3]
ρ_b	ST	Material density	[kg/m^3]
$1\rho_\zeta$	ST	Blade curvature along major principal axis	[-]
$1\rho_\eta$	ST	Blade curvature along minor principal axis	[-]
σ	ST	Bending stress	[Pa]
σ_{VM}	ST	Von Mises stress	[Pa]
σ_{yield}	ST	Yield stress of the material	[Pa]
τ	ST	Shear stress	[Pa]
Φ_V	AC	Fourier source transform of thickness noise	[-]
Φ_Q	AC	Fourier source transform of torque noise	[-]
Φ_T	AC	Fourier source transform of thrust noise	[-]
ϕ_o	AC	Phase lag due to dihedral	[-]
ϕ_s	AC	Phase lag due to sweep	[-]
ψ	AE	Inflow angle	[deg]
Ω	PD	Propeller rotational speed	[rad/s]

SUBSCRIPTS & SUPERSCRIPTS

Subscript / Superscript	Definition
CoP	Radial centre of pressure
$elastic$	Elastic blade performance quantity
$fine$	Solution with very fine panel and wake grid
i,j	Vortex panel position indicator
K,L	Vortex panel index counter
$rigid$	Rigid blade performance quantity
$straight$	Straight blade performance quantity
$swept$	Swept blade performance quantity
tip	Quantity measured at the blade tip

ABBREVIATIONS

Abbreviation	Definition
BB	Backwards-swept blade
BEM	Blade Element Momentum
CFD	Computational Fluid Dynamics
EB	Euler-Bernoulli
FA	Face Alignment
FB	Forwards-swept blade
FEM	Finite Element Modelling
HST	Helicoidal Surface Theory
LBM	Lattice Boltzmann Method
LLT	Lifting Line Theory
LST	Lifting Surface Theory
MCA	Mid-Chord Alignment
OSPL	Overall Sound Pressure Level
PCA	Pitch Change Axis
RANS	Reynolds-Averaged Navier-Stokes
SB	Straight blade
SPL	Sound Pressure Level
TSSP	Thrust-Specific Sound Pressure
VLM	Vortex Lattice Method

List of Figures

List of Tables

I

Background

1 Introduction

The propeller is experiencing a resurgence in interest as the aviation industry strives to adopt more environmentally sustainable technologies [1]. Their high efficiency and scalability are proving to be invaluable to future aircraft concepts. Yet there is still one significant problem restricting the application of propellers: noise emissions. These noise emissions pose a significant environmental and financial challenge. Excessive exposure to noise emissions may pose short- and long-term health complications [2]. Increasing airport noise charges make it financially nonviable for airliners to operate loud aircraft [3]. Society and the aviation industry have evolving needs that require new innovations.

The main sources of propeller noise emissions are the displacement of air as the propeller spins, and the pressure fluctuations generated on the surface. It has been long known that these sources of noise can be reduced using geometrical modifications, resulting in low-noise propellers [4]. Such low-noise propellers are characterised by having a high number (>6) of thin, swept blades [4]. Nevertheless, it has been challenging to implement such complex propeller configurations thus far. Any noise savings often comes at the cost of aerodynamic efficiency. Furthermore, structural constraints may significantly impose upon the suitable geometrical shape of low-noise propellers [4]. The design and analysis of low-noise propellers thus requires detailed aerodynamic, acoustic and structural modelling, making it a multidisciplinary problem.

Significant numerical and experimental research is ongoing to obtain propeller blade shapes that can reduce noise emissions without imposing on the aerodynamic efficiency. These studies use various techniques to model the aerodynamics, acoustics and structures. Nevertheless, there is a lack of research on the effects of structural deformations on the performance of low-noise propeller designs. While these structural deformations are often included in the optimisation schemes, the effects of elasticity are not explicitly analysed.

This thesis aims to investigate the effects of structural deformations on the aerodynamic and acoustic performance of low-noise propellers by means of a parametric study. Aerodynamic, acoustic and structural tools will be coupled in a propeller framework to allow for the analysis of a broad set of propeller geometries over a range of operating conditions. The aerodynamics, acoustics and structural results are then examined in detail to identify the underlying mechanics. While recent studies by Bergmann et al. [5, 6, 7] do address the influence of elasticity on swept propeller blades, only a single sweep distribution is applied. In this study, the amount of sweep, and how this sweep is distributed, is varied to showcase the trends in aeroacoustic and structural performance.

In the remainder of this chapter, state-of-the-art research on low-noise propeller is highlighted in Section 1.1. The objectives and main research questions of this thesis are formulated in Section 1.2. Finally, the overall structure of this report is explained in Section 1.3.

1.1. PROPELLER ACOUSTIC OPTIMISATION

Current research regarding propeller acoustics often consists of propeller geometry optimisation. Many papers can be found with varying degrees of modelling fidelity and optimisation criteria. This section highlights the results obtained in some of these papers.

Geng et al. [8, 9] wrote multiple papers on the rigid acoustic optimisation of the propeller blade geometry. In their first paper, Blade Element Momentum (BEM) and the Hanson Helicoidal Surface Theory (HST) were used to optimise the sweep distribution between the root and tip [8]. The goal was to achieve wave interference due to sweep lag without compromising on the aerodynamic efficiency. They found a 2.9 dB noise reduction while maintaining the aerodynamic efficiency of the baseline design with these low-fidelity methods. The baseline and optimal design are shown in Figure 1.1. The total sweep at the tips are equal, but the optimal design has more forward sweep near the root. This subtle change in geometry is enough to obtain a 2.9 dB reduction.
In a follow-up paper by Geng et al. [9], higher fidelity methods were employed to optimise the propeller blade shape again. Operating conditions are now set to reflect those of conventional regional airliners like the ATR72. The chord and sweep distribution were set as the design variables, and the aerodynamic performance was constrained to match the baseline design. The optimised propeller design is shown in Figure 1.2. Compared to the straight baseline blades, the optimised design has a similar sweep distribution as in Figure 1.1, where the blade sweeps forward near the root and back towards the tip. The chord distribution is increased near the root and decreased near the tip to move the blade loading more inboard. With these modifications, a 1.69 dB noise reduction was achieved.

Figure 1.1: Baseline (left) and optimal (right) propeller blade design by Geng et al. - 2021 [8].

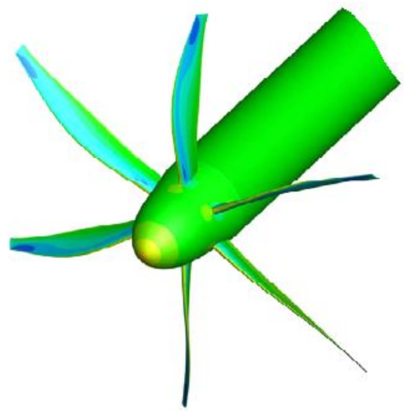

Figure 1.2: Optimal propeller design by Geng et al. - 2023 [9].

The acoustic optimisations by Marinus et al. [10, 11, 12, 13] provide an interesting insight into the effects of elasticity, as structural deformations were not included in all the optimisation results. To model the aerodynamic and acoustic performance, Reynolds-Averaged Navier-Stokes (RANS) Computational Fluid Dynamics (CFD) simulations were coupled with Farassat's acoustic Formulation 1A. High-speed propeller blades ($M_{cruise} = 0.75$) were then optimised for take-off and cruise conditions. The chord, sweep, twist and airfoil shape were all included as design variables for the optimisation. Multiple optimised blades for the rigid procedure are shown in Figure 1.3. Unswept blades (a) and (b) reduce take-off noise by approximately 4 dB and cruise noise by 10.5 dB. The swept blades (c) and (d) reduce take-off noise by approximately 1.5 dB and cruise noise by 15 dB. Clearly, there is a Pareto front in terms of reducing noise in multiple operating conditions.
The structural deformations were included in a follow-up paper by Marinus et al. [11, 12] using Computational Structural Mechanics (CSM). These elastic optimised blades are shown in Figure 1.4. The sweep at the tip has been significantly reduced compared to the rigid blades of Figure 1.3. In terms of acoustic performance, the noise emissions on average have increased for both the take-off and cruise condition. This seems to indicate an adverse effect of the structural deformations on the noise emissions. The aerodynamic efficiency in take-off conditions has also decreased significantly, from $\eta_{rigid} = 0.55$ to $\eta_{elastic} = 0.48$. In cruise conditions, there is no significant difference. The flow in which these propellers operate is highly compress-

ible. As such, the sweep is not only introduced to reduce noise emissions, but also to mitigate the effects of compressibility on the aerodynamic performance.

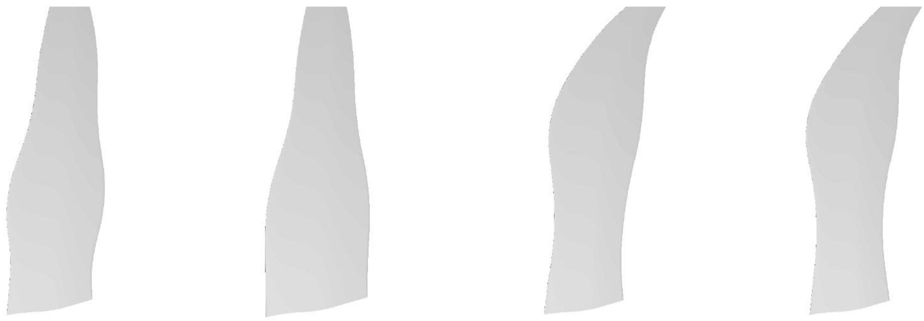

(a) (b) (c) (d)

Figure 1.3: Optimal rigid propeller blade designs by Marinus et al [10].

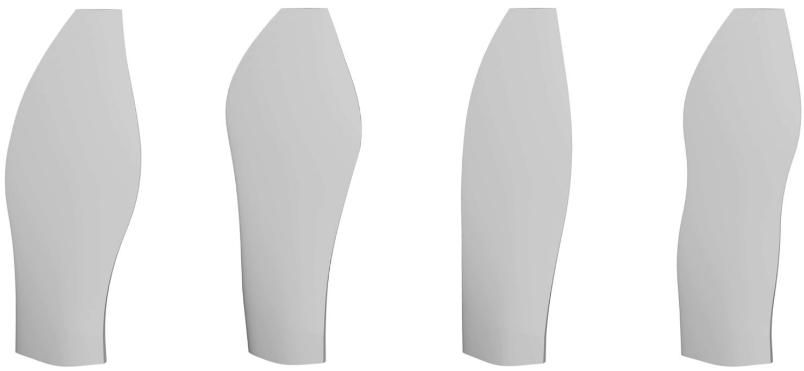

(a) A. (b) B. (c) C. (d) D.

Figure 1.4: Optimal elastic propeller designs by Marinus et al. [11].

The most advanced research on low-noise propellers is currently ongoing as part of the joint European Clean Sky 2 programme [2]. The IRON (Innovative turboROp configuratioN) project aims to significantly reduce the noise emissions of regional airliners without compromising on the aerodynamic performance. The target is a 6 dB reduction during cruise compared to a baseline design. 1:6 scaled models have already been tested in the DNW wind tunnels. These scaled models are shown in Figure 1.5 [2]. The baseline design by Dowty in Figure 1.5a shows a conventional scimitar design commonly used in current regional turboprops. Two low-noise concepts were created by CENAERO and GE AAT, shown in Figures 1.5b and 1.5c respectively. These two designs show very slender blades with a high sweep and even dihedral.
The scaled models are manufactured from titanium, chosen for its high strength-to-weight ratio. Extensive wind-tunnel testing consisted of measuring the aerodynamic, acoustic and structural performance in low and high-speed conditions. Structural deflections were measured by capturing the yellow dots on the blades with high-speed cameras [2].

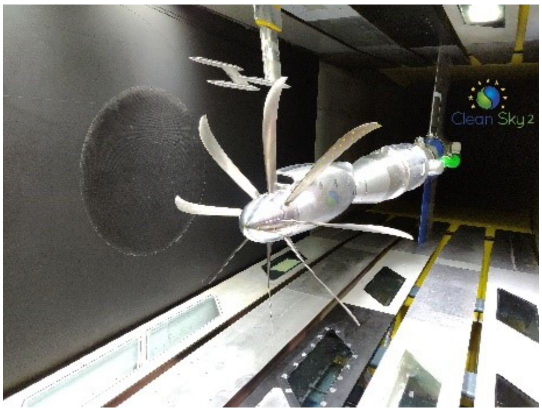

(a) Baseline design by Dowty.

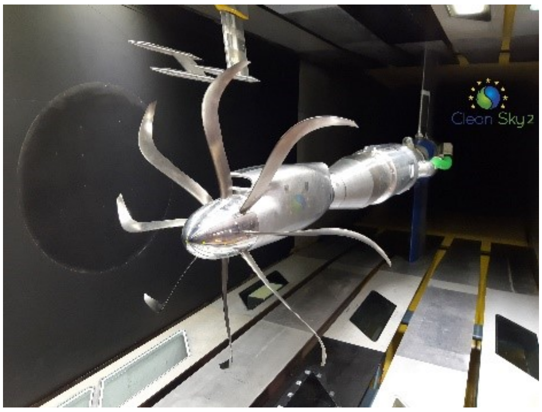

(b) 8-blade design by CENAERO.

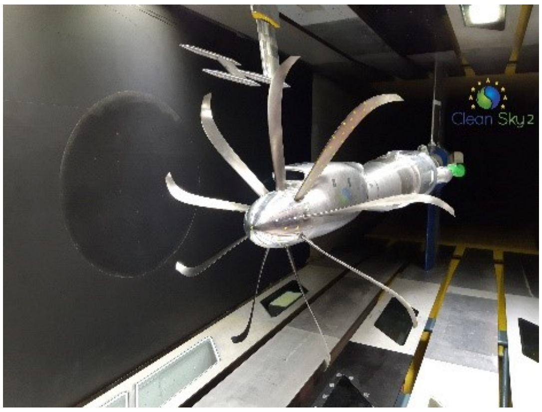

(c) 9-blade design by GE AAT Deutschland.

Figure 1.5: Next generation low-noise propeller models in the transonic wind tunnel of DNW. (from [2])

Current research has shown the potential for significant noise reductions by optimising the blade geometry. In particular, the addition of sweep may induce destructive interference of sound waves without adversely affecting the load distribution. Sweep may induce significant structural deformations, altering the aerodynamic and acoustic performance. There is currently a lack of public research on the effects of elasticity on the performance of swept propellers. Only recently has research by Bergmann et al. [5, 6, 7] come out regarding this topic. In these papers, the effects of elasticity on the aerodynamic and acoustic performance are computed for three sweep configurations. It was found that large diameter, low disc loading, and blade sweep can significantly decrease the aerodynamic performance, with a reduction of thrust up to 8%. The acoustic levels were consequently also reduced due to decreased total loading.

1.2. THESIS OBJECTIVES & RESEARCH QUESTIONS

The previous section highlighted the ongoing research on low-noise propeller optimisation, both numerically and experimentally. This is a well-established research topic with a wide variety of methodologies and applications. Nevertheless, the discipline of structures is often not included or not analysed carefully to identify the effects of structural deformations. This thesis aims to address this lack of knowledge on the effects of elasticity on low-noise propellers. The main objective of this thesis is:

To identify the effects of elasticity on the aerodynamic and acoustic performance of low-noise propellers.

Research questions have been formulated to achieve this objective. These research questions will all be answered in this report. The research questions are:

1. *How does a swept low-noise propeller blade deform when put under load?*
   (a) *How does each type of loading contribute to the structural deformations of swept low-noise propellers?*

   (b) *How does the amount of sweep affect the structural deformations of swept low-noise propellers?*
   (c) *How does the sweep distribution affect the structural deformations of swept low-noise propellers?*
   (d) *How do the structural deformations change under different operating conditions?*

2. *How do the structural deformations affect the aerodynamic and acoustic performance of swept low-noise propellers?*
   (a) *How does each type of deformation contribute to the differences between rigid and elastic aerodynamic performance?*
   (b) *What is the main contribution to the differences between rigid and elastic acoustic performance?*

3. *How does an elastic swept low-noise propeller perform compared to an elastic straight low-noise propeller?*
   (a) *How does blade sweep affect the aerodynamic and acoustic performance of rigid low-noise propellers?*
   (b) *What is the main contribution to changes in performance when comparing elastic swept and straight propellers?*

These research questions will be answered by performing a parametric study of swept propellers. The aerodynamic, acoustic and structural performance of these swept propellers are analysed carefully to identify the relations between the three disciplines. Previous studies on low-noise propellers have used a wide variety of analysis tools, ranging from low-fidelity tools to fully coupled CFD and FEM simulations. While these high-fidelity methods can predict the complex flow and structural phenomena on low-noise propeller designs, the computational costs are extremely high. The goal in this thesis is to analyse many different propeller configurations, across a range of operating conditions. The computational costs of coupled high-fidelity simulations are too high to be able to apply these methods in this thesis. Low-fidelity methods will be used to prioritise the amount of data which can be obtained, instead of focusing on the accuracy of the results.

1.3. THESIS OUTLINE

This thesis is split up into five parts. This chapter is part of Part I, where background information is provided on low-noise propellers performance and state-of-the-art research. Part II will explain the applied methodology for each of the three disciplines. The governing equations, limitations and assumptions of each tool are carefully defined. The modelling method for each discipline was chosen based on an extensive literature research performed previously. The sections of this literature research on choosing the modelling methods are included in Appendix A.

The accuracy of each tool is validated in Part III. High-fidelity and experimental data are used to compare to the results of the developed low-fidelity tools. The suitable region of conditions of each tool is identified. The parametric study set-up and results are shown in Part IV. The results are mainly outlined in the form of contour plots, showing the effect of each sweep parameter on various performance indicators. Relations between the aerodynamic, acoustic and structural performance are identified. Finally, conclusions are drawn in Part V. Limitations of this research, and potential recommendations for future research to build upon this thesis are outlined.

2

Low-Noise Propeller Performance

This chapter provides background information on the aerodynamic, acoustic and structural mechanics of propellers. Special attention is given to any unique characteristics of low-noise, swept propellers. Section 2.1 first discusses the aerodynamics of propellers. This is followed by an explanation of the mechanics of propeller acoustics in Section 2.2. Finally, the structural behaviour is described in Section 2.3.

2.1. Propeller Aerodynamics

A propeller is a set of blades which are shaped like wings. By spinning the propeller, the air is accelerated backwards, producing thrust. This is shown in Figure 2.1, which shows the propeller streamtube. Air is sucked into the propeller, or actuator disk, and accelerated axially. This is accompanied by a pressure jump across the disk. As the streamtube contracts behind the disk, the flow accelerates further, until the induced velocity downstream is twice the velocity induced at the rotor disk. This is a simple explanation of how a propeller produces thrust.

A detailed breakdown of the velocities on a propeller blade explains how these forces are generated. Figure 2.2 shows the breakdown of the velocities on an airfoil cross-section of the propeller blade. The airfoil section is set at an angle β. The blade experiences an axial velocity V_∞ due to the forward speed of the aircraft and a tangential velocity $n \times r$ due to the rotation of the propeller. Induced velocities are generated by the forces acting on the blade. The flow is axially accelerated by w_a due to thrust. The tangential velocity is reduced by w_t due to the torque. Adding these induced velocities to the freestream and rotational velocity results in the resultant velocity vector V. The angle between the resultant velocity vector and the plane of rotation is the inflow angle φ. V forms an angle of attack with the chord line of the airfoil. Thus, lift and drag forces are generated. These forces are decomposed into the local thrust and torque components:

$$T' = L' \cos\varphi - D' \sin\varphi \qquad (2.1) \qquad\qquad Q' = D' \cos\varphi + L' \sin\varphi \qquad (2.2)$$

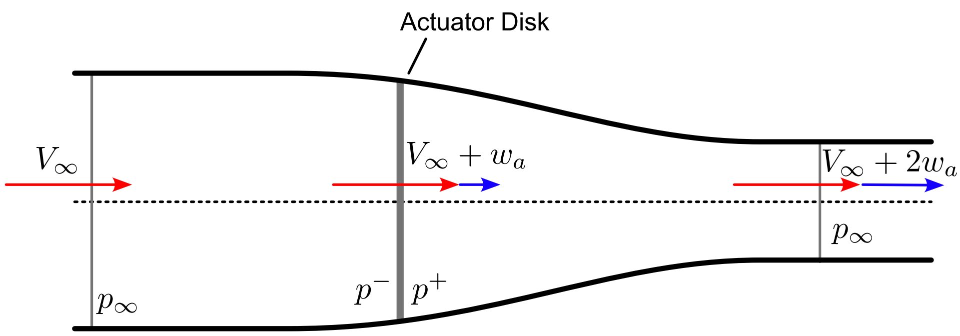

Figure 2.1: Drawing of the propeller streamtube.

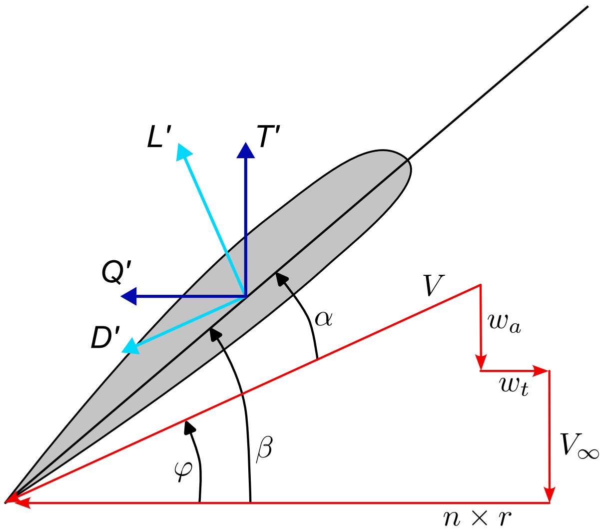

Figure 2.2: Breakdown of velocities and forces acting on propeller airfoil section.

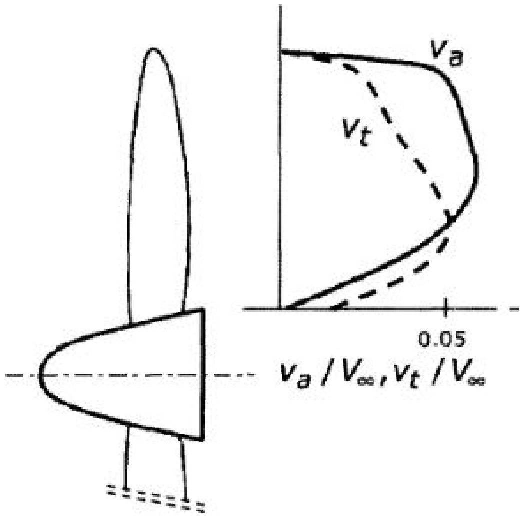

Figure 2.3: Typical induced velocity distribution of a lightly loaded propeller blade. (from Veldhuis [14])

The propeller spins around an axis, thus the rotational velocity component is a function of the distance from this axis of rotation. The pitch angle β is also varied radially. Consequently, the axial and tangential induced velocity distribution is approximately shaped as shown in Figure 2.3 [14]. As a result, the thrust and torque will also vary radially. In fact, due to tip effects and this distribution of induced velocities, the maximum loading of a propeller blade is located more outboard compared to a traditional wing.

One characteristic of low-noise propeller design is that the blades are often swept. Numerical and experimental research has shown that this may result in complex flow phenomena. CFD simulations by Sinnige et al. [15] in Figure 2.4 show leading-edge vortices forming due to the high sweep, a sharp edge and high local angle of attack. Oil-film interferometry measurements were performed by Schülein et al. [16] to map the flow topology of a swept propeller blade, shown in Figure 2.5. Many viscous flow phenomena were identified. Significant parts of the flow become turbulent as the loading increases. The laminar flow separates from the surface near the root due to trailing-edge separation bubbles. Towards the tip, the laminar flow is separated by leading-edge bubbles and vortices.

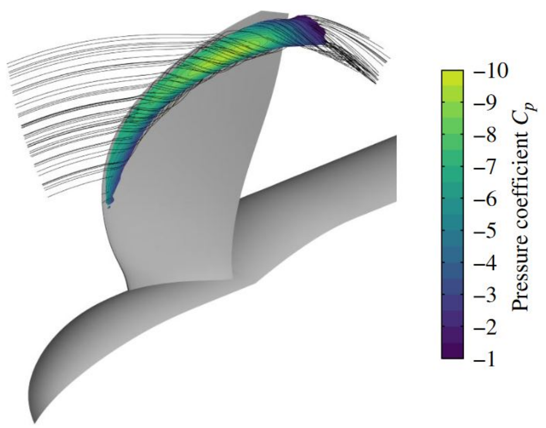

Figure 2.4: Leading edge vortex forming on a highly swept propeller blade. (from Sinnige et al. [15])

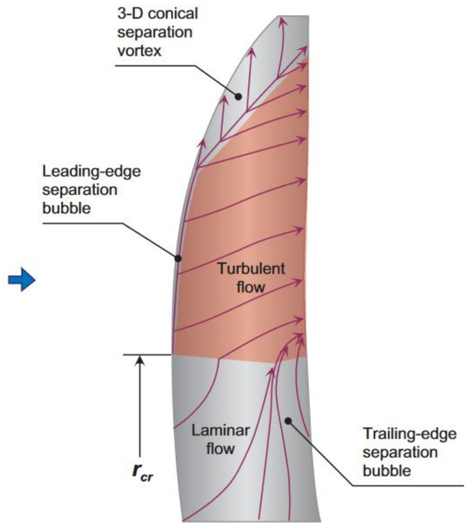

Figure 2.5: Flow topology over a swept blade for low advance ratio (From Schülein et al. [16])

Scaling parameters are required to compare the aerodynamic performance of different size propellers and operating conditions. The performance indicators used in this research are given below. The thrust coefficient C_T and the torque coefficient C_Q are indicative of the local blade loading. The efficiency of the propeller says how much of the shaft power is converted into useful thrust.

$$C_T = \frac{T}{\rho n^2 D^4} \tag{2.3}$$

$$C_Q = \frac{Q}{\rho n^2 D^5} \tag{2.4}$$

$$C_P = \frac{P}{\rho n^3 D^5} \tag{2.5}$$

$$\eta = \frac{T U_\infty}{P} = \frac{C_T}{C_P} J \tag{2.6}$$

Besides these performance indicators, it is important to define the operating conditions of the propeller. For most modern propellers, both the rotational speed and the pitch setting can be set. These operational settings both alter the local angles of attack of the blade and, thus, affect the forces generated. The rotational speed n is nondimensionalised using the propeller diameter and the freestream velocity. This results in the advance ratio J, shown in Equation (2.7). The advance ratio is the ratio between the freestream velocity and the blade tip speed. It can also be seen as the forward distance travelled in a single revolution, divided by the propeller diameter. In addition to the advance ratio, the blade pitch angle can be set. This angle is often taken at 70% of the blade radius, $\beta_{0.7R}$. The advance ratio J and pitch setting $\beta_{0.7R}$, together with the Reynolds number and the Mach number, describe all the operational conditions.

$$J = \frac{U_\infty}{nD} \tag{2.7}$$

2.2. PROPELLER ACOUSTICS

2.2.1. NOISE SOURCES

A propeller generates noise due to it displacing air as it spins and the resulting pressure fluctuations on the blades. The propeller forms one of the biggest sources of noise on an aircraft due to a lack of a casing and the high tip speeds [17]. Propeller noise can be categorised into two types, each of which will be explained further:

- Tonal noise
- Broadband noise

Tonal noises are periodic, meaning they repeat at a constant rate [4]. In the case of a propeller, these periodic pressure fluctuations are due to the blades spinning at a constant RPM. Thus, these noises occur as peaks at integer multiples of the blade-passage frequency. The blade-passage frequency is the rotational speed of the propeller n, multiplied by the number of blades B [4]. These tonal noise characteristics are also shown in Figure 2.6. The tonal noise sources can be further divided into different sources.

Thickness noise occurs due to the displacement of air by the physical blades. As such, it is proportional to the volume of the blade and is influenced by the blade shape and the rotational speed. This noise source becomes dominant at high speeds but can be reduced by using thin, swept blade sections [4].
The loading noise is the result of the pressure field that forms around the blades. Although this pressure field forms the thrust and torque of the propeller, it also propagates as noise. This noise source is prevalent at low to moderate speeds and can be reduced by reducing the loading on the blade. This can be achieved by increasing the diameter or number of blades [17].
Unsteady-loading noise may occur when there is a source of inflow distortion, such as when the propeller shaft experiences an angle of attack. This will result in a circumferential variation of blade loading during a revolution of the blade. This source of noise may interact with the loading noise, in the form of destructive or constructive interference [4].
The final tonal noise source is the quadrupole noise. While the thickness and loading sources are linear at moderate blade speeds, nonlinear effects grow at transonic speeds. The quadrupole noise includes the transonic effects on the thickness and loading noise [17].

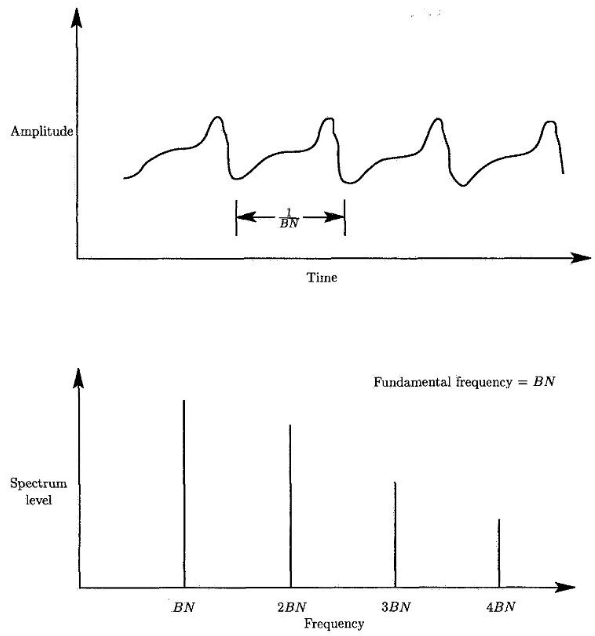

Figure 2.6: Tonal noise characteristics of a propeller. (from Hubbard [4])

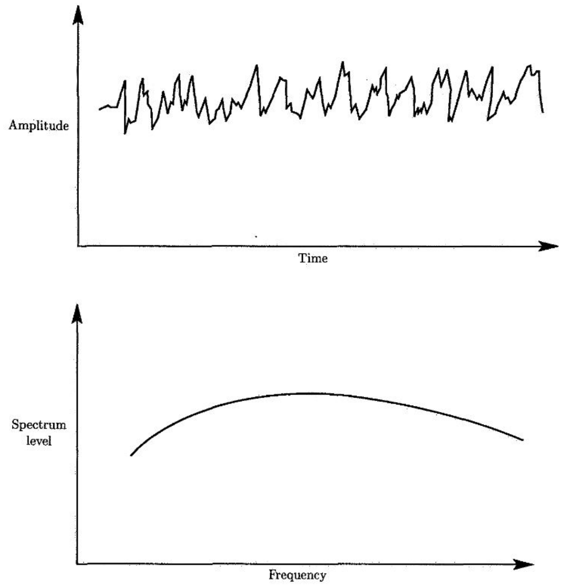

Figure 2.7: Broadband noise characteristics of a propeller. (from Hubbard [4])

Broadband noise is a random source of noise. It contains pressure fluctuations across the entire frequency spectrum, as shown in Figure 2.7. The broadband noise sources are all due to flow turbulence acting on the blades [4]. Turbulence-ingestion noise is the interaction between inflow turbulence and the leading edge of the blades. It is only relevant under high-inflow turbulence [17]. Trailing-edge noise is due to the turbulent boundary layer near the trailing edge of the blade. This turbulent boundary layer results in a fluctuating blade loading that propagates as noise [4]. For full-scale propellers, tonal noise sources are dominant. As such, broadband noise is often omitted, as it does not significantly contribute to the total noise emissions of a propeller [4].

2.2.2. Noise Scaling Parameters

The noise level is most commonly defined using Sound Pressure Level (SPL), which describes the amplitude of the acoustic waves by taking the root-mean-square of the pressure waves. The equation is shown in Equation (2.8). The SPL is made dimensionless with a reference pressure value. The most common reference pressure used is the threshold of human hearing, which is $p_{ref} = 20\mu Pa$. The convenience of using the threshold of human hearing is that it can easily be related to the loudness of noises that everyone is familiar with. The SPL is a function of the frequency and the axial directivity angle θ. The dependence of frequency is removed with the Overall Sound Pressure Level (OSPL) in Equation (2.9), which rates all frequencies equally.

$$SPL = 20 log\left(\frac{p_{rms}}{p_{ref}}\right) \tag{2.8}$$

$$OSPL(\theta) = 10\log\sum_{i}^{n} 10^{SPL(f_i,\theta)/10} \tag{2.9}$$

OSPL is scaled using properties of the human hearing. This property is in no way related to the physical propeller and its operating conditions. As such, it cannot be used as a valid scaling parameter. Instead, Geng et al. [8] propose the use of a thrust-scaled acoustic performance indicator, namely the Thrust-Specific Sound Pressure (TSSP). This acoustic indicator is scaled with the propeller diameter and generated thrust, shown in Equation (2.10). As such, it can be used to compare different propeller sizes and operating conditions. The lack of Mach number still poses a problem though, as the Mach number greatly affects the noise levels. Thus, if one were to compare different experiments, the Mach number needs to match to allow for a fair comparison.

$$TSSP = 20 log\left(\frac{p_{rms}D^2}{T}\right) \tag{2.10}$$

2.2.3. LOW-NOISE PROPELLER CHARACTERISTICS

The noise emissions can be reduced by altering the propeller shape and operating conditions. This is mainly done by reducing the blade loading and the local Mach number [4]. In fact, reducing the propeller rotational speed is one of the most effective methods for reducing noise emissions. This is because the radiation efficiency of all noise sources is a function of the relative velocity.

The thickness noise is a function of the total blade volume. As such, by decreasing the blade volume a significant contribution of noise in high-speed cruise may be reduced. The blade volume is reduced by lowering the airfoil thickness, the chord and the overall diameter [4].

The loading noise, which is most prominent at low speeds, is a function of the radial blade loading. Decreasing the overall blade loading and moving the blade loading more inboard are both effective methods of reducing this noise contribution. In terms of propeller shape, this means changing the twist and chord distribution such as to increase the loading near the root. This may have adverse effects on the aerodynamic efficiency though. By adding more blades to the propeller, the overall loading on a single blade can be reduced. But the addition of blades changes the frequency of the noise, and the overall blade volume could increase [4].

Finally, all sources of noises can be reduced by introducing a blade sweep. Blade sweep acts as a phase lag which can induce interference between sound waves. The concept of this destructive interference is shown in Figure 2.8. The benefit of blade sweep is most apparent at high Mach numbers such as during cruise conditions [4].

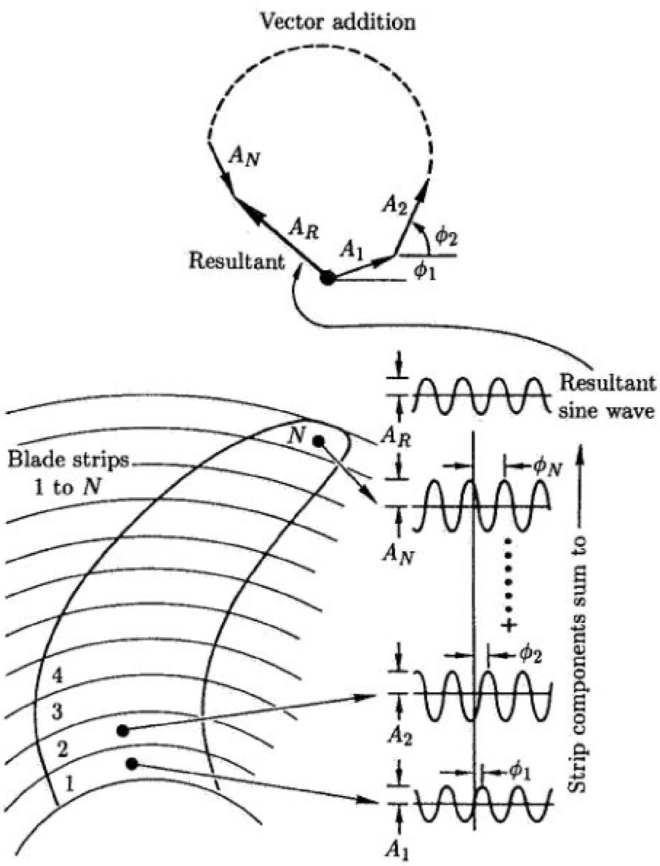

Figure 2.8: Destructive wave interference due to blade sweep. (From Hubbard et al. [4])

Many of these geometrical characteristics can be combined to lower the overall noise emissions of a propeller. As such, these low-noise propeller designs can be distinguished due to having a high number (>6) of slender, swept blades.

2.3. Propeller Structures

2.3.1. Propeller Deformation Modes

The propeller experiences significant forces that may cause the blades to deform. The types of loading acting on the propeller are shown in Figure 2.9. These loadings are:

- The thrust load.
- The torque load
- The centrifugal load.

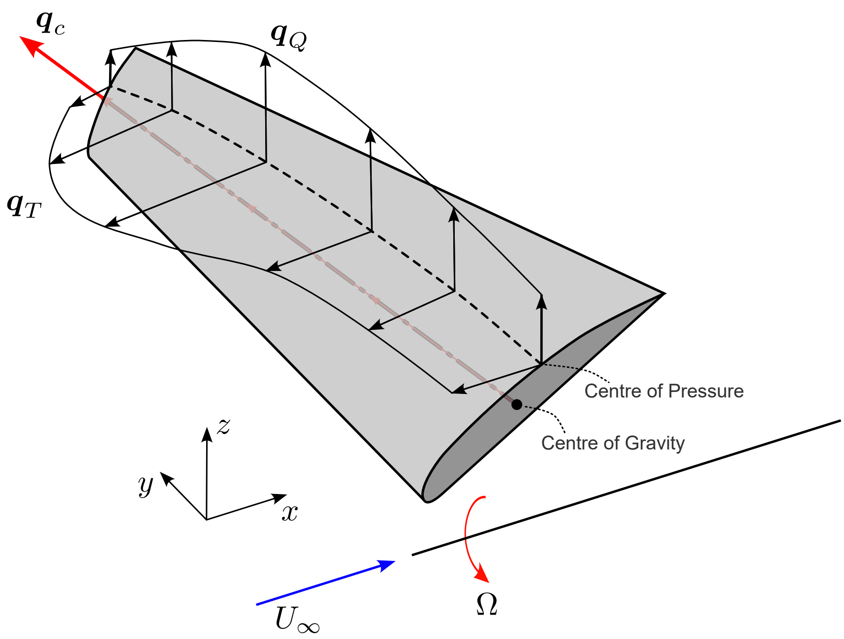

Figure 2.9: Definition of the types of loading on a propeller blade.

The two aerodynamic loads act on the centre of pressure, which varies radially. The thrust load $\boldsymbol{q}_T$ results in a bending moment around the local z-axis. The torque load $\boldsymbol{q}_Q$ results in the bending moment around the local x-axis. Because the centre of pressure does not coincide with the centre of gravity, the aerodynamic load will also generate a twisting moment around the local y-axis. The shear forces acting on the blade from the aerodynamic load are often neglected as they are small compared to the bending and twisting moments [18].
A resultant centrifugal load $\boldsymbol{q}_c$ acts on the local centre of gravity, pointing away from the axis of rotation. This centrifugal load is mainly a tensile force for straight blades, thus it will not generate any (significant) bending moments.

A propeller blade can be modelled as a cantilevered beam, where the root is clamped. The bending and twisting moments will then generate stresses in the blade and deform the shape elastically. Due to the bending moments, the blade can bend in the xz-plane. The tensile forces from the centrifugal load may elongate the blade radius slightly. The twisting moments will cause changes in the blades twist angle. Even small changes in the twist angle can cause large changes in the aerodynamic loading of the propeller as the range of zero lift angle of attack to stall may only be 10° [19].

2.3.2. Low-Noise Propeller Deformations

The bending and torsional deformations of a low-noise propeller blade may be significantly higher than a conventional straight blade, mainly due to sweep. Similarly to a swept aircraft wing, a swept propeller blade will experience a bending-twisting coupling. This can result in wash-in or wash-out, depending on the sweep direction. The aerodynamic loads on a backwards swept wing will cause the blade to wash-out, meaning that the angle of attack decreases.

The two bending modes around the x and z-axis are also heavily coupled, as was observed by Sodja et al. [20, 21]. The twist distribution causes the major and minor principal axes directions to vary significantly throughout the blade radially. This results in bending in one direction (x or z), also causing bending in the other direction. This can be seen in Figure 2.10 (note the different coordinate system definition). This figure shows that a simple tip load applied in one direction induces significant bending in both y and z. In fact, the tip load F_z causes almost equal deformation in the y and z directions.

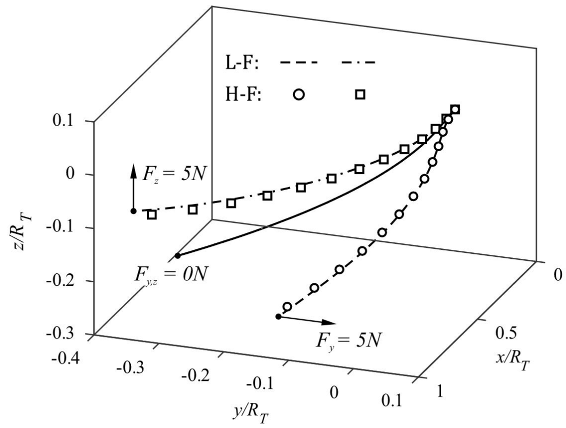

Figure 2.10: Bending coupling of a swept propeller with an applied tip load. (From Sodja et al. [21])

The centrifugal load $\boldsymbol{q}_c$ always points towards the axis of rotation. While this results in a mainly centrifugal force for straight blades, any sweep or dihedral will also cause the centrifugal load to generate significant bending and twisting moments. The centrifugal load tries to straighten the blade back towards the rotational plane, as seen in the drawing by Sodja et al. in Figure 2.11 [21]. This figure shows a blade with dihedral, or coning. No matter whether the blade has positive or negative coning, the centrifugal forces will try to straighten the blade back towards the rotational plane. The same is true for any sweep, the centrifugal loads will pull the blade straight so the sweep reduces. Due to the varying sectional centre of gravity position, a twisting moment may also be induced.

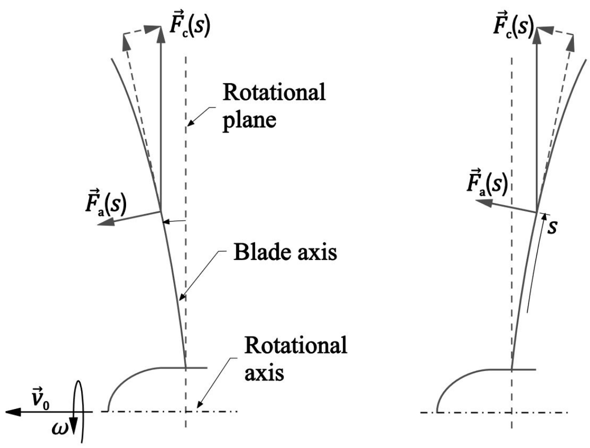

Figure 2.11: Straightening of the propeller blade due to the centrifugal loads. (From Sodja et al. [21])

II

METHODOLOGY

3 Propeller Framework

In this chapter, the propeller framework that is used for this research is shown. The capabilities and features of the framework are first shown in Section 3.1. The parametrisation of the propeller blade is discussed in Section 3.2, and the propeller construction is demonstrated in Section 3.3.

3.1. Framework Features

To couple the three tools of aerodynamics, structures and acoustics, a base framework is required which can construct the propeller geometry and calculate any properties needed by any of the attached tools. Such a framework has already been developed in Matlab by G. Margalida at the Delft University of Technology [1].Figure 3.1 contains an overview of the workflow of the Smart Rotors framework. A non-dimensional blade is first constructed based on a set of inputs. This blade is then converted into a full-scale propeller configuration. Aerodynamic, structural and acoustic performance can be analysed using any exchangeable tool. For the aerodynamic solver, a BEM tool and multiple Lifting-Line Theory (LLT) implementations are available. Polar databases can be used to improve the accuracy of these aerodynamic tools. For acoustic analyses, a version of Hanson's Helicoidal Surface Theory is available, developed by J. Goyal[22]. Structural deformations of straight blades can be calculated using a simple Euler-Bernoulli (EB) beam theory tool. With this workflow, it is possible to perform stand-alone analyses, batch analyses and blade shape optimisations.

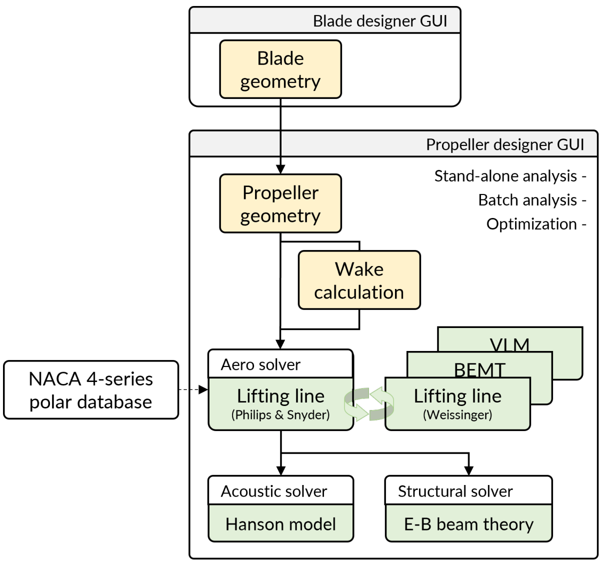

Figure 3.1: Workflow and features of the Smart Rotors framework[1]

[1]Smart Rotors Project: Gabriel Margalida (Accessed in June 2023) [Unpublished]

For this thesis, a new aerodynamic tool is developed for this framework in the form of a Vortex Lattice Method (VLM) code. The acoustic tool is modified such that it can process the results of the VLM tool. The structural tool is rebuilt such that it can process swept propeller blades.

3.2. BLADE PARAMETRISATION

Propellers are constructed from dimensionless blade structures. These dimensionless blade structures are entirely parametrised using 7 radial distributions. The airfoil is discretised into N_c elements, with a cosine spacing. The shape is based on the NACA 4-series, shown in Figure 3.2a. The three distributions to describe a NACA 4-series airfoil are:

- t/c, thickness to chord ratio.
- m, maximum camber.
- p, maximum camber position.

The airfoils constructed from these three radial distributions are stacked on top of each other according to the remaining four radial distributions, as can be seen in Figure 3.2b. Cosine spacing is used at the root and tip to stack N_s number of airfoils on top of each other. Thus, the external surface of the blade is described by a total of $N_s \times (2Nc)$ 3D-coordinates. The four distributions to define the airfoil stacking are:

- c/R, chord to radius ratio.
- β, twist angle.
- $x_{c/4}$, x-alignment of the quarter chord (sweep).
- $y_{c/4}$, y-alignment of the quarter chord (dihedral).

These distributions can either be input as a custom set of N_s data points, or using cubic bézier curves. Cubic bézier curves produce smooth lines with six parameters.

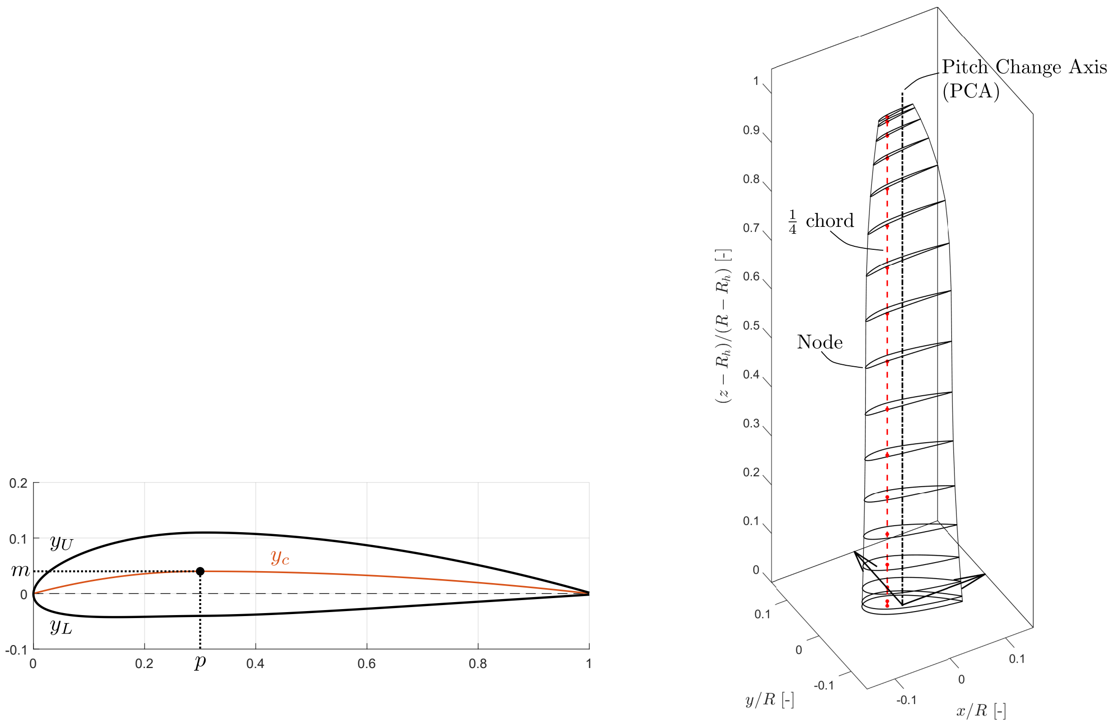

(a) Definition of the airfoil parameters, based on the NACA 4-series

(b) Stacking of the airfoil nodes to obtain the blade geometry

Figure 3.2: Parametrisation of the airfoil and blade as defined by the Smart Rotors framework

3.3. Propeller Definition

The nondimensional blades are dimensionalised using the propeller radius R and the hub radius R_h. The first blade out of an N_b-bladed propeller system is positioned in the global coordinate system such that its Pitch Change Axis (PCA) lies on the global y-axis, as shown in Figure 3.3. In this coordinate system, the propeller rotates around the negative x-axis. Thus the effective flow rotates positively around the x-axis. The inflow velocity is defined as positive along the x-axis. The remaining blades are distributed equally over the actuator disk, as shown in Figure 3.4. Each of these blades produce a rotational wake at its trailing edge. The wake modelling is discussed in more detail in Chapter 4.

For uniform flow, it can be assumed that the aerodynamic performance of each blade is identical. This assumption is used to perform the structural and acoustic analyses only on the blade placed on the y-axis. The results for this first blade are then converted to the remaining blades since it can be assumed that these blades would respond identically.

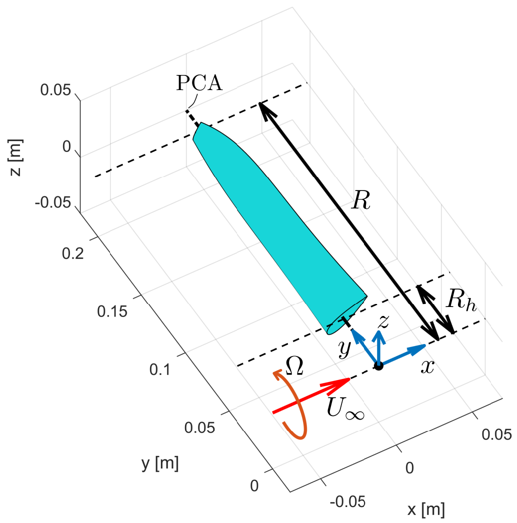

Figure 3.3: Definition of the dimensionalised propeller blade assembled in the global coordinate system.

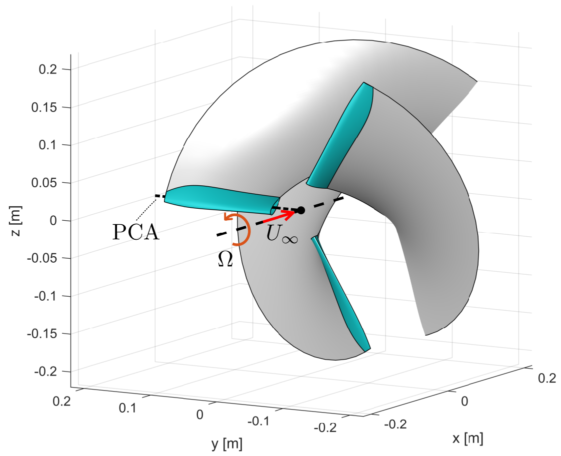

Figure 3.4: Multiple propeller blades with their wakes assembled into the global propeller system.

4

Aerodynamic Tool

In this chapter, a detailed explanation of the aerodynamic model is provided. For the aerodynamic analysis of a propeller geometry, the Vortex Lattice Method is used. The general methodology is first explained in Section 4.1. The modifications required to make the method applicable to propellers are shown in Section 4.2. The assumptions and limitations of the tool are summarised in Section 4.3.

4.1. General Vortex Lattice Methodology

The Vortex Lattice Method is a potential flow method which uses flow singularities with varying strengths to model the inviscid potential flow. Straight vortex segments, such as the one in Figure 4.1, are positioned on the lifting surface. The velocity induced at any point P by such a straight vortex segment with strength Γ can be calculated using the Biot-Savart law:

$$\boldsymbol{q} = \frac{\Gamma}{4\pi} \frac{\boldsymbol{r}_1 \times \boldsymbol{r}_2}{|\,\boldsymbol{r}_1 \times \boldsymbol{r}_2\,|^2} \boldsymbol{r}_0 \cdot \left(\frac{\boldsymbol{r}_1}{r_2} - \frac{\boldsymbol{r}_2}{r_1}\right) \tag{4.1}$$

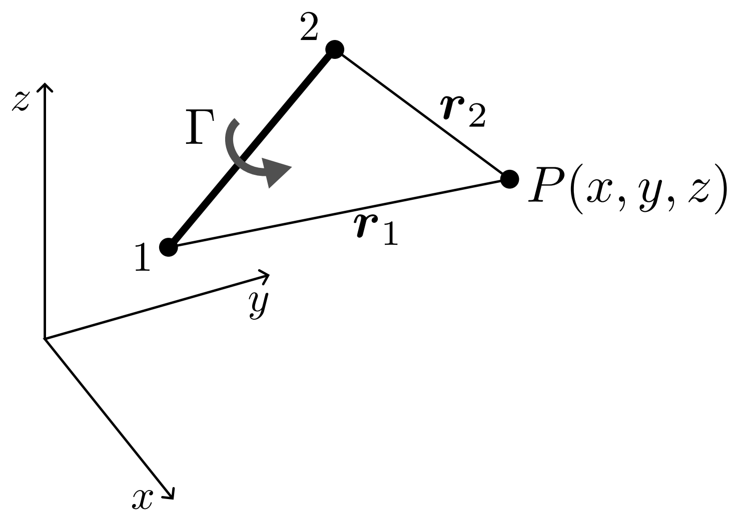

Figure 4.1: Flow on point P induced by a straight line vortex segment with strength Γ.

The lifting surface is split up spanwise and chordwise into quadrilateral panels to model the potential flow over the entire surface. The properties of a quadrilateral panel are shown in Figure 4.2a. The collocation point is located on the 3/4 quarter chord point, where the normal vector $\boldsymbol{n}$ is defined. Singularities are then positioned on the quadrilateral panels to form different types of panel elements. The two most common singularity elements used for the VLM are the horseshoe vortex and the vortex ring element, shown in Figure 4.2b and Figure 4.2c respectively. The horseshoe panel consists of a bound vortex at the 1/4 chord position and two trailing vortices which extend to 'infinity'. Alternatively, the vortex ring element consists of four vortex line segments. Two bound vortices, AB and CD are positioned at the panel's 1/4 chord and 5/4 chord positions. The two trailing vortices BC and DA close the loop. Vortex ring elements have been chosen for this VLM application due to their programming simplicity and benefits in wake modelling.

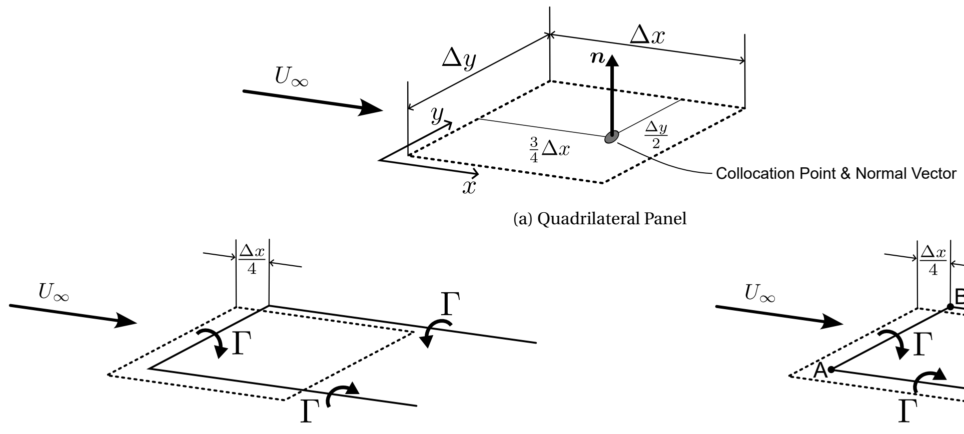

(a) Quadrilateral Panel

(b) Horseshoe Vortex Panel

(c) Ring Vortex Panel

Figure 4.2: Definition of the VLM panel.

The camber surface of the lifting surface is covered in vortex ring elements, as depicted in Figure 4.3. The thickness of the lifting surface is ignored. Each ring element has its unique circulation strength $\Gamma_{i,j}$. These circulation strengths are solved for by applying the boundary condition, which states that the flow shall be tangent to the camber surface. This means there shall be no normal component of the flow at the collocation points, as described in Equation (4.2).

$$\nabla(\Phi_\infty + \phi)\cdot \boldsymbol{n} = 0 \tag{4.2}$$

For the remainder of the figures and equations in this section, the conventions shown in Figure 4.4 are used. A lifting surface is divided into M columns of chordwise panels and N rows of spanwise panels. Thus the entire surface is comprised of $m = M \times N$ ring panels. The panel counter K starts at the leading edge of the wing root and counts from the root to the tip for each column of chordwise panels. Using these conventions, a panel and its properties may either be referred to with its position within the surface, or with the panel sequence counter K, i.e. $\Gamma_{i,j}$ and Γ_K.

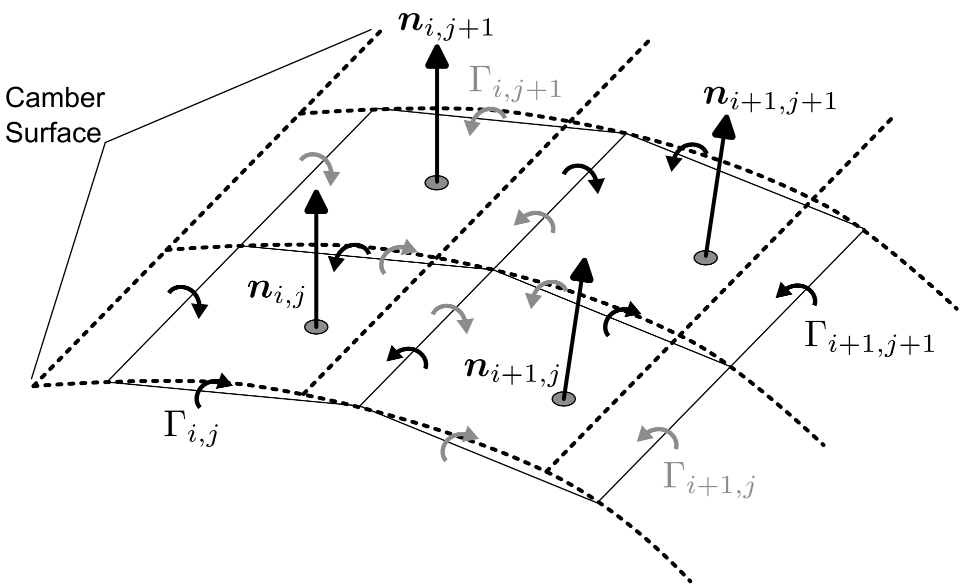

Figure 4.3: Discretisation of a lifting surface by placing multiple vortex ring panels.

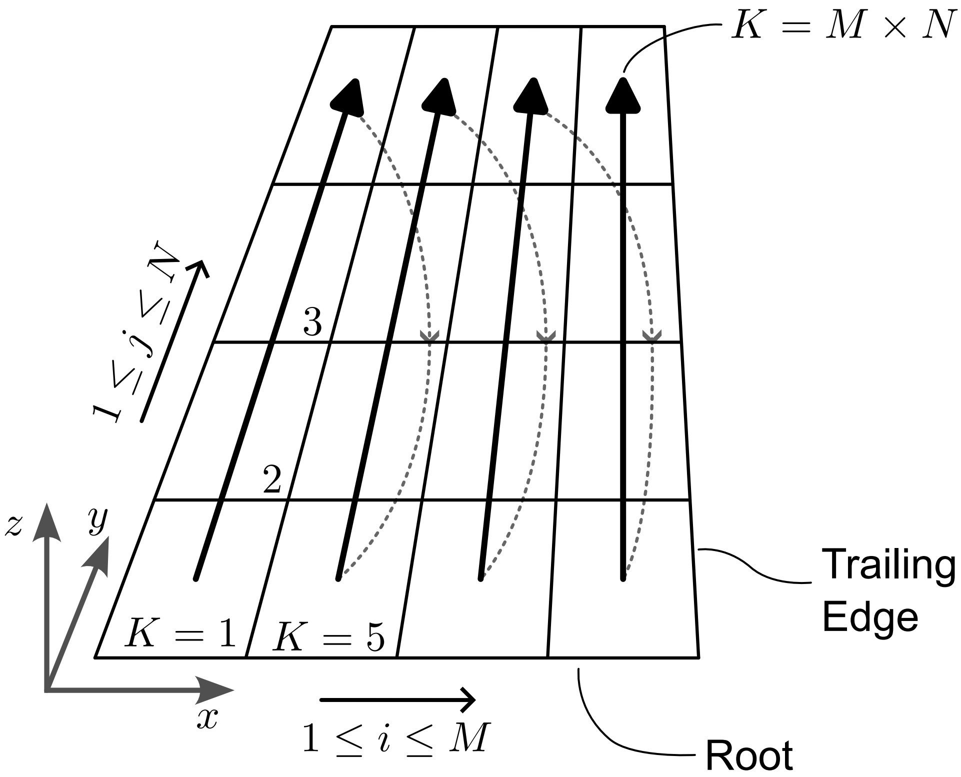

Figure 4.4: Numbering and ordering conventions of the discredited panel surface.

To model the wake and satisfy the Kutta condition such that there is no circulation at the trailing edge, wake panels need to be shed from the trailing edge. Shown in Figure 4.5, ring elements which align with the local streamlines are added to the trailing edge along the entire lifting surface. Since only steady aerodynamics are considered, all the wake panels have the same circulation strength as the trailing edge panel from which they are shed.

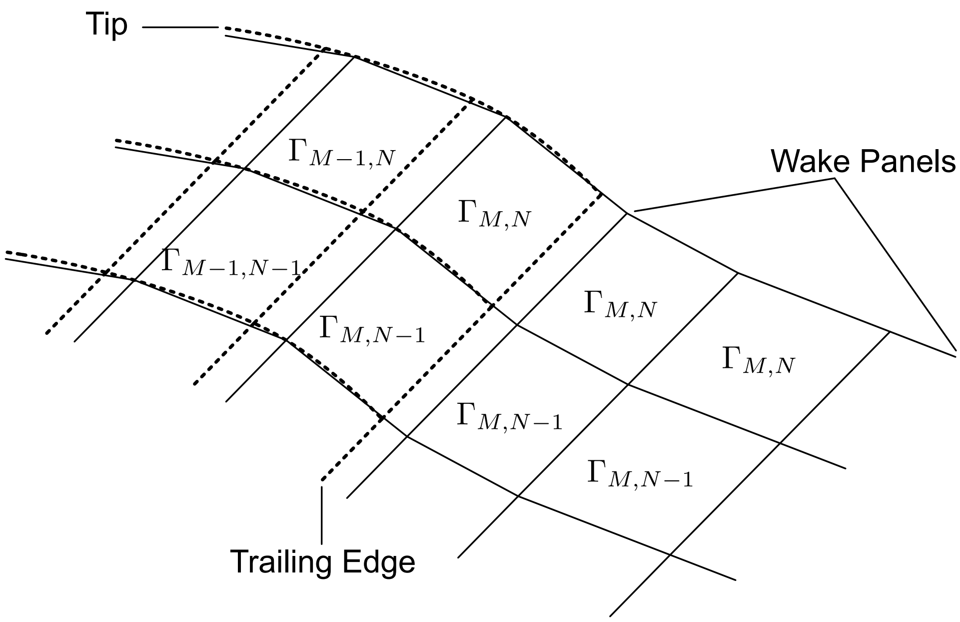

Figure 4.5: Modelling of the wake surface by positioning wake panels at the trailing edge.

With the lifting surface panel array and wake panel array constructed, the system can be solved. The basic principle is that the velocity induced by each ring panel with a unit circulation strength is calculated on each collocation point. As each panel is sequenced through for each collocation point, there are two sequence counters: counter K to indicate the collocation point and counter L to indicate the vortex ring panel. The induced velocity on a collocation point by a ring panel with unit strength is called the influence coefficient, and is defined as in Equation (4.3). Since each ring element consists of four vortex segments, the Biot-Savart law is applied four times.

$$a_{KL} = (u,v,w)_{KL} \cdot \boldsymbol{n}_K = \Big[(u,v,w)_{AB} + (u,v,w)_{BC} + (u,v,w)_{CD} + (u,v,w)_{DA}\Big]_{KL} \cdot \boldsymbol{n}_K \tag{4.3}$$

Since there are m total ring elements, and m total collocation points, there are a total of $m \times m$ influence coefficients that need to be calculated. These are arranged in a matrix such that the vertical rows indicate the different collocation points, and the horizontal columns indicate the vortex rings, as in Equation (4.4). Note that since the wake panels have the same circulation strength as the trailing edge panels, the influence of the wake panels is added onto the influence coefficients of the trailing edge panels $a_{1...m,m-N...m}$. The influence coefficient matrix is multiplied by the circulation strength matrix to obtain the total induced velocity by the panels at each collocation point. The boundary condition stated that the induced velocity plus the freestream velocity shall be tangent to the surface at the collocation point. Thus, the right-hand side of the system in Equation (4.4) is constructed, which is the normal component of the freestream flow at each collocation point.
To solve the system of Equation (4.4) for the panel strengths Γ, the influence coefficient matrix is inversed and multiplied with the right-hand side of the equation.

$$\begin{bmatrix} a_{11} & a_{12} & \cdots & a_{1m} \\ a_{21} & a_{22} & \cdots & a_{2m} \\ a_{31} & a_{32} & \cdots & a_{3m} \\ \vdots & \vdots & \ddots & \vdots \\ a_{m1} & a_{m2} & a_{m3} & a_{mm} \end{bmatrix} \begin{bmatrix} \Gamma_1 \\ \Gamma_2 \\ \Gamma_3 \\ \vdots \\ \Gamma_m \end{bmatrix} = \begin{bmatrix} -\boldsymbol{U}_\infty \cdot \boldsymbol{n}_1 \\ -\boldsymbol{U}_\infty \cdot \boldsymbol{n}_2 \\ -\boldsymbol{U}_\infty \cdot \boldsymbol{n}_3 \\ \vdots \\ -\boldsymbol{U}_\infty \cdot \boldsymbol{n}_m \end{bmatrix} \tag{4.4}$$

$$\begin{bmatrix} \Gamma_1 \\ \Gamma_2 \\ \Gamma_3 \\ \vdots \\ \Gamma_m \end{bmatrix} = \begin{bmatrix} a_{11} & a_{12} & \cdots & a_{1m} \\ a_{21} & a_{22} & \cdots & a_{2m} \\ a_{31} & a_{32} & \cdots & a_{3m} \\ \vdots & \vdots & \ddots & \vdots \\ a_{m1} & a_{m2} & a_{m3} & a_{mm} \end{bmatrix}^{-1} \begin{bmatrix} -\boldsymbol{U}_\infty \cdot \boldsymbol{n}_1 \\ -\boldsymbol{U}_\infty \cdot \boldsymbol{n}_2 \\ -\boldsymbol{U}_\infty \cdot \boldsymbol{n}_3 \\ \vdots \\ -\boldsymbol{U}_\infty \cdot \boldsymbol{n}_m \end{bmatrix} \tag{4.5}$$

With the circulation strength of each vortex ring known, the generated forces can be found. The lift generated at the centre of each bound vortex is calculated using the Kutta-Joukowski theorem:

$$\begin{aligned} \Delta \boldsymbol{L}_{i,j} &= \rho \boldsymbol{U}_\infty \times \Delta \boldsymbol{l}_{i,j} (\Gamma_{i,j} - \Gamma_{i-1,j}) \text{ for } i > 1 \\ \Delta \boldsymbol{L}_{i,j} &= \rho \boldsymbol{U}_\infty \times \Delta \boldsymbol{l}_{i,j} \Gamma_{i,j} \text{ for } i = 1 \end{aligned} \tag{4.6}$$

The induced drag is found by calculating the induced downwash at each collocation point [23]. This downwash is the velocity induced by all trailing vortices. The procedure of finding this is similar to the system of Equation (4.4), the influence of all the bounding vortices have been removed however. This results in the new system of Equation (4.7), which can be easily solved for w_{ind} as the circulation strengths Γ are all known. With the induced downwash at each collocation point known, the induced drag can be calculated using Equation (4.8).

$$\begin{bmatrix} w_{ind1} \\ w_{ind2} \\ w_{ind3} \\ \vdots \\ w_{indm} \end{bmatrix} = \begin{bmatrix} b_{11} & b_{12} & \cdots & b_{1m} \\ b_{21} & b_{22} & \cdots & b_{2m} \\ b_{31} & b_{32} & \cdots & b_{3m} \\ \vdots & \vdots & \ddots & \vdots \\ b_{m1} & b_{m2} & b_{m3} & b_{mm} \end{bmatrix} \begin{bmatrix} \Gamma_1 \\ \Gamma_2 \\ \Gamma_3 \\ \vdots \\ \Gamma_m \end{bmatrix} \tag{4.7}$$

$$\begin{aligned} \Delta \boldsymbol{D}_{i,j} &= -\rho \boldsymbol{w}_{ind_{i,j}} \times \Delta \boldsymbol{l}_{i,j} (\Gamma_{i,j} - \Gamma_{i-1,j}) \text{ for } i > 1 \\ \Delta \boldsymbol{D}_{i,j} &= -\rho \boldsymbol{w}_{ind_{i,j}} \times \Delta \boldsymbol{l}_{i,j} \Gamma_{i,j} \text{ for } i = 1 \end{aligned} \tag{4.8}$$

4.2. PROPELLER VORTEX LATTICE METHODOLOGY

The previous section described a general Vortex Lattice Method for a lifting surface. Several modifications are required to make this method applicable to propellers.

4.2.1. ROTATIONAL EFFECTS

A rotational component of the velocity is induced over the blade as the propeller spins. A new boundary condition is required which states that the sum of the freestream velocity, the rotational velocity and the induced velocity needs to be tangent to the body surface:

$$\nabla(\Phi_\infty + \Phi_\Omega + \phi) \cdot \boldsymbol{n} = 0 \tag{4.9}$$

The equations of the previous section need to be updated to include this new total velocity. First of all, the rotational velocity is included in the right-hand side of Equation (4.4). The rotational velocity at each panel is a function of the vectorised rotational speed $\boldsymbol{\Omega}$ and the vector $\boldsymbol{r}$ from the rotational axis to the collocation point.

$$RHS_K = -(\boldsymbol{U}_\infty + \boldsymbol{\Omega} \times \boldsymbol{r}_K) \cdot \boldsymbol{n}_K \tag{4.10}$$

The rotational velocity $\boldsymbol{U}_\Omega$ is also included in the lift equation of each panel:

$$\begin{aligned} \Delta \boldsymbol{L}_{i,j} &= \rho(\boldsymbol{U}_\infty + \boldsymbol{U}_\Omega) \times \boldsymbol{\Delta y}_{i,j}(\Gamma_{i,j} - \Gamma_{i-1,j}) \text{ for } i > 1 \\ \Delta \boldsymbol{L}_{i,j} &= \rho(\boldsymbol{U}_\infty + \boldsymbol{U}_\Omega) \times \boldsymbol{\Delta y}_{i,j}\Gamma_{i,j} \text{ for } i = 1 \end{aligned} \tag{4.11}$$

4.2.2. WAKE MODELLING

The wake panels of the generalised VLM have to be adapted to represent the accelerating and contracting wake of a propeller. Within the Smart Rotors framework, it is possible to model a frozen, semi-free, or free wake. The frozen wake only models the acceleration of the wake using a set of user-chosen inputs. The semi-free wake is an iterative scheme where the acceleration and contraction of the wake are solved for iteratively, requiring multiple VLM simulations. The free wake uses a time step to calculate a new wake panel that sheds from the trailing edge. Multiple VLM simulations are then performed to create a sufficiently long enough wake surface. The frozen wake is used for this research as its results are adequate, and no iterations are required, significantly reducing the computational time.

The frozen wake is constructed using the two parameters A_{conv} and A_{expan}. A_{conv} sets the axial velocity of the wake at the trailing edge as a fraction of the freestream velocity, scaling from 0 to 1. A_{expan} sets the pitch between the wake surface rotations. The final axial velocity of the wake is then calculated with Equation (4.12). Overall the effects of these wake parameters are not significant. As such, A_{conv} is fixed to the middle point of its range at 0.5. A_{expan} is fixed to 10, but with the number of wake panels used, its effect is negligible on the wake panel positioning.

$$u_{wake} = \boldsymbol{U}_\infty(1 + e^{-A_{expan}*dt} A_{conv}) \tag{4.12}$$

4.2.3. PROPELLER INTERACTIONS

Finally, one needs to account for multiple blades and the interaction effects between them. This is done by modelling all the blades and their wakes as ring panel lattices. Then, assuming steady aerodynamics and uniform flow, the circulation strength distribution of each blade will be identical. This means that one needs to solve for the circulation strengths of only a single blade. Thus, the size of the matrices in the system of Equation (4.4) does not increase if more blades are added. Figure 4.6 shows two blades and their wakes. The collocation points are only located on blade 1. The influence coefficient of vortex panel L on collocation point K now consists of the sum of the induced velocity of panel L on blade 1 and the induced velocity of panel L on blade 2. For B blades present, the influence coefficient is calculated as in Equation (4.13).

$$a_{KL} = \Big[(u,v,w)_{KL,1} + (u,v,w)_{KL,2} + ... + (u,v,w)_{KL,B}\Big] \cdot \boldsymbol{n}_{K,1} \tag{4.13}$$

This means that while the size of the system in Equation (4.4) does not increase, the computational time does increase. This is due to the extra Biot-Savart calculations that are required to calculate the influence coefficients of each panel.

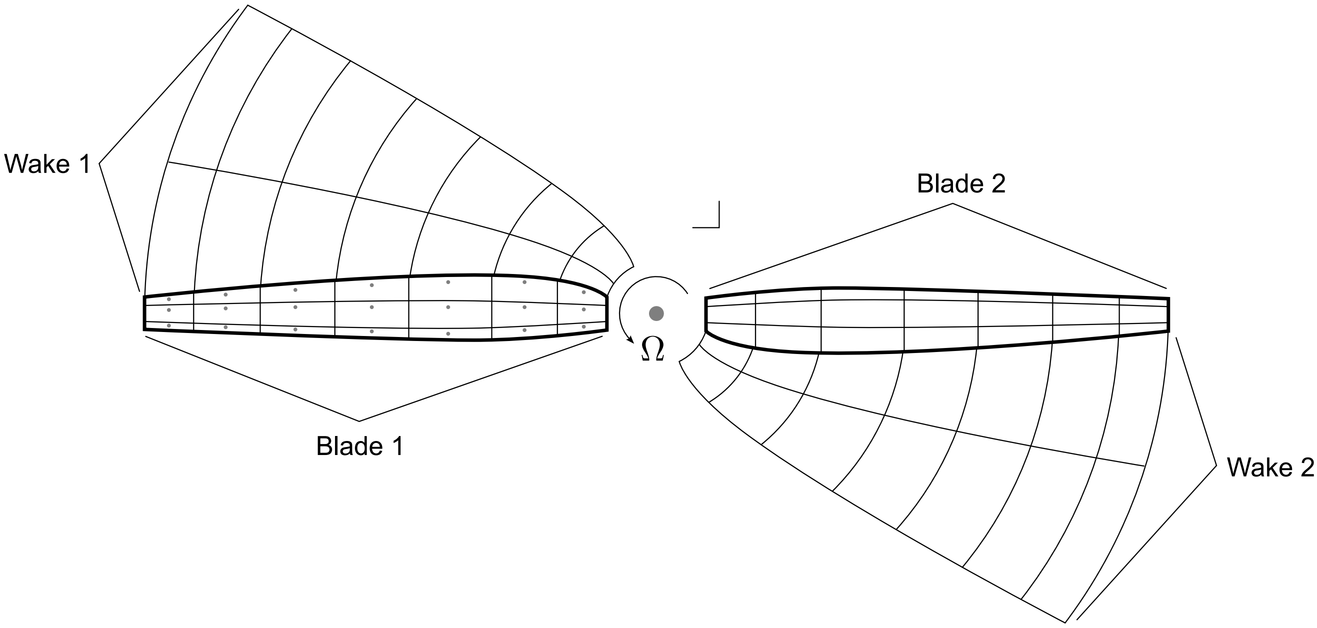

Figure 4.6: Discretisation of a propeller with multiple blades.

4.3. VLM ASSUMPTIONS & LIMITATIONS

The assumptions and limitations of the implemented VLM tool are summarised below.

- No viscous correction is present. With no viscous flow correction, this tool remains purely potential flow. Complex flow phenomena such as flow separation, leading-edge vortices and crossflow are not accounted for. This limits the suitable operation conditions in which the VLM tool may be applied. In particular, high-loading and negative-loading conditions are unsuitable for analysis. The lack of viscosity also affects the results of the VLM tool in the linear flow regime. It is expected for the thrust to be overestimated, due to the lack of decambering effect. The torque will be underestimated, as profile drag will not be present. This combination of errors will result in an overestimation of the propeller efficiency.
- No compressibility correction is present. This limits the operating conditions and dimensions of the propeller. Regarding operating conditions, the inflow velocity U_∞ and the rotational speed should be limited such that the resultant propeller tip speed does not exceed into compressible flow region. Besides limiting the operating conditions, the size of the propeller is also constrained, as a large propeller with a high rotational speed will quickly induce compressible flow at the tips.
- The flow is assumed to be uniform. The incoming flow is constant across the entire propeller face. This means that all the blades of a propeller experience the same incoming flow, and will thus generate identical forces. Non-zero angle of attack situations can not be simulated.
- The flow is assumed to be steady. This means that the flow is constant over time. The wake is stabilised, and new wake panels do not need to be shed off the trailing edge.
- The propeller is assumed to be isolated. Any interactions between the propeller, pylon and wing are neglected. In reality, these structures will interact with each other altering the propeller performance.
- The blade thickness is neglected. The Vortex Lattice Method models the entire lifting wing using only the camber surface. Thick blades may not be accurately modelled.

5

Acoustic Tool

The noise emissions of the swept propellers are calculated using the acoustic tool. This is done using Hanson's far-field Helicoidal Surface Theory, as it models the phase lag effects of non-straight blades. A Matlab code of this model has been developed by J. Goyal [22]. This model has been modified to be compatible with the aerodynamic results generated by the VLM tool. In this chapter, the main principles and equations of the Helicoidal Surface Theory are explained. A more detailed explanation can be found in the paper by D.B. Hanson [24].

5.1. Helicoidal Surface Theory

The Helicoidal Surface Theory (HST) represents the blades as advancing helicoidal surfaces, on which the blade surface is swept out by a radial line, rotating at the angular speed Ω and translating at the freestream velocity U_∞. This helical coordinate system is shown in Figure 5.1 [24]. The sweep of the blade is defined as the Mid-chord Alignment (MCA), which is the distance from the pitch change axis to the midchord. Any dihedral is defined as Face Alignment (FA), which is the perpendicular distance between the pitch change axis and the chord line.

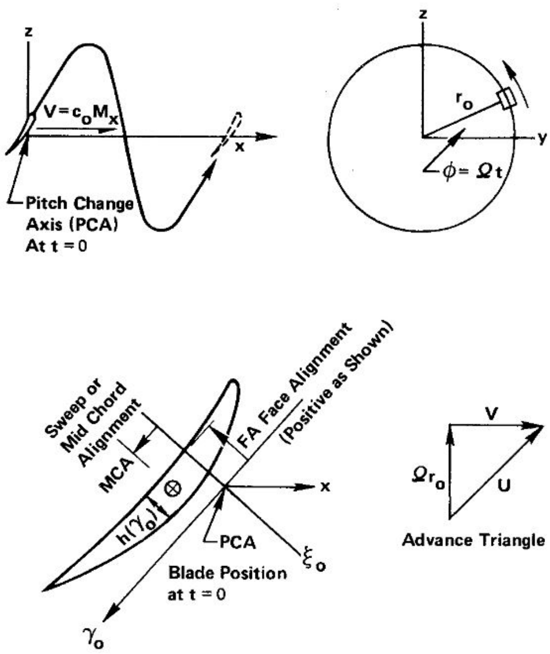

Figure 5.1: Helical coordinate system of the Helicoidal Surface Theory. (From Hanson [24])

The aerodynamic loading and thickness sources are transferred to the advance helix for the radiation calculations. The far-field pressure is then obtained using Green's function in Equation (5.1). P_{mN_b} represents the Fourier transform of the pressure at the mth harmonic of blade-passage frequency for a propeller with N_b blades. The blade-passage frequency is the number of blades N_b multiplied with the rotational speed.

$$p(t) = \sum_{m=-\infty}^{\infty} P_{mN_b} e^{-imN_b\Omega t} \tag{5.1}$$

P_{mN_b} consists of the two noise sources considered in this model, the thickness and loading noise. The loading noise can be further split into either the lift and drag noise, or the thrust and torque noise. In this derivation, only the thrust and torque noise are further considered.

$$P_{mN_b} = P_{Vm} + P_{Lm} + P_{Dm} = P_{Vm} + P_{Tm} + P_{Qm} \tag{5.2}$$

The general equation for the far-field pressure harmonics is given by Equation (5.3) [24]. In this equation, the ambient density ρ and the speed of sound c_0 represent the atmospheric conditions. The observer's position is set using the radiation angle θ and the observer distance y_o. N_b is the number of blades, D is the propeller diameter, B_D is the chord-to-diameter ratio and t_b is the maximum thickness to chord ratio. Three different Mach numbers appear in Equation (5.3); M_x is the flight Mach number, M_r is the section relative Mach number and M_t is the tip rotation Mach number.

$$\begin{aligned}\begin{Bmatrix} P_{Vm} \\ P_{Tm} \\ P_{Qm} \end{Bmatrix} &= -\frac{\rho c_0^2 N_b \sin\theta \exp\left(imN_b\left(\frac{\Omega r}{c_0} - \frac{\pi}{2}\right)\right)}{8\pi (y_o/D)(1 - M_x\cos\theta)} \\ &\times \int_0^1 M_r^2 \exp(i\phi_o + \phi_s) J_{mN_b}\left(\frac{mN_b (r/R) M_t \sin\theta}{1 - M_x\cos\theta}\right) \begin{Bmatrix} k_x^2 t_b \Psi_V(k_x) \\ -i\frac{M_t}{M_r}\left(\frac{mN_b}{1-M_x\cos\theta} - mN_b\right) B_D (C_T/2)\Psi_T(k_x) \\ -i\frac{mN_b}{r/R} B_D (C_Q/2)\Psi_Q(k_x) \end{Bmatrix} d(r/R)\end{aligned} \tag{5.3}$$

The sweep and dihedral of the blade are modelled as phase lag effects, using the MCA and FA, which were defined in Figure 5.1. The equations for the phase lag effects ϕ_o and ϕ_s are shown in Equations (5.4) and (5.5).

$$\phi_o = \frac{2mN_b}{(r/R)M_r}\left(\frac{M_r^2\cos\theta - M_x}{1 - M_x\cos\theta}\right)\frac{FA}{D} \tag{5.4}$$

$$\phi_s = \frac{2mN_b M_T}{M_r(1 - M_x\cos\theta)}\frac{MCA}{D} \tag{5.5}$$

The frequency domain source terms Ψ_V, Ψ_T and Ψ_Q are found by integrating along the chord length for each radial position. For the thickness source term, the thickness distribution of the airfoil is normalised along the nondimensional chord length, like in Figure 5.2. The total thickness source term is then calculated using Equation (5.6). The source term Ψ_V is not very sensitive to the thickness distribution. As such, the thickness distribution is approximated to be parabolic. Figure 5.3 shows the difference in thickness noise when the thickness distribution is approximated as a biconvex parabolic distribution [4].

$$\Psi_V(k_x) = \int_{-1/2}^{1/2} H(x) e^{ik_x x} dx \tag{5.6}$$

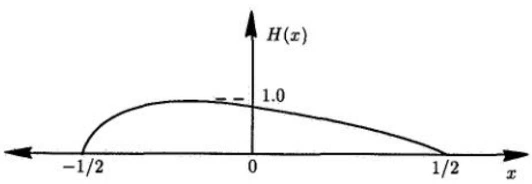

Figure 5.2: Shape function of the chordwise thickness distribution. (From Hubbard [4])

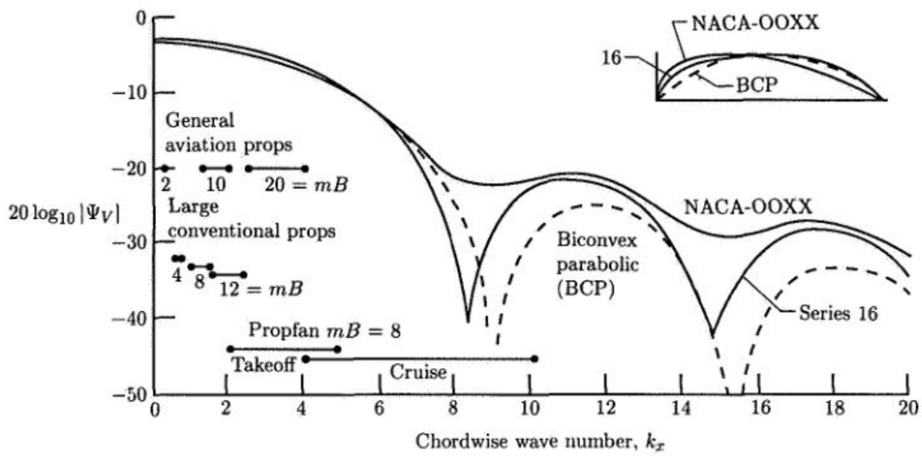

Figure 5.3: Approximation of the thickness noise source by simplifying the thickness distribution. (From Hubbard [4])

The loading source terms Ψ_T and Ψ_Q are found using Equations (5.7) and (5.8). These equations use the chordwise normalised thrust and torque distributions. These distributions can be approximated as parabolic or uniform distributions, as can be seen in Figure 5.4. The loading source terms are much more sensitive to the loading distributions. Specifically, strong peaks can increase the noise significantly. As such, the actual loading distribution obtained from the aerodynamic analysis is used, instead of any of the approximations.

$$\Psi_T(k_x) = \int_{-1/2}^{1/2} f_T(x) e^{ik_x x} dx \tag{5.7}$$

$$\Psi_Q(k_x) = \int_{-1/2}^{1/2} f_Q(x) e^{ik_x x} dx \tag{5.8}$$

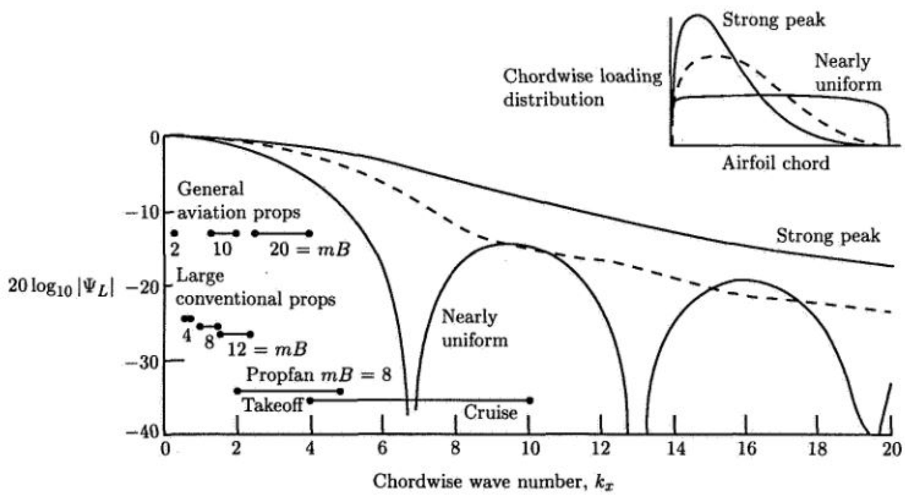

Figure 5.4: Approximation of the chordwise loading noise by simplifying the chordwise loading distribution. (From Hubbard [4])

These source terms are all a function of the chordwise wave number k_x, shown in Equation (5.9). This nondimensional parameter is a measure of the chordwise noncompactness. The final important parameter of Equation (5.3) is the radiation efficiency factor J_{mN_b}. This is a Bessel function of the mN_bth order.

$$k_x = \frac{2mN_b B_D M_t}{M_r(1 - M_x \cos\theta)} \tag{5.9}$$

The pressure fluctuations obtained from the Fourier transforms of the pressure with Green's function (Equation (5.1)) are transformed into the root mean square wave signal by time integration in Equation (5.10). The pressure is cyclic since only steady sources are considered. As such, the time limits only have to cover a single revolution.

$$p_{rms} = \sqrt{\frac{1}{T_2 - T_1} \int_{T_1}^{T_2} p(t)^2 dt} \tag{5.10}$$

Finally, the p_{rms} is converted to the logarthmic decibel scale using either Equation (5.11) or Equation (5.12). The contribution of each noise source can be isolated by calculating the pressure fluctuations $p(t)$ using only a single noise source term Ψ. This way, contributions to the noise due to thrust, torque or thickness can also be expressed in the decibel scale.

$$SPL = 20log\left(\frac{p_{rms}}{p_{ref}}\right) \tag{5.11}$$

$$TSSP = 20log\left(\frac{p_{rms}D^2}{T}\right) \tag{5.12}$$

5.2. HST ASSUMPTIONS & LIMITATIONS

The assumptions and limitations of the HST tool are summarised and some of the potential effects on the results are discussed.

- The propeller blade is assumed to be thin such that all noise sources are positioned on the mean surface. This results in an error of the Face Alignment, and thus a phase lag error. This error is negligible near the plane of rotation at all frequencies [24].
- The thickness distribution of the airfoil is modelled as a parabolic function. The shape of the thickness distribution is negligible, as was shown in Figure 5.3.
- Broadband noise sources are omitted. This has a negligible effect on the results, as tonal noise sources are considerably louder.
- Unsteady noise sources are omitted. Since the aerodynamic model is fully steady, any unsteady noise sources can not be modelled.

6
Structural Tool

The structural tool calculates the stresses and deformations of the blade due to the aerodynamic and inertial loading. The structural model by Sodja et al. [20, 21] is used. This model allows for the analysis of swept propeller blades using the Euler-Bernoulli (EB) beam model in combination with the Saint-Venant theory of torsion.

6.1. Euler-Bernoulli Model

In this structural model, the propeller blades are represented as slender, pre-twisted cantilever beams of variable cross-sections with homogenous and isotropic elastic materials [20]. The structural model defines new local coordinate systems along the blade axis, shown in Figure 6.1. The blade axis is the curve connecting the centre of gravity of each cross-section. s is the arc length of the blade axis spanning from 0 at the propeller hub to l at the blade tip. The local coordinate systems of $\boldsymbol{e}_\xi$, $\boldsymbol{e}^*_\eta$ and $\boldsymbol{e}^*_\zeta$ is defined such that $\boldsymbol{e}_\xi$ is tangent to the blade axis, using Equation (6.1). $\boldsymbol{e}_\eta$ and $\boldsymbol{e}_\zeta$ are aligned with the principal axes of the local cross-section by accounting for the blade twist angle, using Equation (6.2). The twist angles used in the structural model are not identical to the twist angles as defined in the propeller framework, due to the different coordinate systems. β_L refers to the local twist angles along the blade axis.

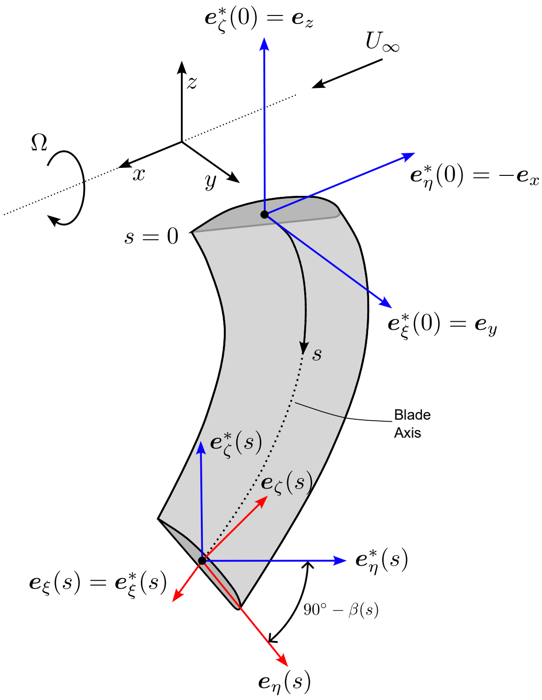

Figure 6.1: Local coordinate system definitions for the structural model.

$$
\begin{aligned}
\boldsymbol{e}_\xi &= x'\boldsymbol{e}_x + \sqrt{1-z'^2-x'^2}\,\boldsymbol{e}_y + z'\boldsymbol{e}_z \\
\boldsymbol{e}^*_\eta &= -\frac{x'z'(1-\sqrt{1-z'^2-x'^2})}{x'^2+z'^2}\boldsymbol{e}_x - z'\boldsymbol{e}_y + \frac{x'^2+z'^2\sqrt{1-z'^2-x'^2}}{x'^2+z'^2}\boldsymbol{e}_z \\
\boldsymbol{e}^*_\zeta &= \frac{x'^2+z'^2\sqrt{1-z'^2-x'^2}}{x'^2+z'^2}\boldsymbol{e}_x - x'\boldsymbol{e}_y - \frac{x'z'(1-\sqrt{1-z'^2-x'^2})}{x'^2+z'^2}\boldsymbol{e}_z
\end{aligned}
\tag{6.1}
$$

$$
\begin{aligned}
\boldsymbol{e}_\eta &= \cos(90-\beta_L)\boldsymbol{e}^*_\eta + \sin(90-\beta_L)\boldsymbol{e}^*_\zeta \\
\boldsymbol{e}_\zeta &= -\sin(90-\beta_L)\boldsymbol{e}^*_\eta + \cos(90-\beta_L)\boldsymbol{e}^*_\zeta
\end{aligned}
\tag{6.2}
$$

The forces acting on the propeller blade consist of the aerodynamic loads $\boldsymbol{q}_a$ and the inertial forces $\boldsymbol{q}_c$. The aerodynamic loads come from the VLM tool from Chapter 4. The chordwise loads at each radial station are summed and averaged to obtain a resultant force and its centre of pressure. The internal moments due to the aerodynamic loads, $\boldsymbol{M}_a(s)$, are then calculated as in Equation (6.3). The integral is taken w.r.t. u, which spans from the local cross-section to the blade tip for each cross-section. The integral is the cross-product of the aerodynamic force and the vector from the blade axis (centre of gravity) to the centre of pressure.

$$
\boldsymbol{M}_a(s) = \int_s^l \left[(\boldsymbol{r}_a(u) - \boldsymbol{r}_q(s)) \times \boldsymbol{q}_a(u)\right] du \tag{6.3}
$$

The blade spinning results in centrifugal forces acting on each blade element. These centrifugal forces are proportional to the section mass, radial position and angular velocity, as shown in Equation (6.4). The vector $\boldsymbol{e}_r$ points from the section's centre of gravity to the axis of rotation of the blade. Equation (6.5) is the formula used to obtain the internal moment due to the inertial loads.

$$
\boldsymbol{q}_c = \rho_b dV\Omega^2 r\boldsymbol{e}_r \tag{6.4}
$$

$$
\boldsymbol{M}_c(s) = \int_s^l \left[(\boldsymbol{r}_q(u) - \boldsymbol{r}_q(s)) \times \boldsymbol{q}_c(u)\right] du \tag{6.5}
$$

$$
\boldsymbol{M}(s) = \boldsymbol{M}_a(s) + \boldsymbol{M}_c(s) \tag{6.6}
$$

The loads and internal moments are all defined in the global coordinate system of the propeller framework. The total internal moment $\boldsymbol{M}$ is decomposed into the three local components via simple dot-product operation:

$$
\begin{aligned}
M_\xi(s) &= \boldsymbol{M}\cdot\boldsymbol{e}_\xi \\
M_\eta(s) &= \boldsymbol{M}\cdot\boldsymbol{e}_\eta \\
M_\zeta(s) &= \boldsymbol{M}\cdot\boldsymbol{e}_\eta
\end{aligned}
\tag{6.7}
$$

The constitutive equations for the bending and twisting of the blade can then be constructed. For the bending deformations of the blade in (global) $\boldsymbol{e}_x$ and $\boldsymbol{e}_z$ directions, the Euler-Bernoulli beam theory principles are applied. The torsion of the blade around the $\boldsymbol{e}_\xi$ vector is obtained using the principles of Saint Venant's theory of torsion, for which warping effects are neglected. It is important to note that there will be a coupling between the bending and twisting of the blade due to any sweep or dihedral in the blade axis. This is accounted for by introducing the curvature of the blade axis in each principal axis direction:

$$
\begin{aligned}
\frac{1}{\rho_\eta}(s) &= \frac{-z''\boldsymbol{e}_x\cdot\boldsymbol{e}_\eta + x''\boldsymbol{e}_z\cdot\boldsymbol{e}_\eta}{\boldsymbol{e}_y\cdot\boldsymbol{e}_\xi} \\
\frac{1}{\rho_\zeta}(s) &= \frac{z''\boldsymbol{e}_x\cdot\boldsymbol{e}_\zeta - x''\boldsymbol{e}_z\cdot\boldsymbol{e}_\zeta}{\boldsymbol{e}_y\cdot\boldsymbol{e}_\xi}
\end{aligned}
\tag{6.8}
$$

The constitutive equations are set up to relate one (un)deformed state to another deformed state, shown in Equation (6.9). These equations are assembled in an ordinary differential equations solver to obtain the new local twist distribution β_L and the new x- and z-coordinate distribution of the blade axis.

$$
\begin{aligned}
\beta'_L &= \beta'_{L0} - \frac{M_\xi - M_{\xi 0}}{GI_\xi} \\
x'' &= \left(\frac{1}{\rho_{\eta 0}} + \frac{M_\eta - M_{\eta 0}}{EI_\eta}\right)\boldsymbol{e}_\zeta \cdot \boldsymbol{e}_x + \left(\frac{1}{\rho_{\zeta 0}} + \frac{M_\zeta - M_\zeta 0}{EI_\zeta}\right)\boldsymbol{e}_\eta \cdot \boldsymbol{e}_x \\
z'' &= \left(\frac{1}{\rho_{\eta 0}} + \frac{M_\eta - M_{\eta 0}}{EI_\eta}\right)\boldsymbol{e}_\zeta \cdot \boldsymbol{e}_z + \left(\frac{1}{\rho_{\zeta 0}} + \frac{M_\zeta - M_\zeta 0}{EI_\zeta}\right)\boldsymbol{e}_\eta \cdot \boldsymbol{e}_z
\end{aligned}
\tag{6.9}
$$

The system of Equation (6.9) allows one to connect one deformed state to another undeformed state using the initial internal moments M_0 and $\frac{1}{\rho_0}$. To go from an undeformed state to a deformed state, the internal moments M_0 are set to zero. When no internal moments are applied, both M_0 and M are zero. Integration of the blade initial state β_{L0}, $\frac{1}{\rho_0}$ will return the initial blade axis coordinates. To go from a deformed state 1 to a deformed state 2. The initial moments M_0 correspond to the internal moments at state 1, and the blade initial states β_{L0} and $\frac{1}{\rho_0}$ correspond to the twist and curvatures of the blade at state 1.

The contributions to the normal stresses within the blade consist of the axial forces (mainly centrifugal) and the two bending moments M_η and M_ζ, thus the total normal stresses within the blade are calculated with Equation (6.10). The shear stress consists only of the torsional moment M_ξ, calculated with Equation (6.11). The total stresses within the blade are expressed using the Von Mises stress, defined in Equation (6.12).

$$
\sigma = \frac{(\boldsymbol{q}_a + \boldsymbol{q}_c)\cdot\xi}{A_L} + \frac{M_\eta \eta}{I_\eta} - \frac{M_\zeta \zeta}{I_\zeta} \tag{6.10}
$$

$$
\tau = \frac{2M_\xi}{I_\xi}|\nabla \bar{U}| \tag{6.11}
$$

$$
\sigma_{VM} = \sqrt{\sigma^2 + 3\tau^2} \tag{6.12}
$$

6.2. EB ASSUMPTIONS & LIMITATIONS

The assumptions and limitations of the Euler-Bernoulli (EB) tool are summarised and some of the potential effects on the results are discussed.

- The propeller blades should be slender such that the length is an order of magnitude higher than the chord length. This is a limitation of the Euler-Bernoulli beam theory.
- The deformations should remain small. Accurate bending of up to 15% of the blade radius and torsion of up to 6° has been validated by Sodja et al. [21].
- Warping effects due to torsion are neglected as they are expected to be small [20].
- The cross-section is assumed to be solid. Detailed propeller structures with stringers and ribs can not be evaluated with the current structural model. With the cross-section being solid, the moment of inertia will be overestimated compared to a real propeller structure. The sectional mass is also significantly increased, increasing the centrifugal forces.
- The material is assumed to be isotropic. Anisotropic materials such as composites can not be applied. This makes the results obtained in this research less applicable to current propellers, which are often made of composites.
- Any axial deflections elongating the propeller blade are neglected.

7

Discipline Couplings

Since the outcome of one discipline may impact the results of another discipline, couplings are required to find a converged state. In this chapter, all the required couplings are identified and explained. Section 7.1 starts with the coupling between the aerodynamic and structural disciplines. The acoustic couplings with the other disciplines are explained in Section 7.2. The final architecture which will be used to analyse propeller designs is shown in Section 7.3 in the form of an XDSM diagram.

7.1. Aerodynamic and Structural Coupling

The aerodynamic and structural tools are directly coupled as their results impact each other. The aerodynamic loads cause a change in structure, this change in blade geometry will cause a change in aerodynamic loads. As such, a coupling is required to find the equilibrium position of the structure so that the aerodynamic loads stay constant and do not change the structure any further.

The aerodynamic and structural tools can be coupled iteratively using the constitutive equations of the structural model, shown again below in Equation (7.1). These equations allow for the calculation of one deformed state to the next deformed state. A converged aerodynamic and structural solution should then result in a propeller blade that does not deform any further, as the initial state internal moments M_0 and the new internal moments M should be equal. As such, the $\frac{M-M_0}{EI}$ should reduce to zero, and the system of differential equations will return the initial blade axis geometry.

$$
\begin{aligned}
\beta_L' &= \beta_{L0}' - \frac{M_\xi - M_{\xi 0}}{GI_\xi} \\
x'' &= \left(\frac{1}{\rho_{\eta 0}} + \frac{M_\eta - M_{\eta 0}}{EI_\eta}\right)\boldsymbol{e}_\zeta \cdot \boldsymbol{e}_x + \left(\frac{1}{\rho_{\zeta 0}} + \frac{M_\zeta - M_\zeta 0}{EI_\zeta}\right)\boldsymbol{e}_\eta \cdot \boldsymbol{e}_x \\
z'' &= \left(\frac{1}{\rho_{\eta 0}} + \frac{M_\eta - M_{\eta 0}}{EI_\eta}\right)\boldsymbol{e}_\zeta \cdot \boldsymbol{e}_z + \left(\frac{1}{\rho_{\zeta 0}} + \frac{M_\zeta - M_\zeta 0}{EI_\zeta}\right)\boldsymbol{e}_\eta \cdot \boldsymbol{e}_z
\end{aligned} \tag{7.1}
$$

However, a simple iterative aerodynamic and structural coupling yields undesired behaviour, as shown in Figures 7.1 and 7.2. Starting from the undeformed state, the blade deforms due to the aerodynamic and inertial loads. With no damping or relaxation factors applied, the blade deformations jump around the converged solution, slowly diverging as the deflections get bigger. This can continue until the blade has deformed such that it becomes unusable in the propeller framework.

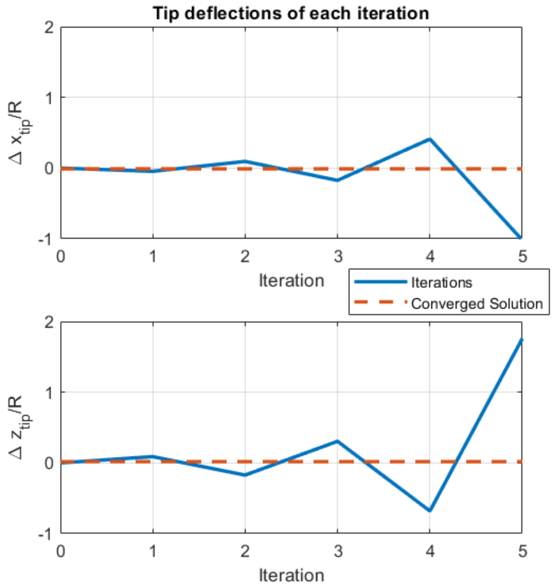

Figure 7.1: The difference in tip deflection after each iteration

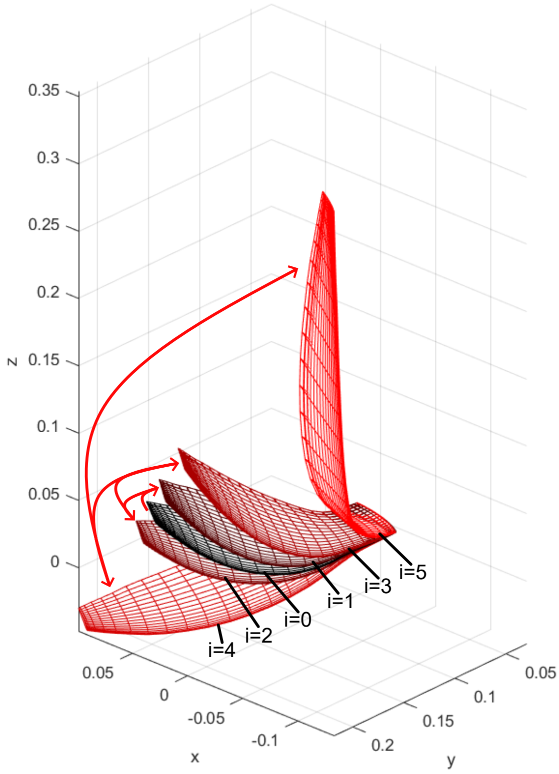

Figure 7.2: The blade geometry after each iteration

Clearly, some type of damping is required to restrict the coupling from diverging. Two different types of relaxation factors were applied to be able to get the system to converge. Firstly, the jump from the undeformed blade to the initial deformed blade was found to be too big for highly swept blades due to the inertial forces. As such, the propeller's RPM is increased slowly from 0 to the desired RPM using a relaxation factor α_{RPM} which slowly increases from 0 to 1. This is done only in the structural solver such that the new inertial forces are calculated with Equation (7.2). Thus the aerodynamic solver still uses the final RPM setting.

$$\begin{gathered}\boldsymbol{q}_c = \rho_b dV(\alpha_\Omega \Omega)^2 r\boldsymbol{e}_r, \\ \text{with } 0 \leq \alpha_\Omega \leq 1\end{gathered} \tag{7.2}$$

The implementation of α_Ω reduces the tendency for the system to diverge. Nevertheless, divergence is still possible at high RPM settings. Furthermore, consecutive analyses at the final RPM setting will still make the system diverge. This is because the $M - M_0$ terms in Equation (7.1) rarely reduce to exactly zero. This residual will cause the system to oscillate around the converged solution again, eventually diverging. To counter this behaviour, the relaxation factor α_d is also added to the applied deformations. The blade shape found from the differential equation system of Equation (7.1) is thus not directly used, instead, a fraction of these deformations is taken to find a new blade shape, shown in Equation (7.3). α_d is initially set to 0.15. This factor is reduced further if the deformations start to increase again during the final converging iterations.

$$\begin{aligned}\beta_{i+1} &= \beta_i + \alpha_d(\beta_{deformed} - \beta_i) \\ x_{i+1} &= x_i + \alpha_d(x_{deformed} - x_i) \\ z_{i+1} &= z_i + \alpha_d(z_{deformed} - z_i)\end{aligned} \tag{7.3}$$

The combination of the relaxation factors α_Ω and α_d resulted in the most stable behaviour of the aerodynamics-structures coupling. Furthermore, the amount of iterations required to reach convergence is significantly reduced compared to using only one of the relaxation factors.

7.2. Acoustic Coupling

The acoustic tool requires the results of both the aerodynamic and structural solvers to calculate the noise emissions. From the VLM tool, the aerodynamic force coefficients of each panel are required as inputs to the radial and chordwise loading distributions. The final shape of the propeller blade, in particular the face and mid-chord alignment are obtained from the structural tool.

The acoustic signature has no impact on the aerodynamic or structural performance of the propeller. As such, the acoustic tool does not need to be included in some form of iterative scheme. Instead, the acoustic tool only needs to be run after the aerodynamics-structural coupling is done.

7.3. Analysis Architecture

An XDSM diagram is constructed to schematically show the coupling between the three tools. The diagram is shown in Figure 7.3. This XDSM diagram shows a converger receiving an initial propeller as input. This propeller data is first given to the aerodynamics discipline, which calculates the aerodynamic loads q_a. The propeller geometry and the aerodynamic loads are given to the structural discipline. The structural tool calculates a new propeller geometry, which has deformed due to the loads. The new propeller geometry is given back to the converger. This loop keeps repeating until the propeller geometry has converged. Only after this converger loop is done will the acoustics discipline be activated. The acoustics tool receives the converged propeller and aerodynamic load data. The noise emissions in the form of SPL and TSSP are then calculated, finishing the entire analysis.

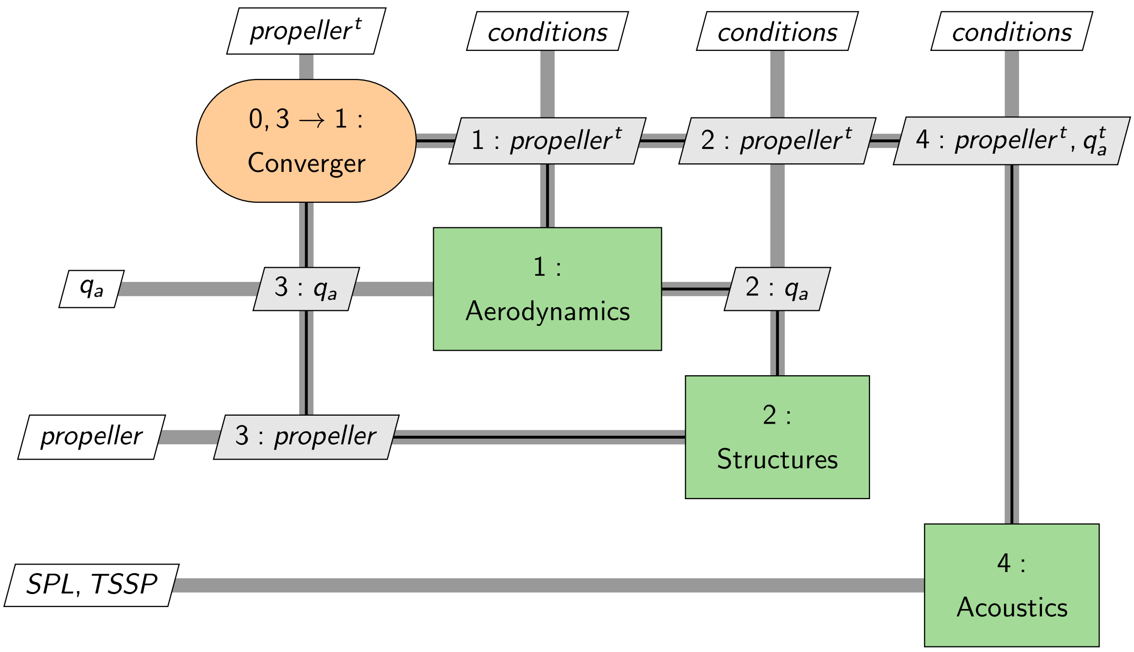

Figure 7.3: XDSM Diagram of the performance calculations of a fully elastic propeller.

III

Tool Error Analysis

8

Grid Convergence Study

In this chapter, the ideal configuration for the propeller blade discretisation is found. The propeller blade is discretised into spanwise, chordwise, and wake panels. The minimum grid required for convergence is determined by slowly increasing the grid density for each tool, and comparing the results to the results of a very fine grid simulation. The grid sensitivities of the aerodynamic, structural and acoustic tools are shown in Sections 8.1, 8.2 and8.3 respectively.

8.1. Aerodynamic Grid Convergence

The aerodynamic tool depends on all three grid parameters; N_s, N_c and N_w. To find the sensitivity of the aerodynamic tool to all three grid parameters, propeller geometries with all possible grid size combinations are input into the aerodynamic tool. The resultant C_T and C_P are compared to the results with a fine grid of $N_s = 72$, $N_c = 72$ and $N_w = 200$. The characteristics to identify are the errors of $C_T/C_{T,fine}$, $C_P/C_{P,fine}$ and the rate at which this error reduces. Shown in Figure 8.1 are the errors of C_T for the three combinations of couples of N_s, N_c and N_w. These combinations are plotted to see if there are any interactions between the grid parameters. For N_s, the aerodynamic tool quickly converges with only 20 panels. Significantly more chordwise panels are required to reduce the errors. Though the error only reduces to exactly zero when the maximum amount of chordwise panels is reached, with 40 panels the error has been decreased sufficiently. The addition of wake panels is relatively cheap in terms of computational time. Regarding the error, only 60 panels are sufficient for the tool to converge.

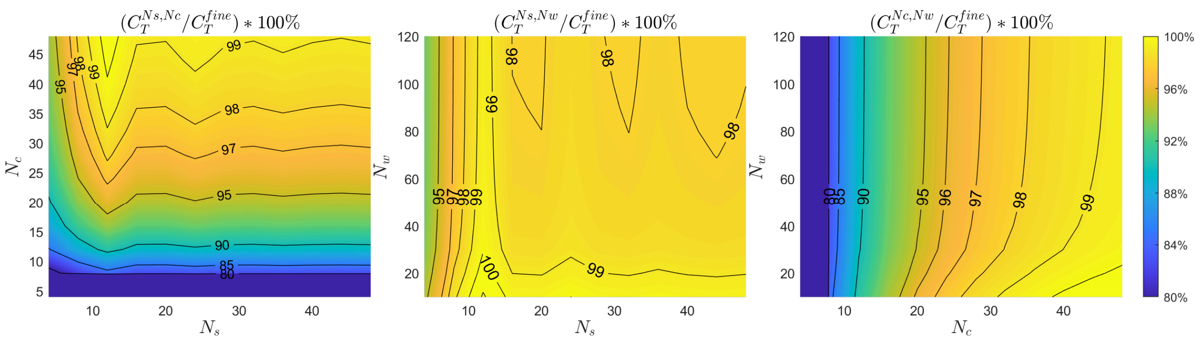

(a) N_s vs N_c (b) N_s vs N_w (c) N_c vs N_w

Figure 8.1: Grid convergence of the VLM tool for all three grid parameters.

8.2. Acoustic Sensitivity Analysis

The acoustic tool is only a function of N_s and N_c. The amount of wake panels N_w will only affect the acoustic results due to a change in aerodynamic loads. The acoustic tool is isolated from the aerodynamic tool to determine the convergence rate however. This is done by interpolating fixed aerodynamic results at N_s and N_c positions. Thus the convergence grid will show if having more radial and chordwise stations will increase the tool's accuracy. The error of the maximum SPL for various amounts of span and chord panels is shown in Figure 8.2. It can be seen that the error is almost negligible already at most grid configurations. The problem is that the behaviour is inconsistent from one grid configuration to the next if the amount of panels is low. As such, for the tool to be stable, at least 24 spanwise panels are required, and 32 chordwise panels.

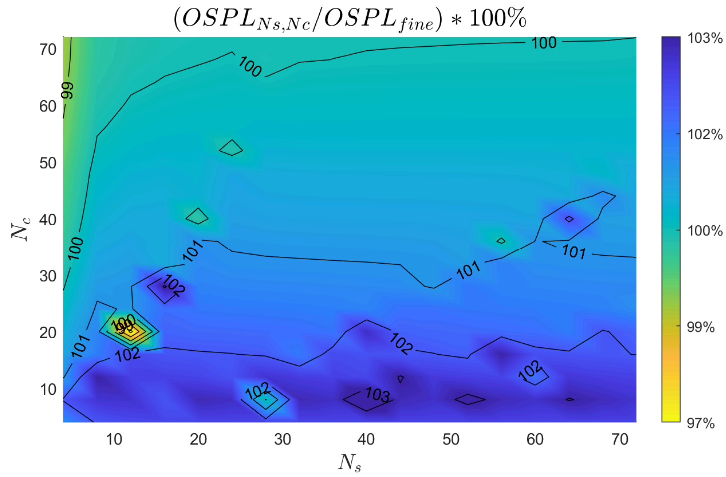

Figure 8.2: Grid convergence of the acoustic tool for N_s and N_c.

8.3. STRUCTURAL SENSITIVITY ANALYSIS

The structural tool has an interesting relation with each grid parameter. It is mainly the amount of span panels that should affect the convergence of the structural tool. A higher N_s will discretise the forces more and calculate the deflections at more radial stations. The amount of chord panels will dictate the accuracy of the moment of inertia calculations, as this is done using the cross-section at each radial station. The number of wake panels does not directly affect the structural tool; it only does so through a change in aerodynamic loads in the aerodynamic solver. The structural tool is isolated from the aerodynamic solver by replacing the aerodynamic loads with a constant distributed load. Propellers with varying amounts of span and chord panels are then input into the structural tool. The results of each propeller size are compared to the results of the finest propeller. The error of the total tip deflection δ_{tip} and twist deformation β_{tip} are shown in Figure 8.3. It can be seen that significant errors occur if the amount of span panels is set too low. However, these errors quickly reduce, with an error of less than 2% with a minimum of 32 span panels. The error only reduces to zero when the maximum amount of spanwise panels is reached. In terms of the chordwise panels, only 20 panels are required for the tool to converge.

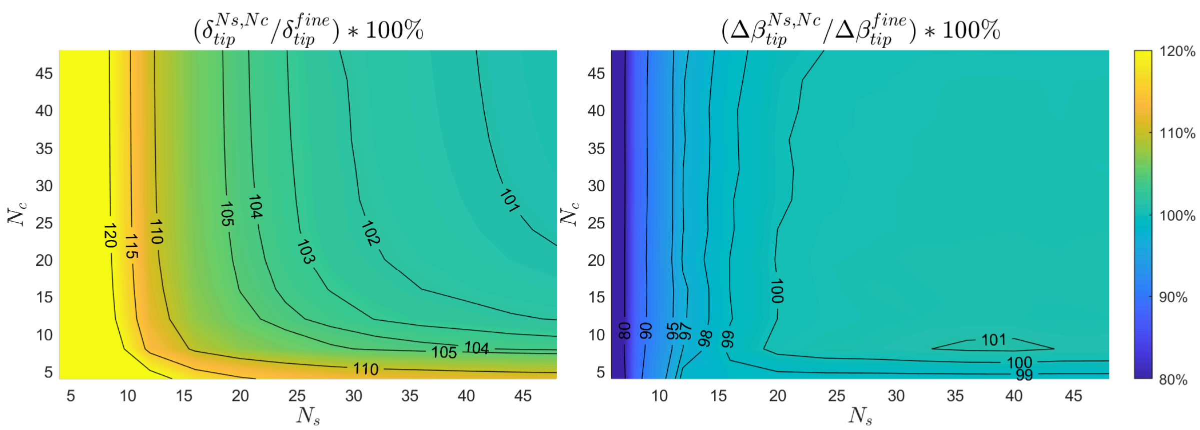

(a) Sensitivity of grid size to bending deformations at the tip

(b) Sensitivity of grid size to twisting deformations at the tip

Figure 8.3: Grid convergence of the structural tool for N_s and N_c.

8.4. FINAL GRID SIZE

A final grid is chosen based on the grid convergence analyses of the previous sections. It is important to not set the grid too fine, as this will significantly increase computational time. The errors of some tools do not reduce to zero unless the maximum amount of panels is reached however. As such, a maximum boundary of 2% error compared to the fine mesh results is imposed. This results in the required grid configurations of each tool as shown in Table 8.1. Since the minimum number of panels for each discipline is relatively similar, a constant grid can be chosen. This grid can then be used throughout the workflow, and results do not need to be interpolated between disciplines. The highest minimum grid number for each parameter is taken to obtain the final grid size of the propeller; $N_s = 32$, $N_c = 40$, $N_w = 60$.

Discipline	N_s	N_c	N_w
Aerodynamics	30	40	60
Acoustics	24	32	N.A.
Structures	32	20	N.A.

Table 8.1: Minimum required panels for each discipline.

9

Tool Validation

In this chapter, each tool is validated against experimental or high-fidelity data. By first validating each tool individually, the accuracy and suitable conditions are determined. The coupling between each tool is also validated to check whether these couplings have been implemented correctly.

9.1. Aerodynamic Tool Validation

The aerodynamic VLM tool is validated using both CFD and experimental data. Considering a wide range of operating conditions is important since no viscous effects have been added to the numerical tool. As such, it is expected that significant errors may occur when viscous effects are significant, such as during high loading and windmilling conditions. The VLM tool is extensively validated against multiple XPROP data sets. The XPROP propeller is a simple straight propeller for which an abundance of high-fidelity and experimental data is available. The geometry of the XPROP propeller is described in Ref [25].

9.1.1. CFD Validation

CFD simulations of a 50% scale XPROP have been done Van Arnhem [25]. The results of these simulations are compared to results calculated by the VLM in Figure 9.1. It can be seen that the VLM results match almost perfectly between $1.4 \leq J \leq 2.2$. The flow separation at $J \leq 1.4$ present in the CFD simulations are clearly not captured by the VLM tool, as there is no viscosity correction present. Near the zero-thrust condition, the flow is also highly viscous, and thus the VLM tool also loses accuracy compared to the CFD data. The errors in C_T and C_P are compounded in the efficiency, thus resulting in bigger differences between the VLM and CFD results. Nevertheless, at maximum efficiency ($J = 2$), the results are near-identical.

Local force distributions are also available from the CFD simulations. These can be compared to the distributions obtained by the VLM tool to validate not only the global performance but also local forces. Figure 9.2 shows a comparison of the dC_T/dr and dC_Q/dr distributions for two operating settings. $J = 1.40$ occurs just before flow separation occurs. $J = 2.00$ is the point of maximum efficiency. It can be seen that for both settings, the CFD simulations predict a higher tip loading, with the peak being closer to the tip. Despite the differences in local force distributions, the overall performance of the propeller is nearly identical, as was seen in Figure 9.1. It is important to keep this discrepancy in local forces in mind, as it could impact the noise predictions.

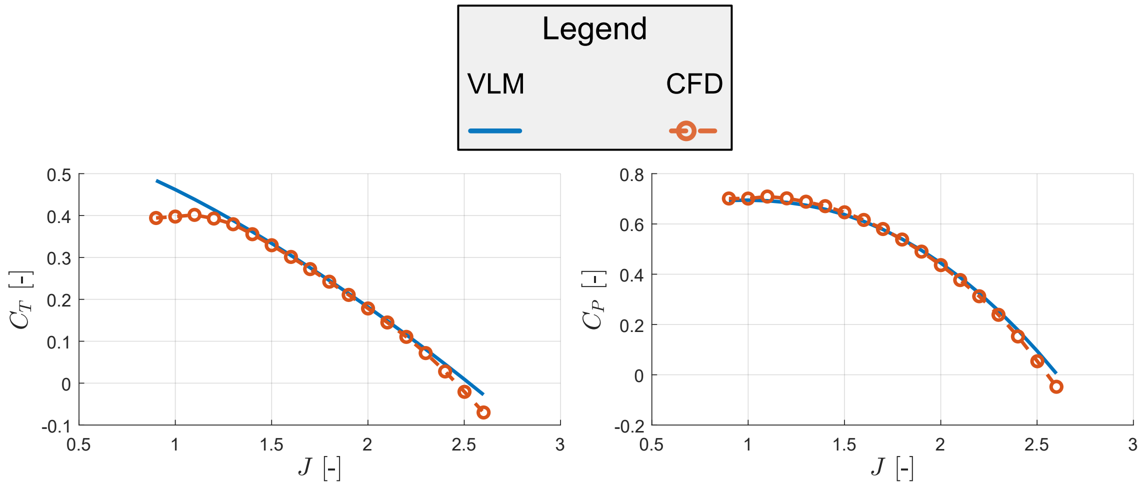

(a) Thrust Coefficient (b) Power Coefficient

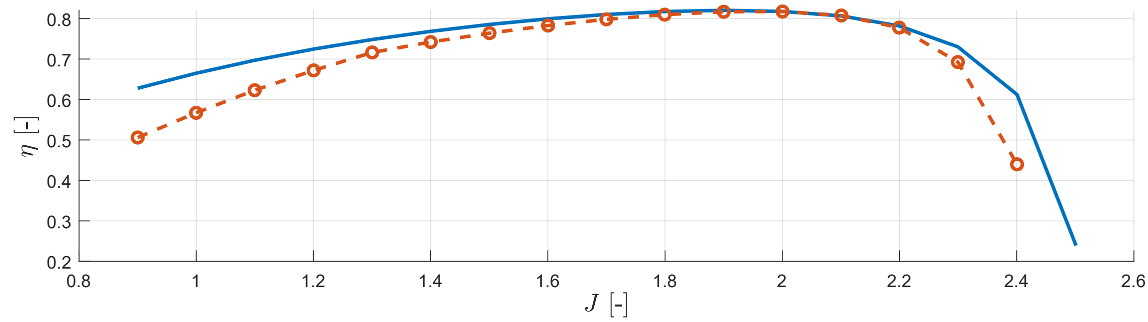

(c) Efficiency

Figure 9.1: Comparison of XPROP performance curves calculated by VLM and CFD.

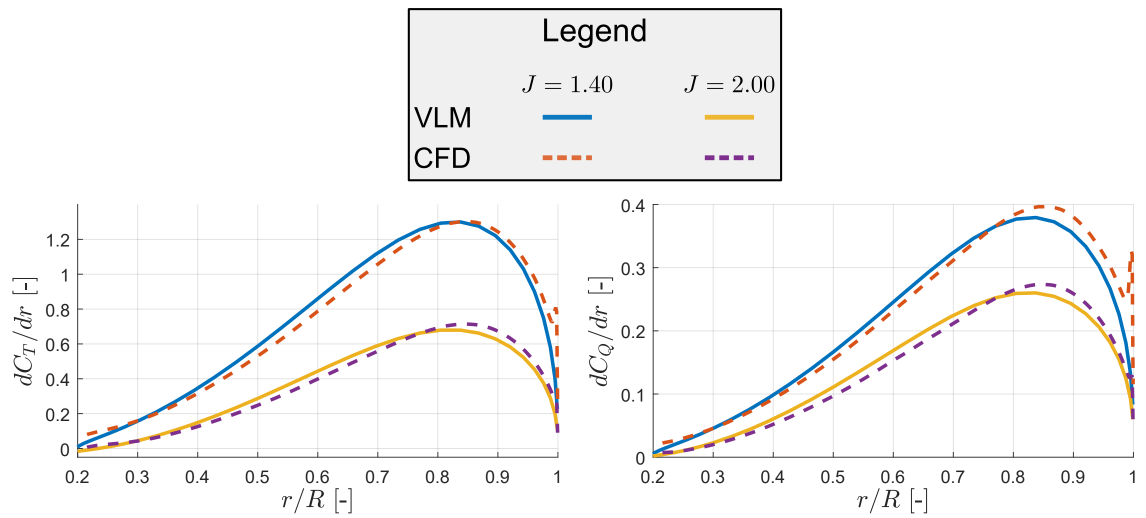

(a) Thrust Distribution (b) Torque Distribution

Figure 9.2: Comparison of XPROP local force distributions calculated by VLM and CFD.

9.1.2. EXPERIMENTAL VALIDATION

A considerable amount of wind tunnel data is available for the XPROP propeller. The test campaigns of Stokkermans and Veldhuis [26], Li et al.[27] and Van Arnhem et al.[28] are combined to obtain a wide range of operating conditions. The comparison of VLM results and this experimental data is shown in Figure 9.3. Three different operating settings are used. Generally, the VLM tool overestimates the thrust, and underestimates the power. This results in an overprediction of the efficiency across the entire operating range. The difference between VLM and experimental data increases as the thrust coefficient nears 0, indicating an increase of viscous effects. Flow separation can also be seen at low advance ratios when the pitch is set to $\beta_{0.7R} = 45°$. This is not captured by the VLM tool.

Nederlof et al.[29] completed a full test campaign of the XPROP, focusing on the negative thrust conditions. Since the VLM tool does not have any viscosity corrections, results in the negative thrust condition will be inaccurate and will thus not be compared. Instead, only the positive thrust region is compared, delving slightly into the negative thrust condition to compare the transition point of positive thrust to negative thrust. The comparison of the VLM tool and Nederlof's experimental data is shown in Figure 9.4. It can be seen that the inaccuracies of the VLM tool increase as the negative thrust condition is approached. The exact advance ratio at which this transition occurs is overpredicted, as the potential flow predictions remain linear while the experimental data changes in slope due to the highly viscous flow. The regions of positive thrust when $\beta_{0.7R} = 25°$ and $\beta_{0.7R} = 30°$ do show better agreement between the VLM tool and experimental data.

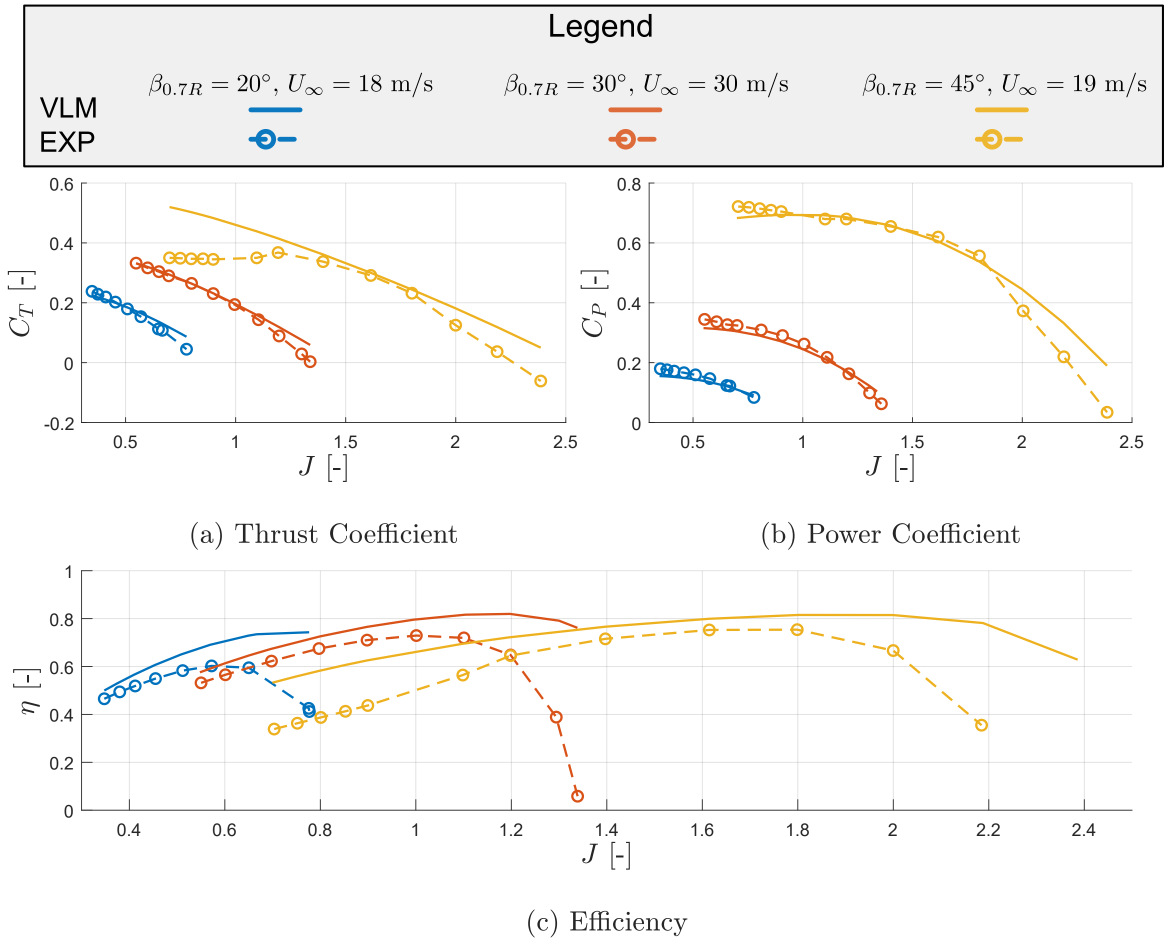

Figure 9.3: Comparison of XPROP VLM and experimental results. (Data from Stokkermans and Veldhuis [26], Li et al.[27] and Arnhem et al.[28].)

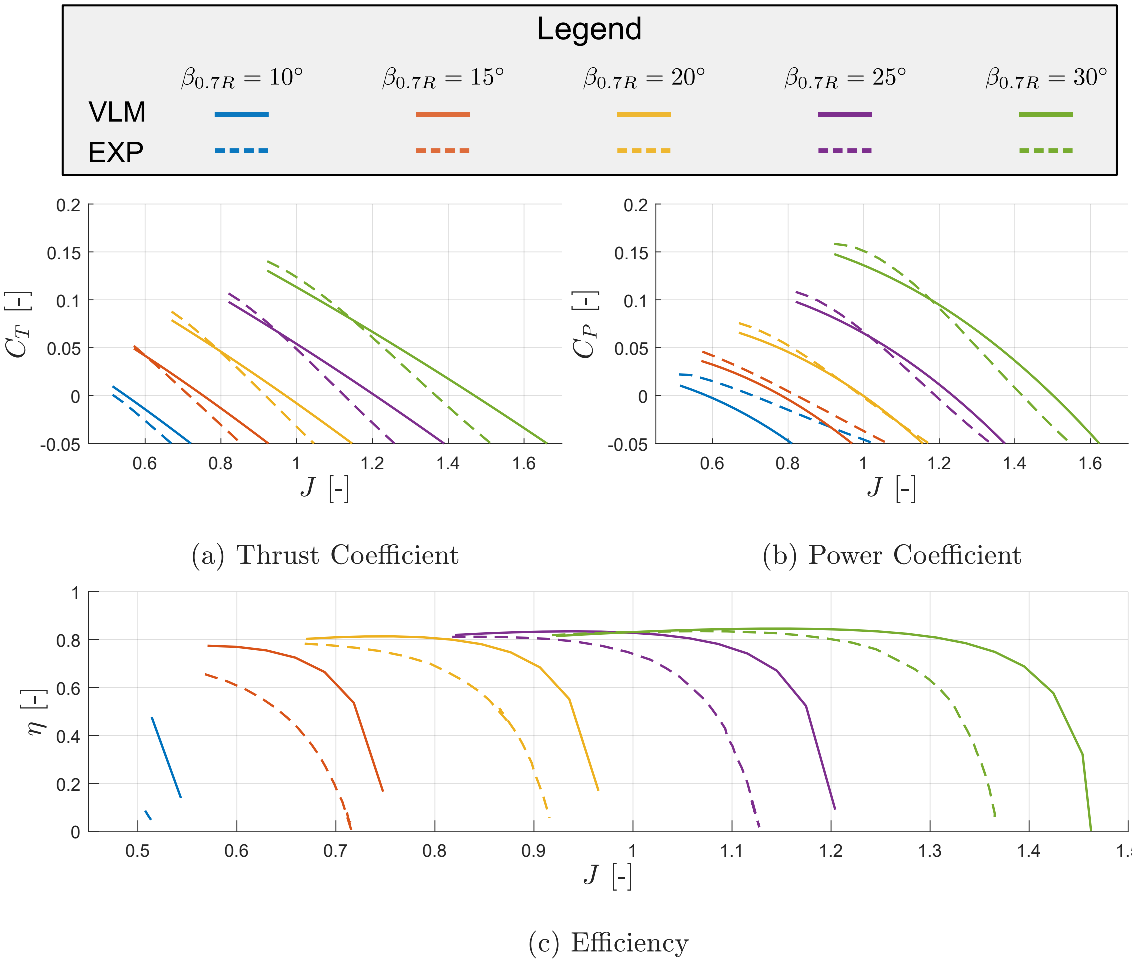

Figure 9.4: Comparison of XPROP VLM results and Nederlof's experimental results [29].

9.2. Acoustic Tool Validation

The acoustic tool has already been validated by Goyal et al.[30], where the HST tool was coupled with a BEM and CFD aerodynamic solver. It was found that the acoustic tool is sensitive to errors from low-fidelity aerodynamic data such as obtained by BEM. This results in inaccurate predictions of noise levels. Nevertheless, the tool is suitable for a comparative analysis of different propellers and operating conditions as it can still predict trends in noise emissions accurately [30].

The coupling between the VLM tool and the HST tool is validated here by comparing the noise directivity to Lattice Boltzmann Method (LBM) data by Goyal et al. [31]. Numerical data was generated using the XPROP for the positive and negative thrust regimes at multiple angles of attack. Broadband noise was also included in the simulation. Figure 9.5 shows the comparison of the noise emissions at zero angle of attack at $J = 0.60$ and $\beta_{0.7R} = 15°$. Figure 9.4 showed that the aerodynamic predictions by the VLM tool for these conditions are accurate. The contributions of the loading and thickness noise are plotted separately. The VLM+HST coupling shows good agreement for these noise sources with the LBM data for axial directivity angles between 45° and 135° degrees. The broadband noise becomes the main noise source beyond these directivity angles, which is not modelled by the HST tool. The total noise agreement is slightly worse. This may be due to differences in the interference pattern. Goyal et al. [30] already stated that any differences in local loading distribution can result in observable differences in acoustic emissions. Furthermore, Section 9.1 already showed that the local loading distributions calculated by the VLM tool differs slightly from high-fidelity data. As such, differences between this low-fidelity method and high-fidelity data are to be expected.

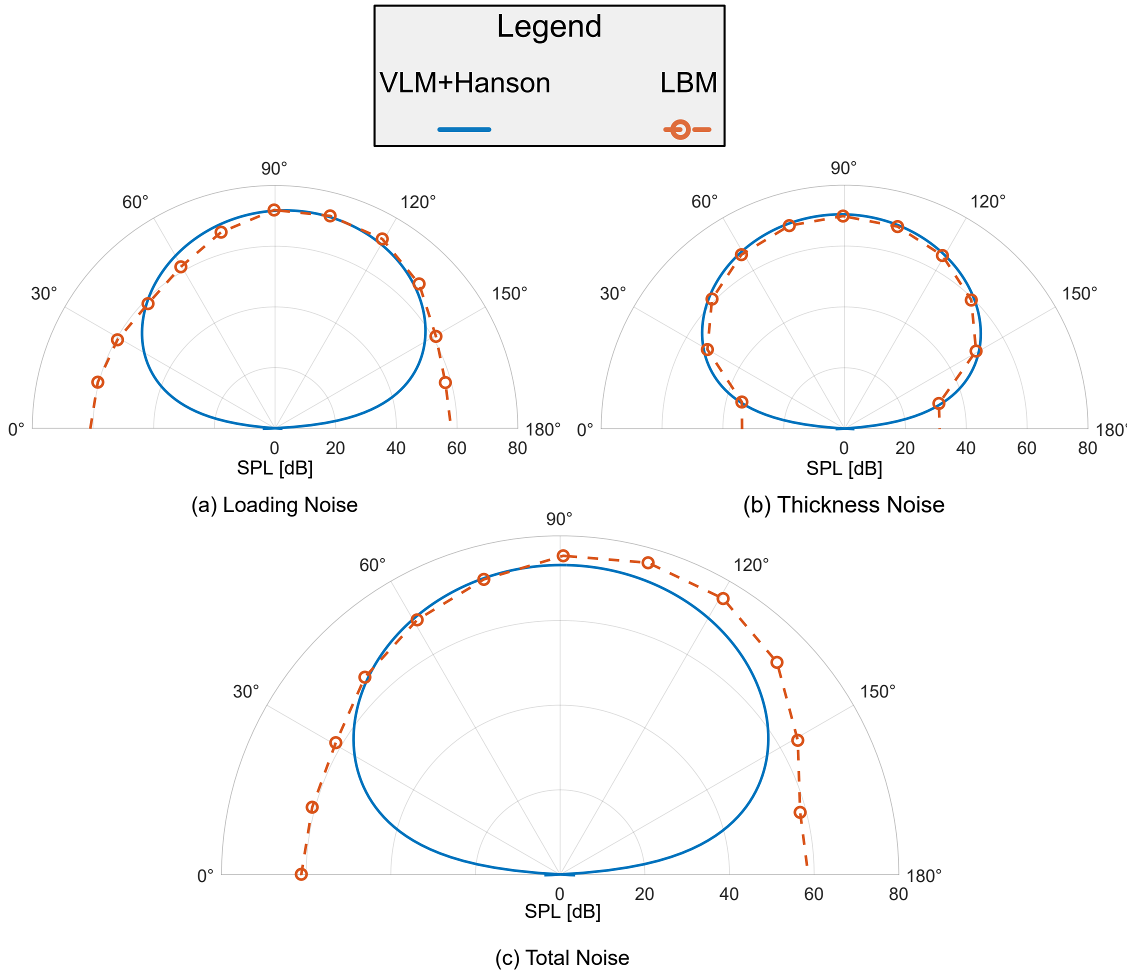

Figure 9.5: Comparison of noise directivity calculated by VLM+HST and LBM simulations (Data from Goyal et al. [31]).

9.3. STRUCTURAL TOOL VALIDATION

The Euler-Bernoulli structural tool has been extensively validated by Sodja et al. [20, 21]. It was found that the low-fidelity structural tool can accurately predict the general behaviour of straight, forward-swept and backwards-swept blades. Coupled with a BEM aerodynamic model, the aerodynamic-structures coupling successfully captured aeroelastic effects [21]. The propeller framework of this research and the one used by Sodja et al. are fundamentally different [20, 21]. This has been accounted for in the implementation of the structural tool. Some additional validation is performed in this section to ensure the structural tool works correctly with the propeller framework employed for this research. This validation is done in the form of FEM simulations using Ansys.

A swept version of the XPROP propeller is generated using the propeller framework. This geometry is then imported into Ansys. Point loads are applied at the propeller tip, and the results of the EB tool and FEM simulations are compared.

The comparison between the EB tool and the FEM simulations is shown in Figure 9.6. It can be seen that the bending deformations, Δ_x and Δ_z, show very good agreement between the two methods. The bending coupling is also captured successfully, with a tipload in a single direction causing deflections in both x and z. The twisting deformations $\Delta\beta$ show similar trends between the EB tool and FEM simulations. The EB tool estimates higher torsion along most of the blade but ends up underestimating the torsion at the tip.

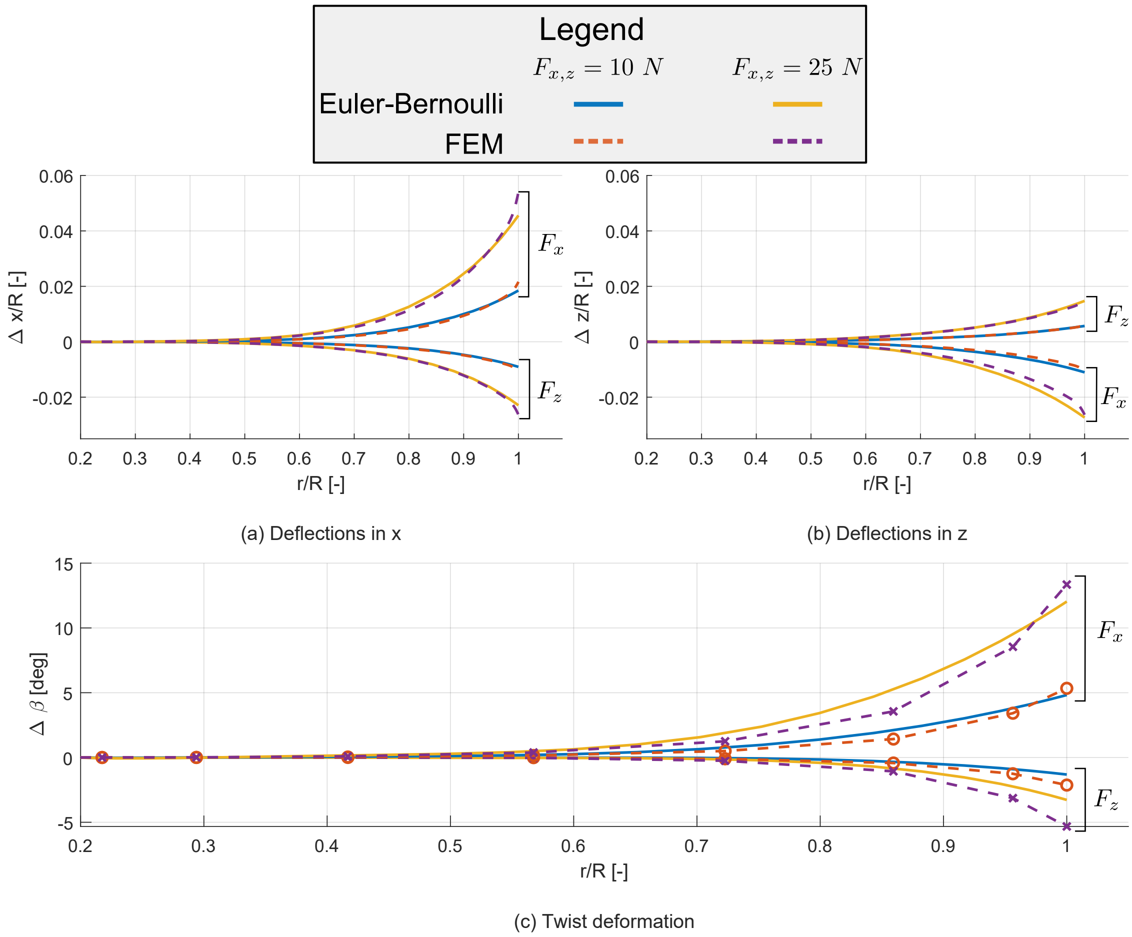

Figure 9.6: Comparison of structural deflections due to a tipload calculated by the EB tool and Ansys FEM simulations.

9.4. AERODYNAMICS-STRUCTURES COUPLING VALIDATION

It is possible to validate the coupling of the aerodynamic and structural tool by using data from Sodja et al. [21]. In this paper, CFD and FEM were coupled to simulate three different blades; the Straight blade (SB), the Backwards-swept blade (BB) and the Forwards-swept blade (FB). These blades are shown in Figure 9.7. The exact properties of these blades can be found in Ref [21]. Each blade is reconstructed in the propeller framework. However, due to the difference in propeller frameworks, it was not possible to reproduce the blade geometries exactly. As such, it is expected that differences may occur between the results obtained here and those obtained by Sodja et al. [21].

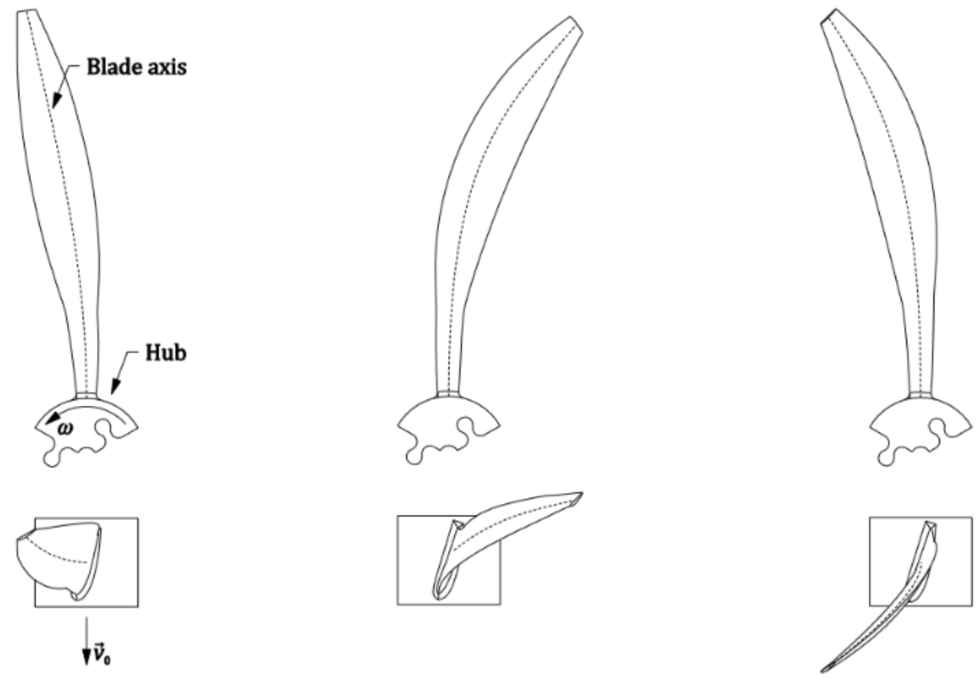

(a) Straight blade (SB). (b) Backwards swept blade (BB). (c) Forward swept blade (FB).

Figure 9.7: Three swept blade designs by Sodja et al. [21].

The deformations of the blades are evaluated at four operating conditions. The structural deformation comparisons between the VLM-EB coupling and the CFD-FEM coupling are shown in Figures 9.8 to 9.10. The aerodynamic results are shown in Figure 9.11, these provide valuable context for the structural deformations.

The bending deformations of the straight blade in Figure 9.8 show very good agreement in terms of bending deformations for all operating conditions. The torsional deformations are significantly underestimated, as was also found by Sodja et al. [21]. For straight blades, the exact position of the chordwise centre of pressure is important as it will dictate whether the blade will twist positively or negatively. The difference in torsional deformations may be due to the VLM inaccurately predicting the centre of pressure location. Nevertheless, the overall aerodynamic performance in Figure 9.11 shows good agreement for C_T, with C_P being underestimated. The flow separation occurring before $J = 1.1$ is not captured. Despite this, the structural deformations at $J = 0.87$ are still very accurate, which could indicate that the inertial forces are dominant for deformations.

In the case of the forwards-swept blade, in Figure 9.9, the VLM-EB coupling generally underpredicts bending deformations. Though clearly the discrepancy for $\Delta x/R$ is bigger than that for $\Delta z/R$. The centrifugal and aerodynamic bending moments are opposite of each other in the x-direction. An underprediction of $\Delta x/R$ would thus indicate an overestimation of the aerodynamic forces or an underestimation of the centrifugal loads. However, the aerodynamic performance in Figure 9.11 generally shows a good agreement, only overestimating the aerodynamic forces after flow separation occurs in the Computational Fluid Dynamics (CFD) data when $J \leq 1.20$. Additionally, the $\Delta z/R$ bending deflections and torsional deformations agree well with the high-fidelity data. Therefore, the cause of the discrepancy in $\Delta x/R$ remains unclear.

The deformations of the backwards-swept blade are shown in Figure 9.10. Significantly bigger discrepancies can be identified here, with an underestimation of the bending deformations and an overestimation of the torsional deformations. It is important to note however that the overall bending deformations of the backwards-swept blade are quite small. The overestimation of the torsional deformations by the low-fidelity model was also found by Sodja et al. [21]. The aerodynamic performance in Figure 9.11 shows an overestimation of both the thrust and power, which could explain the increase in torsional deformations and $\Delta z/R$. Higher aerodynamic forces would also result in more negative $\Delta x/R$ deformations however, which is not replicated in this case. The difference in structural deformations could be attributed to the discrepancies in replicating the propeller geometry using the Smart Rotors propeller framework. With the backwards-swept blade having the most sweep out of all three blades, the geometrical differences are expected to be the most significant. Furthermore, accurate results were obtained using the low-fidelity model by Sodja et al [21]. With the accurate results for the straight and forward-swept blades obtained here and the fact that the underlying mechanics of the model remain the same regardless of the propeller geometry, it is likely a failure to adapt the backwards-swept blade to the Smart Rotors framework is to blame.

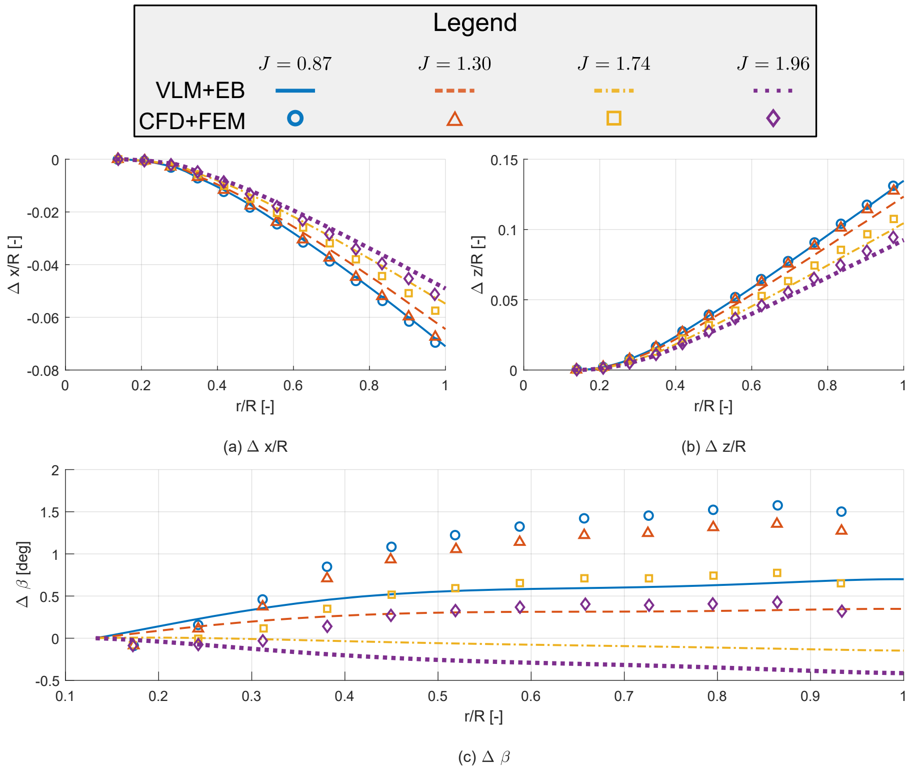

Figure 9.8: Comparison of the structural deformations of the straight blade, calculated by VLM-EB coupling and CFD-FEM coupling. (Data from [21]).

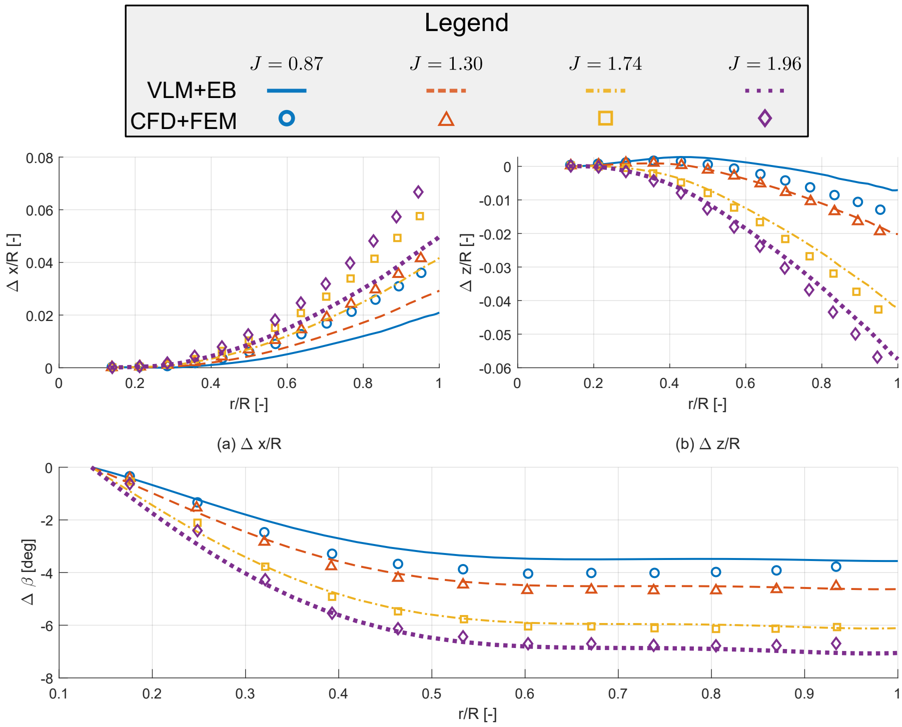

(a) Δ x/R (b) Δ z/R

(c) Δ β

Figure 9.9: Comparison of the structural deformations of the forward swept blade, calculated by VLM-EB coupling and CFD-FEM coupling. (Data from [21]).

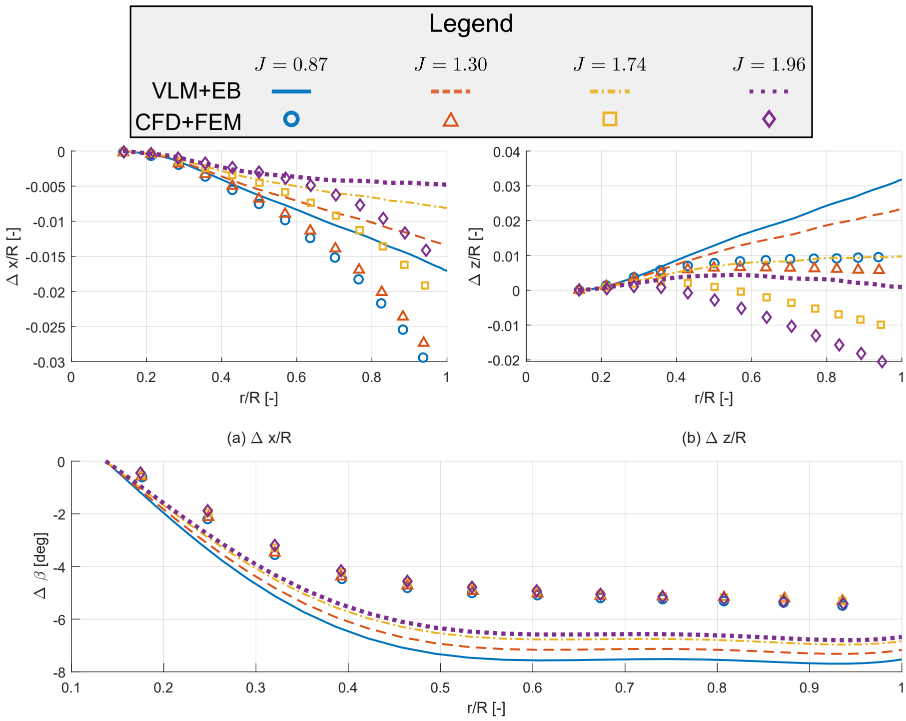

(a) Δ x/R (b) Δ z/R

(c) Δ β

Figure 9.10: Comparison of the structural deformations of the backwards swept blade, calculated by VLM-EB coupling and CFD-FEM coupling. (Data from [21]).

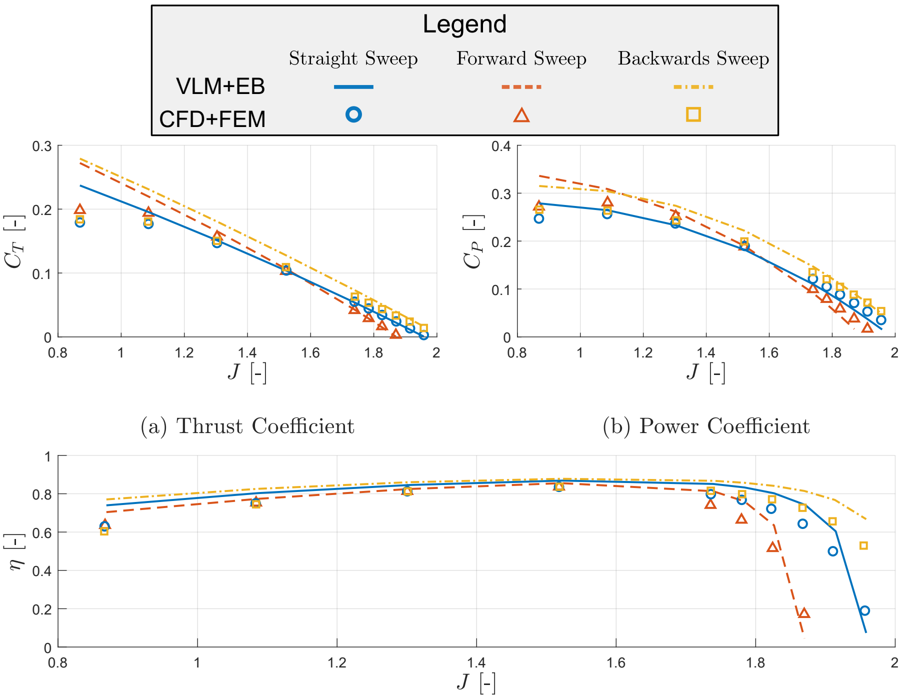

(a) Thrust Coefficient

(b) Power Coefficient

(c) Efficiency

Figure 9.11: Comparison of the aerodynamic performance of three swept blade designs, calculated by VLM-EB coupling and CFD-FEM coupling. (Data from [21]).

IV

Results

10

ANALYSIS SETUP

The parametric study is set up to obtain the relevant data required to achieve the thesis objective. A baseline propeller is first obtained in Section 10.1. The sweep distribution parameterization is defined in Section 10.2. Finally, the exact design space of the parametric study is established in Section 10.3.

10.1. BASELINE PROPELLER

A baseline propeller is required on which varying amounts of sweep angles can be added. This propeller needs to remain within the suitable operating range of the analysis tools. So far, the XPROP has been used often to validate the tools. This has shown that accurate results for this size and operating conditions may be obtained. The research aim is to investigate low-noise propellers, of which the XPROP has no such properties.

Instead, an optimisation study has already been performed using the Smart Rotors propeller framework by G. Margalida[1]. The chord, twist, camber, camber position and thickness distributions were all optimised for noise emissions over three operating conditions. Critically, no sweep or dihedral was added to the propellers. A Pareto front was found where the propeller efficiency has to be traded for noise emissions, as seen in Figure 10.1. Structural constraints were also implemented to limit the stress and bending of the blades. Figure 10.1 highlights a point on the Pareto front where these constraints no longer impact the propeller geometry, and the blade shapes become identical. The propeller found at this point has been chosen as the baseline propeller for this research. At this point, the propeller has decreased noise emissions compared to the XPROP. Structural constraints are not active such that there is some freedom to add blade sweep, which will increase the bending and stress.

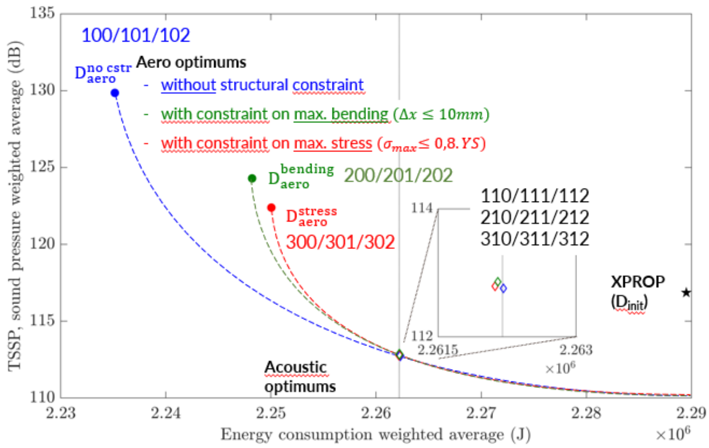

Figure 10.1: Optimisation study of low-noise propeller designs with multiple different constraints. (From Smart Rotors Project [Unpublished])

[1] Smart Rotors Project: Propeller Optimisation by Gabriel Margalida (Accessed in December 2023) [Unpublished]

The propeller geometry is shown in Figure 10.2, with the geometric distributions displayed in Figure 10.3. The operating conditions for which the propeller has been designed are summarised in Table 10.2. To limit the scope of this research, only the pitch setting of the climb conditions will be analysed. This setting has been chosen as this is one of the flight phases in which noise reductions may be most beneficial for the environment. The low-noise propeller was originally designed with aluminium as the material. Since adding sweep may significantly induce extra bending and stresses, the material has been changed to titanium alloy, with the properties shown in Table 10.3. Titanium alloy has been used for experimental swept propellers like those tested in the DNW wind tunnels [2]. It allows for very high stresses, but its lower elastic modulus (compared to steel) should still highlight the effects of structural deformations.

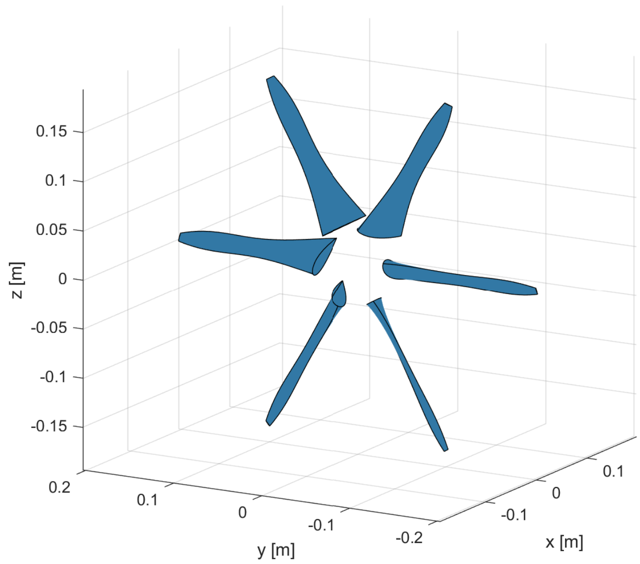

Figure 10.2: Design of the baseline, six-bladed low-noise propeller.

Propeller Properties	
N_b	6
R	0.2032 m
R_h/R	0.1978
$\beta_{0.7R}$	36.2°
y_o	10R

Table 10.1: Properties of the baseline low-noise propeller

Parameters	Take-off	Climb	Cruise
J	0.67	1.09	1.95
U_∞	40 m/s	60 m/s	68 m/s
$\beta_{0.7R}$	25.7°	36.2°	45.2°
ρ	1.225 kg/m^3	1.225 kg/m^3	1.225 kg/m^3

Table 10.2: Operating conditions of the low-noise propeller.

Material Properties	
Material	Ti-6Al-4V
ρ_b	4430 kg/m^3
E	120 GPa
G	44 GPa
ν	0.36
σ_{yield}	1000 MPa

Table 10.3: Material properties of the chosen material [32].

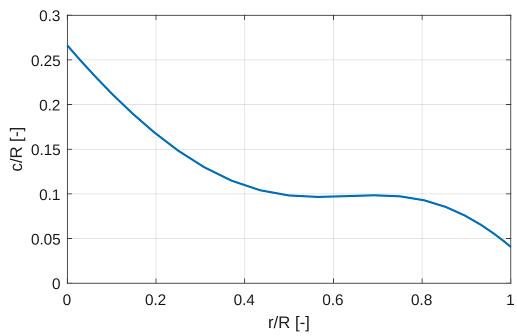

(a) Chord distribution.

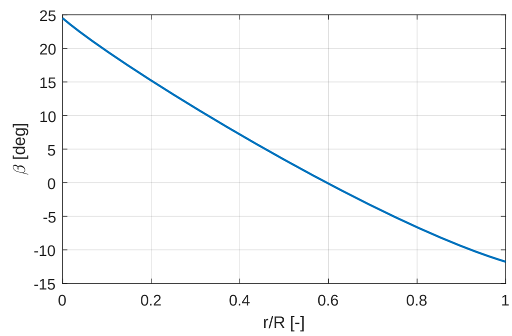

(b) Twist distribution.

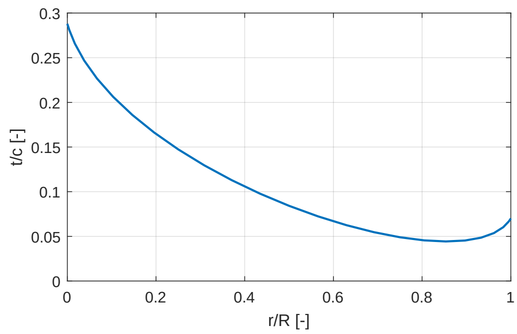

(c) Thickness distribution.

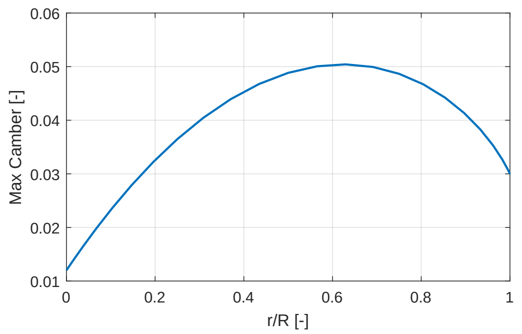

(d) Camber distribution.

Figure 10.3: Baseline propeller geometrical distributions.

10.2. SWEEP PARAMETRISATION

The baseline propeller of Section 10.1 has no sweep applied to it. The goal is to add varying amounts of sweep, and change the sweep distribution, to investigate the impact on the performance. To achieve this, the sweep is parametrised such that it can be simply added to the baseline propeller.

The sweep is parametrised using Equation (10.1), with which the total sweep, the sweep distribution and the forward sweep between the root and tip can be adjusted. Equation (10.1) is the relation between the offset distance z/R and the nondimensional distance from the blade root y/R. The z/R distribution is then applied to centre of gravity distribution at the specific setting of $\beta_{0.7R} = 36.2°$ of the nondimensional blade construct of the propeller framework. By applying it to the centre of gravity distribution at this specific pitch setting, the entire blade will remain within the rotational axis when undeformed. This means that there is no dihedral at this pitch setting. Additionally, the sweep is applied such that the tip of the blade remains on the same actuator disk of the straight propeller, so that the radius of the propeller remains constant.

$$\frac{z}{R} = \Lambda\left(\frac{y}{R}\right)^{d\Lambda} + \kappa\left(\left(\frac{y}{R} - 0.5\right)^2 - 0.25\right) \tag{10.1}$$

The sweep parameterization of Equation (10.1) is determined by three sweep parameters; Λ, $d\Lambda$ and κ. The definitions of these three sweep parameters are shown in Figure 10.4. The tip sweep parameter Λ sets the z/R distance at the tip of the blade. Traditionally the sweep is represented by an angle λ. In this case, $\tan\lambda$ is represented as the linearised amount of sweep at the tip with Λ.
The second sweep parameter, $d\Lambda$, sets the curvature of the sweep distribution between the root and tip. It can be seen in Equation (10.1) and Figure 10.4 that it represents the degree of the monomial. By increasing $d\Lambda$, the sweep distribution between the root and tip changes without increasing the total amount of sweep at the tip. The blade becomes straight near the root and starts to sweep back aggressively near the tip as it is increased. Λ is not an independent parameter however, as no sweep curvature can be applied if there is no tip sweep present. Therefore the slope of the blade tip is represented by $\Lambda d\Lambda$.
The final sweep parameter is κ. This parameter allows for the addition of forward sweep between the root and tip, without altering the total amount of sweep near the tip. The part including κ in Equation (10.1) represents a parabola between $y/R = 0$ and $y/R = 1$. Increasing κ increases the depth of this parabola at

$y/R = 0.5$. The summation of this parabola and the monomial curve described by Λ and $d\Lambda$ then form the final sweep distribution.

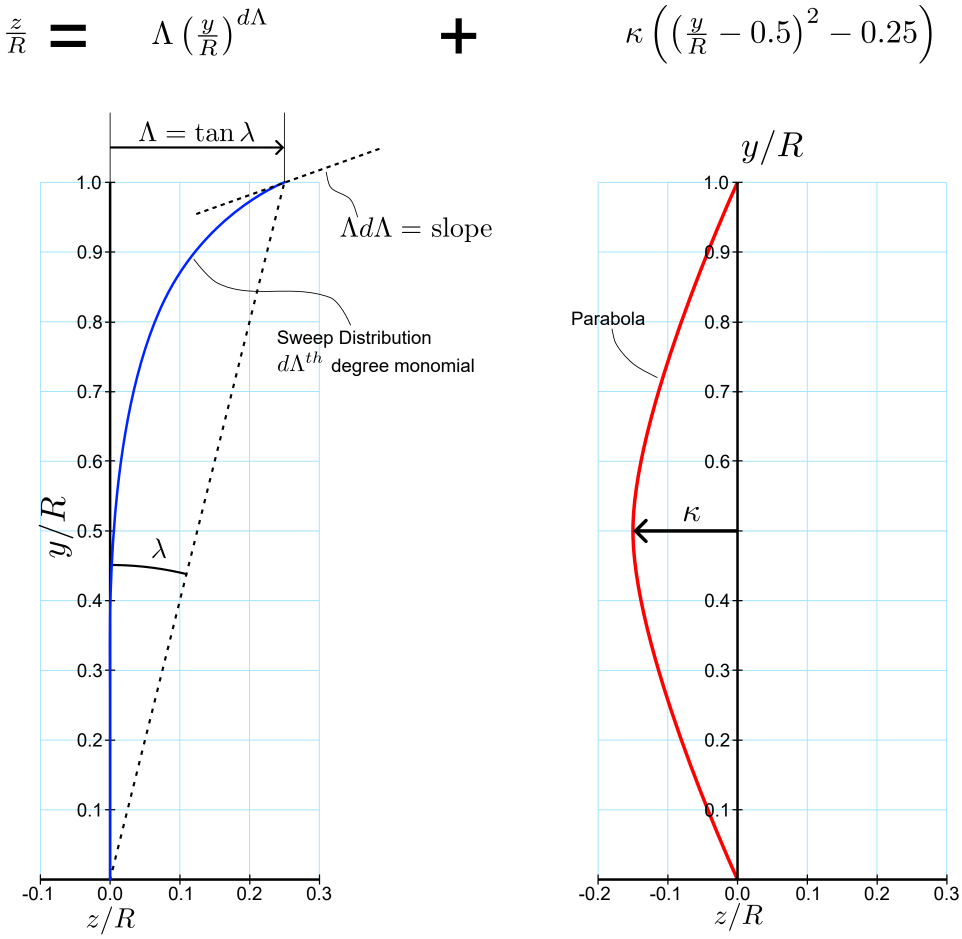

Figure 10.4: Definition of the sweep parameters Λ, $d\Lambda$ and κ.

The ranges of the three sweep parameters are shown in Figure 10.5. Physical propeller geometries with different sets of Λ , $d\Lambda$ and κ are shown in Figure 10.6. The tip sweep Λ ranges from 0 to 0.25. The tip sweep curvature $d\Lambda$ ranges from 1 to 8.0. The forward-backwards sweep parameter κ can be set anywhere between 0 to 0.5.

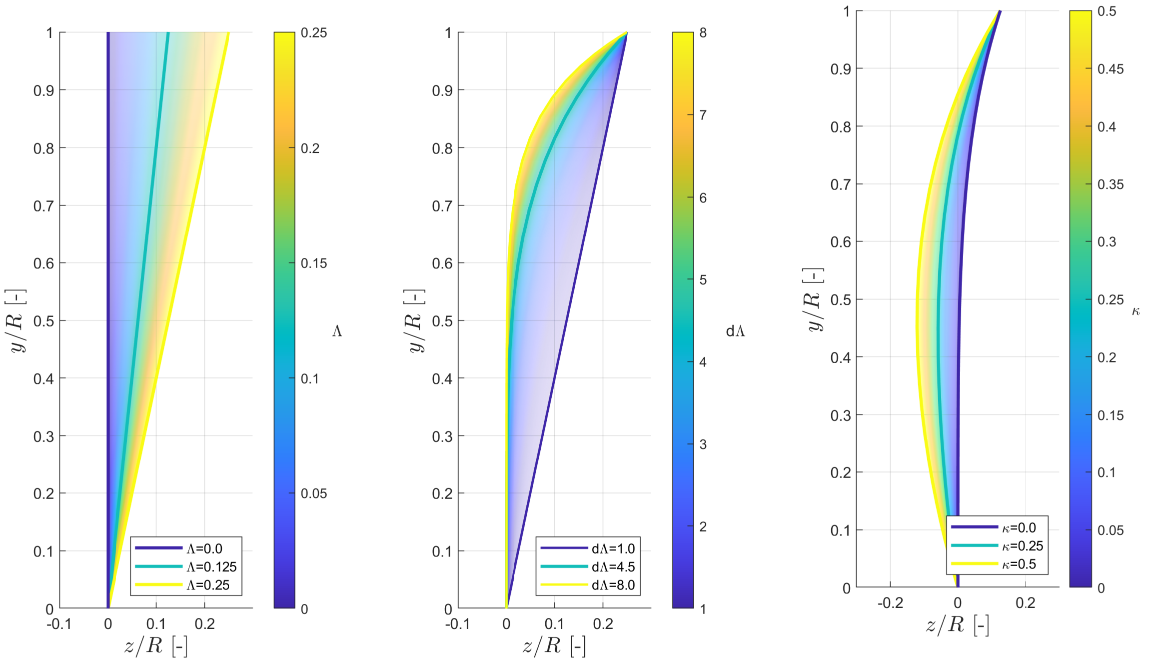

(a) Tip sweep Λ ($d\Lambda = 1.0$, $\kappa = 0.0$) (b) Sweep curvature $d\Lambda$ ($\Lambda = 0.25$, $\kappa = 0.0$) (c) Forwards-backwards sweep κ ($d\Lambda = 4.5$, $\Lambda = 0.125$)

Figure 10.5: Ranges of the three sweep parameters: (a) tip sweep Λ, (b) sweep curvature $d\Lambda$, and (c) forward-backwards sweep κ.

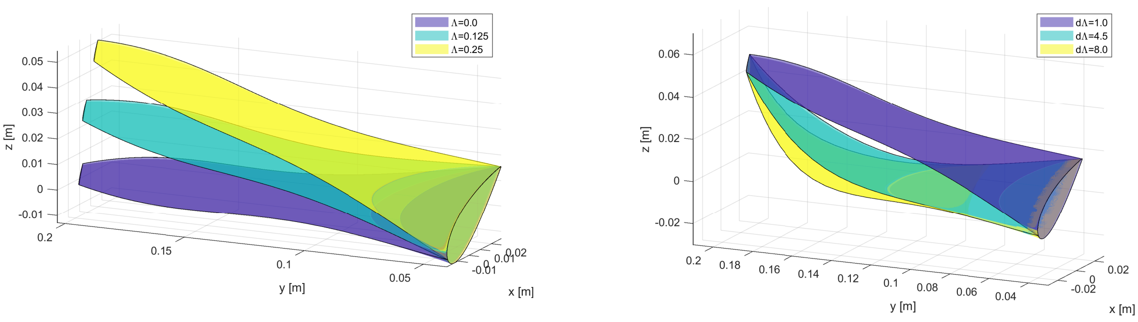

(a) Λ ($d\Lambda = 1.0$, $\kappa = 0.0$) (b) $d\Lambda$ ($\Lambda = 0.25$, $\kappa = 0.0$)

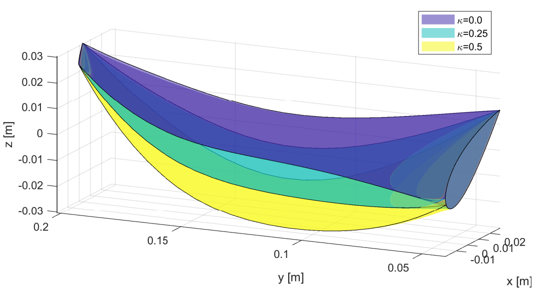

(c) κ ($d\Lambda = 4.5$, $\Lambda = 0.125$)

Figure 10.6: Propeller blades with different Λ , $d\Lambda$ and κ values.

10.3. DESIGN SPACE DEFINITION

The design space consists of the parameters which need to be studied. In this study, the parameters to investigate are the sweep parameters, Λ , $d\Lambda$, κ, and the operating conditions. Many combinations of each of these parameters are then put through the XDSM architecture of Section 7.3 to obtain the aerodynamic, structural and acoustic performance. Critically, the computation time of a complete execution of the XDSM procedure is relatively low ($t < 2$ minutes). As such, Design of Experiment methods which reduce the required amount of evaluation points are not utilised. Instead, a complete analysis is performed for most of the design space parameters. Two different parametric studies are performed. The first parametric study focuses on the backwards sweep parameters Λ and $d\Lambda$ over multiple operating conditions by also altering J. The second parametric study is smaller in size, only analysing Λ and κ, fixing the sweep curvature and the advance ratio to a single data point.

10.3.1. BACKWARDS SWEEP PARAMETRIC STUDY

One of the main goals of this study is to investigate the impact of backwards sweep on propeller performance. This is done by varying Λ and $d\Lambda$. It is expected that both the amount of sweep, and the distribution of this sweep are vital to the aerodynamic, structural and acoustic response of the blade. As such, a full parametric study of the Λ and $d\Lambda$ parameters is performed. 11 data points are used for each parameter, resulting in the following data points:

$$\Lambda = [0.0,\ 0.025,\ 0.050,\ 0.075,\ 0.100,\ 0.125,\ 0.150,\ 0.175,\ 0.200,\ 0.225,\ 0.250]$$

$$d\Lambda = [1.0,\ 1.7,\ 2.4,\ 3.1,\ 3.8,\ 4.5,\ 5.2,\ 5.9,\ 6.6,\ 7.3,\ 8.0]$$

In terms of the operating conditions, it has already been decided to limit the pitch setting to that of the climb conditions. Besides the pitch setting however, the advance ratio still needs to be varied from low to high-loading conditions. From initial results, it was found that $0.9 \leq J \leq 1.9$ is a suitable range of advance ratio. Significant flow separation is likely to occur at advance ratio lower than 0.9. Near $J = 1.9$, the propeller enters the windmilling state. 8 different values of J are used, such that the step size is $\Delta J = 0.143$:

$$J = [0.90,\ 1.04,\ 1.19,\ 1.33,\ 1.47,\ 1.61,\ 1.76,\ 1.90]$$

The advance ratio is a dimensionless parameter that generalises the propeller performance with regard to operating conditions. However, Sodja et al. found that the advance ratio is not a valid measure of similarity for highly flexible propellers [21]. It was found that altering the rotational speed Ω but maintaining a constant advance ratio will significantly affect the aerodynamic performance [21]. Hence, defining the advance ratio is not adequate for this parametric study, either the inflow velocity U_∞ or rotational speed Ω has to be fixed. For this parametric study, it has been chosen to fix the inflow velocity U_∞, such that the rotational speed Ω decreases as the advance ratio increases. This means the aerodynamic and inertial forces both decrease as the advance ratio increases. These loadings do not scale equally however, as can be seen in Equation (10.2).

$$\begin{aligned} \boldsymbol{q}_a &\propto V^2 = (U_\infty^2 + (r\Omega)^2) \\ \boldsymbol{q}_c &\propto \Omega^2 \end{aligned} \tag{10.2}$$

10.3.2. FORWARD-BACKWARDS SWEEP CASE STUDY

The sweep parameter κ allows forward sweep to be added between the root and tip without sweeping the entire propeller forward. The goal of this parameter is to investigate whether this kind of forward sweep can mitigate any structural deformations and reduce the impact of elasticity on the blade performance. A parametric study is performed using only κ and Λ . The sweep curvature $d\Lambda$ is fixed to $d\Lambda = 4.5$. The operating conditions are limited to $J = 1.47$. With steps of $\Delta\kappa = 0.05$, 11 total values of κ are used. Λ is limited to range from 0 to 0.20, as any higher tip sweep results in complex blade shapes that exceed the yield strength of the material.

$$\begin{aligned} &\Lambda = [0.0,\ 0.025,\ 0.050,\ 0.075,\ 0.100,\ 0.125,\ 0.150,\ 0.175,\ 0.200] \\ &\kappa = [0.0,\ 0.05,\ 0.10,\ 0.15,\ 0.20,\ 0.25,\ 0.30,\ 0.35,\ 0.40,\ 0.45,\ 0.50] \\ &d\Lambda = 4.5,\ J = 1.47 \end{aligned}$$

11

Backwards Swept Blade Results

In this chapter, the results of the sweep parametric study are discussed. The effects of the structural deformations on the aerodynamic and acoustic performance of the swept blades are first discussed in Section 11.1. Section 11.2 identifies the effects of the application of blade sweep on the rigid blades. The effects of elasticity and blade sweep are combined in Section 11.3 to compare the elastic swept blades to the straight blade. Finally, Section 11.4 shows the relation between the structural deformations and the operating settings.

11.1. Effects of Elasticity

The effects of elasticity are investigated by comparing the elastic blades directly to their rigid counterpart. The structural deformations are first analysed to provide context on the changes that will appear in aerodynamic and acoustic performance.

11.1.1. Structural Performance

The structural performance is characterised using the bending deformations, the torsional deformations of the propeller. The bending deformations are defined as the difference between the blade axis of the elastic and rigid blade in the global coordinate system. This propeller coordinate system was shown in Figure 3.4. The bending deformations are nondimensionalised using the propeller radius, and split into the x and z components. $\Delta x/R$ represents the nondimensional bending of the blade in the direction of the freestream flow. $\Delta z/R$ represents the nondimensional bending in the same direction as the applied sweep. The torsional deformations are defined as the difference in twist angle of the rigid and elastic blade; $\Delta\beta$. This $\Delta\beta$ is measured around the positive y-axis of the coordinate system, using the right-hand rule as the sign indicator. A negative $\Delta\beta$ indicates a wash-out of the blade, decreasing the local angle of attack.

Figure 11.1 shows the bending deformations at the tip of the blade for $J = 1.47$. These bending deformations are shown as a function of the two backwards sweep parameters Λ and $d\Lambda$. Figure 11.1 shows that the bending increases when the tip sweep Λ is increased. The sweep curvature only significantly affects the bending deflections at low $d\Lambda$. The local bending deflections are shown in Figure 11.2 for the propeller configurations with $0 \leq \Lambda \leq 0.25$ and $d\Lambda = 4.5$. Locally, the blades only start significantly bending past $r/R \geq 0.5$. The positive sign of Δx indicates that the blades are deforming in the same direction as the incoming freestream velocity. The negative Δz deformations mean that the blade is being straightened, reducing the sweep.
These deformations are opposite of where the aerodynamic forces are pointed. It may seem surprising that the blade is bending completely opposite of where the aerodynamic forces would be pulling the blade. But it comes from the centrifugal forces straightening the blade into $-\Delta z$ direction. This also induces a significant bending deformation in x-direction. The two bending modes are coupled because of the minor principle axis changing throughout the blade due to the twist. This bending coupling was already seen in Section 9.3, where a simple tip load in one direction also induced deformations in the other direction. The bending deformations indicate that the bending moments from the centrifugal forces are significantly higher than those of the aerodynamic forces. When the blade is straight ($\Lambda \approx 0$), the bending moments due to the aerodynamic forces are higher than those from the centrifugal forces. As such, the bending deformations of these blades are slightly in negative x and positive z direction.

Figure 11.3 shows the torsional deformations at the tip of the blade as a function of Λ and $d\Lambda$ for $J = 1.47$. This figure shows that while Λ and $d\Lambda$ clearly increase the twisting of the blade, both parameters are required to induce a significant amount of twisting. The twisting deformations are negative, corresponding to wash-out, reducing the angle of attack.

The effects of Λ and $d\Lambda$ on the local twisting distributions are shown in Figures 11.4. The blades only start significantly twisting once $r/R \geq 0.5$, similarly to the bending deformations. This characteristic is likely an attribute of the general baseline blade design. The swept blade designs by Sodja et al. [20, 21] showed significant deformations near the root, plateauing near the tip instead.

The aerodynamic forces are the main contributor to the twisting moments within the blades. For straight blades, the centre of pressure is close to the blade axis, resulting in low twisting deformations. For the case of Figure 11.3, the straight blades twist negatively around the y-axis because the centre of pressure is behind the blade axis. At high loading conditions, the centre of pressure is actually in front of the blade axis, resulting in positive twisting moments. When the blade is swept back by applying Λ and $d\Lambda$, the chordwise centre of pressure position becomes irrelevant compared to the overall position of the force in the global coordinate system. The moment arm between the centre of gravity near the root and the aerodynamic forces near the tip significantly increases due to the sweep. On the other hand, the centrifugal forces do not invoke significant twisting as the centrifugal force direction and the torsion moment axis are closely aligned.

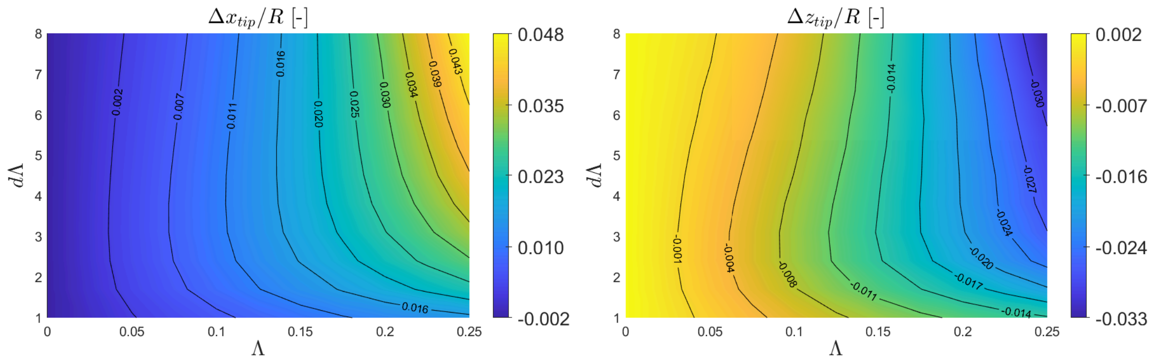

(a) Bending deformations at the tip in x-direction (b) Bending deformations at the tip in z-direction

Figure 11.1: The bending deformations at the tip of the blade as a function of the sweep parameters Λ and $d\Lambda$ for $J = 1.47$. (a) shows the bending deformations in x-direction, (b) shows the bending deformations in z-direction.

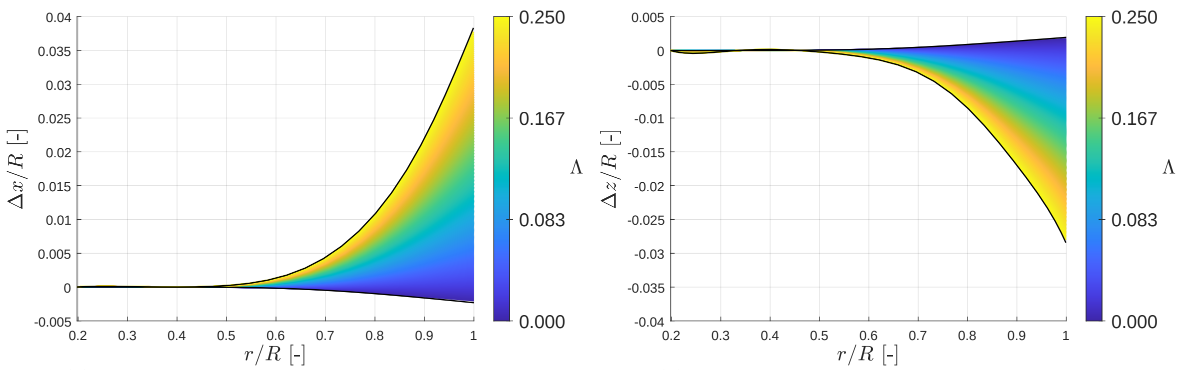

(a) Local bending deformations in x-direction (b) Local bending deformations in z-direction

Figure 11.2: The local bending deformations along the entire blade as a function of the tip sweep Λ for $J = 1.47$. $d\Lambda$ is fixed to 4.5. (a) shows the local bending deformations in x-direction, (b) shows the local bending deformations in z-direction.

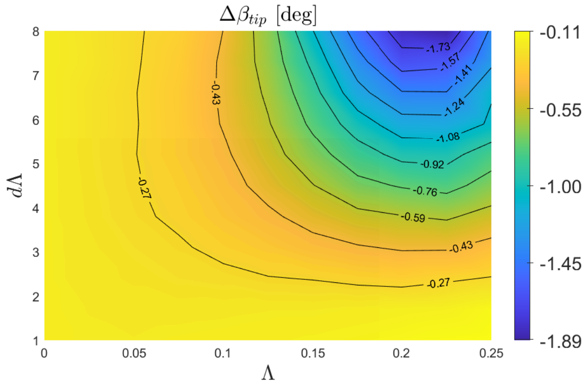

Figure 11.3: The twisting deformations at the tip of the blade as a function of the sweep parameters Λ and $d\Lambda$ for $J = 1.47$.

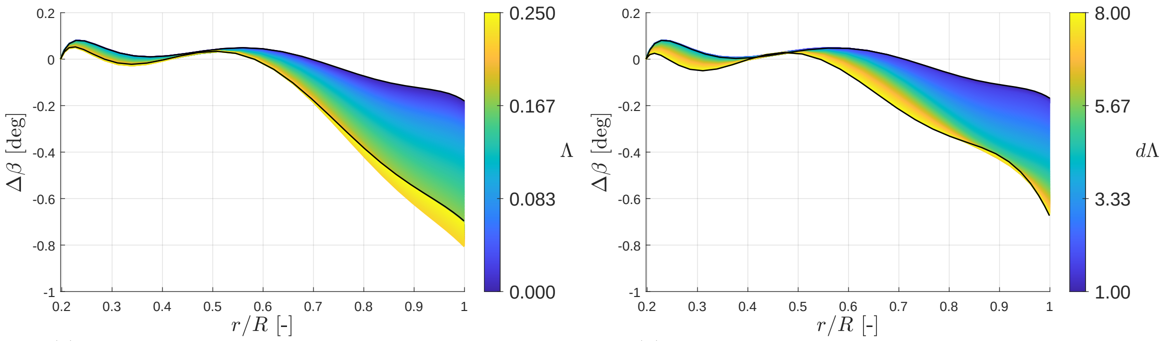

(a) Local torsional deformations as a function of Λ ($d\Lambda = 4.5$)

(b) Local torsional deformations as a function of $d\Lambda$ ($\Lambda = 0.125$)

Figure 11.4: The local twisting deformations along the entire blade as a function of (a) the tip sweep Λ and (b) the sweep curvature $d\Lambda$.

11.1.2. AERODYNAMIC PERFORMANCE CHANGES DUE TO ELASTICITY

The previous section showed that significant bending and twisting may occur when the propeller blade is swept. In this section, the aerodynamic performances of the elastic blades are compared directly to their rigid counterparts, highlighting the effects that the structural deformations have on the aerodynamic performance.

Figure 11.5 shows the percentage changes of C_T, C_P and η. Significant changes in C_T and C_P can be seen in Figures 11.5a and 11.5b. Both the thrust and required power of the propeller reduce gradually as the blade becomes more swept, due to the increasing deformations. The blades are clearly more sensitive to Λ than $d\Lambda$, similar to the total bending deformations in Figure 11.1. The penalties in performance can be as high as 20%.
The changes in aerodynamic efficiency are shown in Figure 11.5c. Despite the significant reductions in thrust and required power, the changes in aerodynamic efficiency are completely negligible. Clearly, the thrust and power coefficient change in such a way that aerodynamic efficiency remains constant. As such, while there is a penalty due to elasticity in terms of total forces generated, there is no penalty in aerodynamic efficiency.

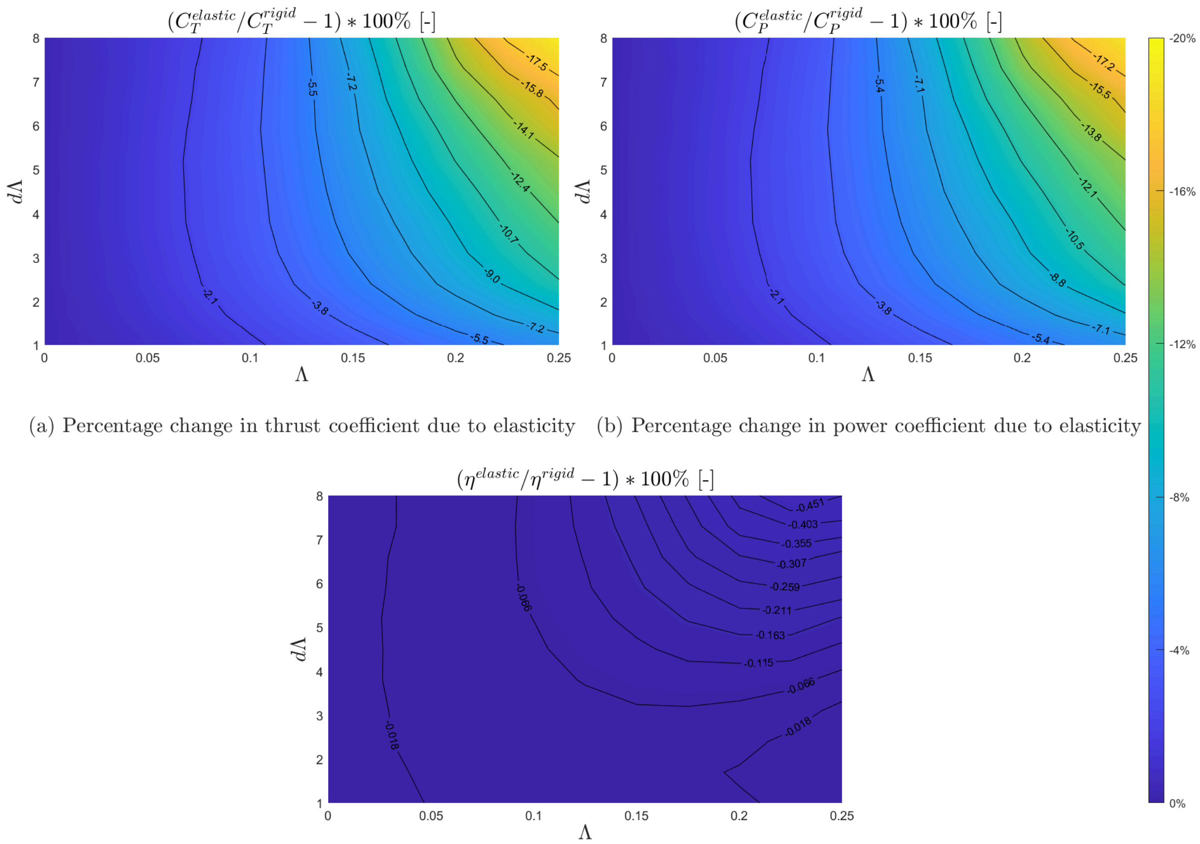

(a) Percentage change in thrust coefficient due to elasticity (b) Percentage change in power coefficient due to elasticity

(c) Percentage change in efficiency due to elasticity

Figure 11.5: The percentage change in aerodynamic performance due to elasticity as a function of the sweep parameters Λ and $d\Lambda$ for $J = 1.47$. Elastic blades are compared to their rigid counterpart. (a) shows the thrust coefficient, (b) shows the power coefficient, (c) shows the aerodynamic efficiency.

One might expect the torsional deformations to cause the biggest changes in aerodynamic performance. But the changes in C_T and C_P in Figures 11.5a and 11.5b actually resemble the contour plots of the bending deformations in Figure 11.1. This indicates that the bending deformations also significantly alter the aerodynamic performance. To analyse the effect of bending and twisting, each type of deformation is isolated and applied individually to the rigid blade. Thus, a comparison is made between the rigid blade, the blade with only the bending deformations, the blade with only twisting deformations and the fully elastic blade with bending and twisting deformations. The aerodynamic performance of each new blade is then compared to each other. The results are shown in Figure 11.6 for $J = 1.47$. It can be seen that both the bending and twisting deformations contribute to the losses in aerodynamic performance. In fact, the bending deformations result in higher losses of thrust and torque compared to the twisting deformations. The losses due to bending and twisting are combined for the fully elastic blade, which generates the least amount of aerodynamic force.

The losses in aerodynamic forces are caused by changes in the local angle of attack distribution. The local angle of attack distribution can be found using the VLM tool by calculating the total velocity near the blade leading edge using the Biot-Savart law. The differences in local angle of attack compared to the rigid blade are shown in Figure 11.7 for each of the three (semi) elastic blades. The twisted blade shows a change in local angle of attack similar to the local twist deformations, indicated with the black dashed line. The local angle of attack changes are inflated compared to these twist deformations though, with a lower angle of attack near the tip compared to the actual twist deformations. The purely bent blade experiences a more gradual change in the local angle of attack. The local angle of attack already decreases slowly near the root, continuing all the way towards the tip. The fully elastic blade, undergoing both bending and twisting, experiences the most significant reductions in local angle of attack. In fact, the angle of attack distribution of the fully elastic blade almost perfectly resembles the sum of the isolated bending and twisted blades.

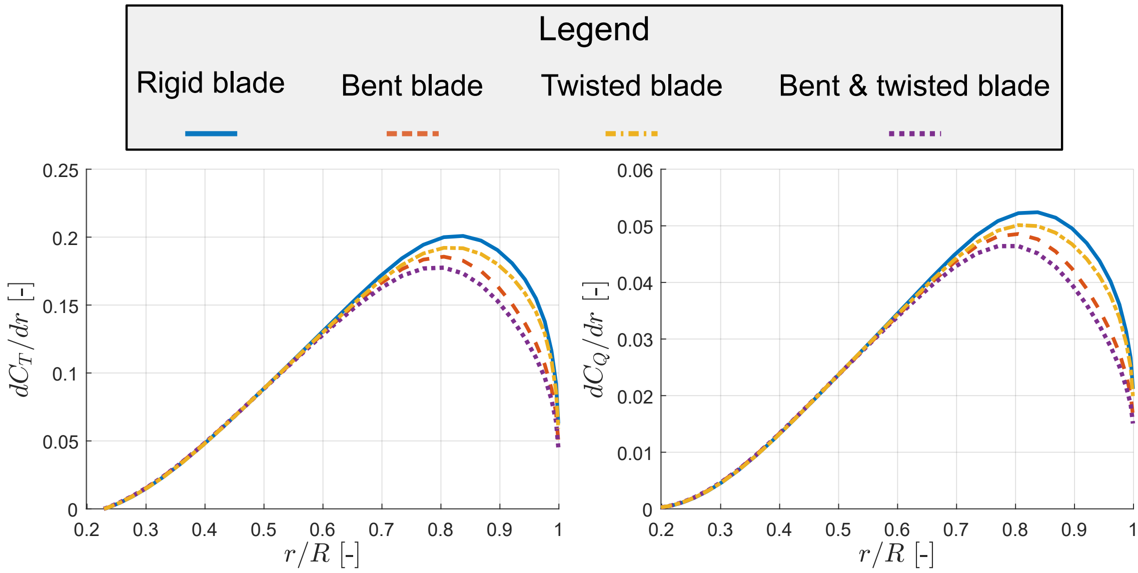

(a) Local thrust distribution

(b) Local torque Distribution

Figure 11.6: Effects of bending, twisting and bending & twisting on the local aerodynamic loading distributions for $J = 1.47$. Each type of deformations is applied individually to the rigid blade with $\Lambda = 0.25$ and $d\Lambda = 4.5$.

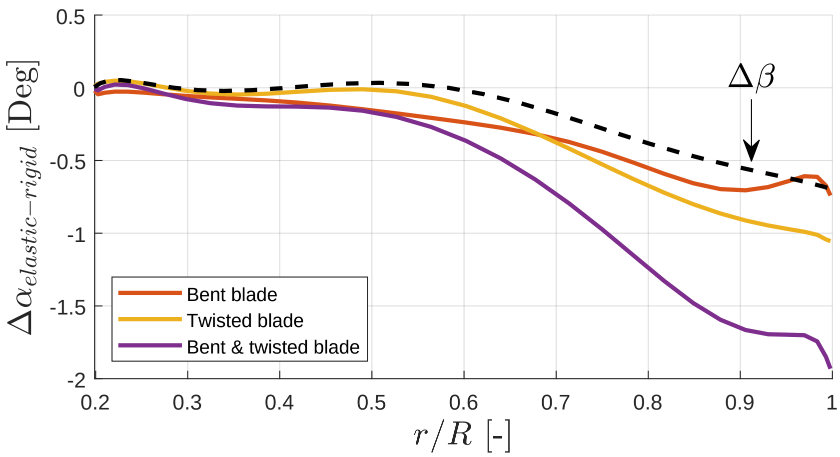

Figure 11.7: The change in local angle of attack due to bending, twisting and bending & twisting of the blade with $\Lambda = 0.25$ and $d\Lambda = 4.5$. The elastic blade is compared to the rigid blade. ($J = 1.47$)

Another critical characteristic to note from Figure 11.6 is that the changes in local aerodynamic forces are concentrated past $r/R > 0.5$, as this is also where structural deformations are most significant. With the forces near the root remaining identical, this means that the local aerodynamic loading is effectively shifting inboard. The bending deformations contribute more to this inboard shifting than the twisting deformations, as the local angle of attack already reduces closer to the root. The radial loading distribution is a critical characteristic for the acoustic performance of the propeller. As such, this characteristic is investigated further. Figure 11.8 shows the shift radial centre of pressure due to the elastic deformations of the blade. All propeller configurations experience some amount of inboard shifting of the local loading due to structural deformations near the tip. However, there is a region of propeller configurations that undergoes the largest radial shift of the loading. These are the propellers where $\Lambda \approx 0.25$ and $d\Lambda \approx 4.5$.

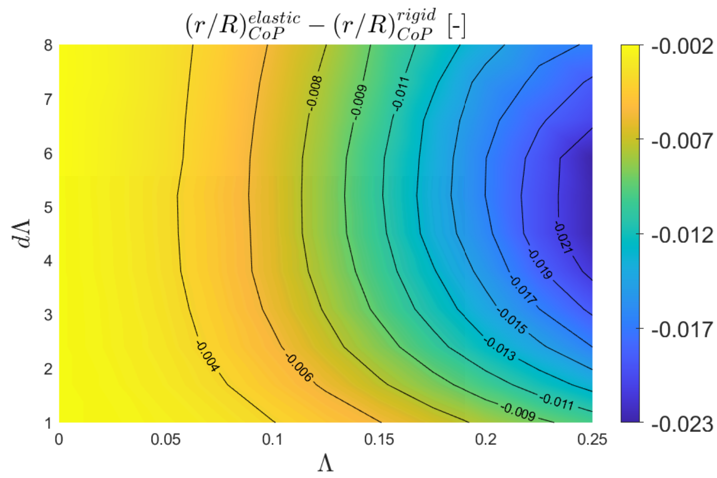

Figure 11.8: The radial shift of the radial centre of pressure due to elasticity as a function of the sweep parameters Λ and $d\Lambda$ for = 1.47. The radial position of the centre of pressure of the elastic blade is compared to the radial position of the centre of pressure of the rigid blade.

11.1.3. ACOUSTIC PERFORMANCE CHANGES DUE TO ELASTICITY

The structural deformations have so far shown significant changes in the aerodynamic performance. Specifically, the aerodynamic forces near the tip decrease as this is where the structural deformations are concentrated. Both the overall loss in performance, and the changes in the local load distributions should be reflected in the acoustic performance.

Figure 11.9 shows the changes in acoustic performance due to elasticity as a function of the two sweep parameters Λ and $d\Lambda$. The acoustic performance indicators OSPL and TSSP are a function of the directivity angle θ. In this figure, the maximum noise levels are taken, thus the directivity angle θ may differ slightly between data points. Substantial changes in overall sound pressure level due to elasticity can be seen in Figure 11.9a, with reductions in noise of up to 2.4 dB. These changes in noise levels are clearly due to the reductions in overall thrust and required power, as the contour shape is similar to those of Figure 11.5. This is as expected, as thrust and torque are one of the major noise sources.

The changes in OSPL are dominated by the changes in overall thrust and torque levels. By using the thrust-specific sound pressure level, the dependency on total thrust is removed. The effects of the blade shape and loading distributions should become more apparent. Figure 11.9b shows the difference between the elastic and rigid maximum noise levels measured in TSSP. The elastic blades still produce less noise even when accounting for the changes in total thrust. This is due to the changes in the local loading distributions. There is a clear correlation with the inboard shifting of the local loading, previously shown in Figure 11.8. The propeller configurations with the most significant inboard shifting of the loads also clearly show the highest reductions in noise levels in Figure 11.9b. This is because loads radiate less efficiently as noise if they are generated further inboard [19]. Thus, structural deformations can actually be beneficial in terms of noise levels, when accounting for the changes in overall thrust levels. This is likely dependent on how the blade actually deforms however. The swept blades of this analysis show increasing bending and twisting deformations towards the tip. The elastic blades by Sodja et al. [20, 21], replicated in Section 9.4, showed the blades quickly twisting at the root, with no further twisting near the tip. Such a twisting distribution may reduce the local forces more evenly across the entire blade. Thus the shifting of the radial centre of pressure may be diminished compared to the results of this analysis.

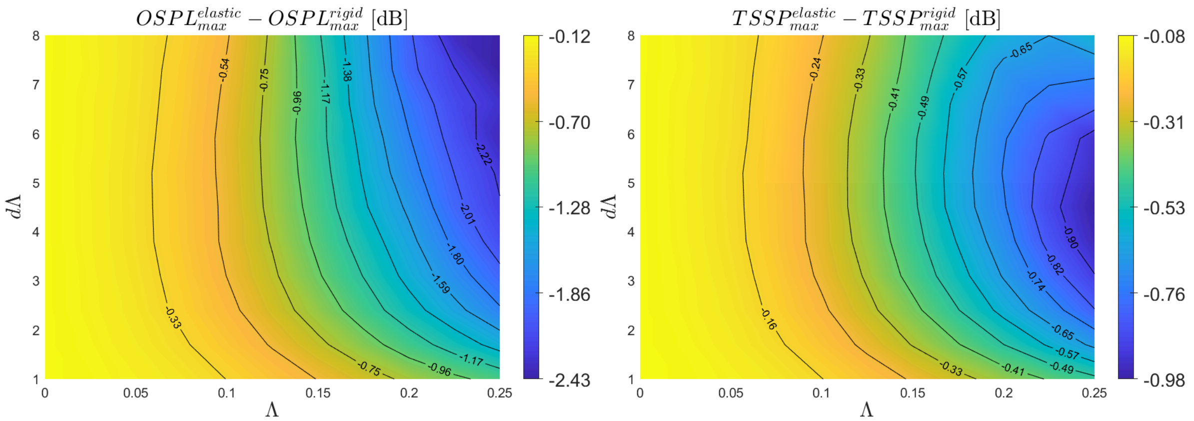

(a) Difference in Overall Sound Pressure Level due to elasticity.

(b) Difference in Thrust-Specific Sound Pressure Level due to elasticity.

Figure 11.9: The difference in noise emissions due to elasticity as a function of the sweep parameters Λ and $d\Lambda$ for $J = 1.47$. (a) shows the difference in OSPL, and (b) shows the difference in TSSP.

A clear relation between the radial load shifting and the TSSP has been identified. Besides the aerodynamic loading, other factors can also alter the acoustic performance. The change in blade shape due to structural deformations alters the MCA and FA of the blade. Since these geometric parameters are represented as phase lag effects in the acoustic method, they could also alter the noise emissions. To determine whether this effect has any significance, the aerodynamic load distributions of the rigid and elastic blades are interchanged. This means that the aerodynamic loading generated by the elastic blade geometry is applied to the rigid blade geometry (and vice versa) and input to the acoustic model. The results of this exchange of load distributions and blade shape are shown in Figure 11.10 for the swept blade with $\Lambda = 0.25$ and $d\Lambda = 4.5$.

Firstly, an observation about the prevalence of each noise source can be made. The torque noise component is by far the most dominant noise source for these propeller blades, with it being more than 15 dB louder than the thrust and thickness noise sources.
Further analysis of Figure 11.10 shows that the aerodynamic performance is the main contribution to the noise reductions. When the aerodynamic loading distribution of the elastic blade is applied to the rigid blade shape, the noise reduces almost to the level of the elastic blade with elastic loading distribution. When the rigid aerodynamic loading is applied to the elastic blade shape, the noise emissions increase. This indicates that the aerodynamic performance is the main contributor to the changes in overall noise emissions between the rigid and elastic blades. Only a minimal further reduction in noise emissions remains when the aerodynamic loadings are exchanged, this could indicate that the changes in phase lag effects due to structural deformations do have a small contribution to the change in noise emissions. But this difference is negligible compared to the effect that the aerodynamic performance has on the acoustic emissions.

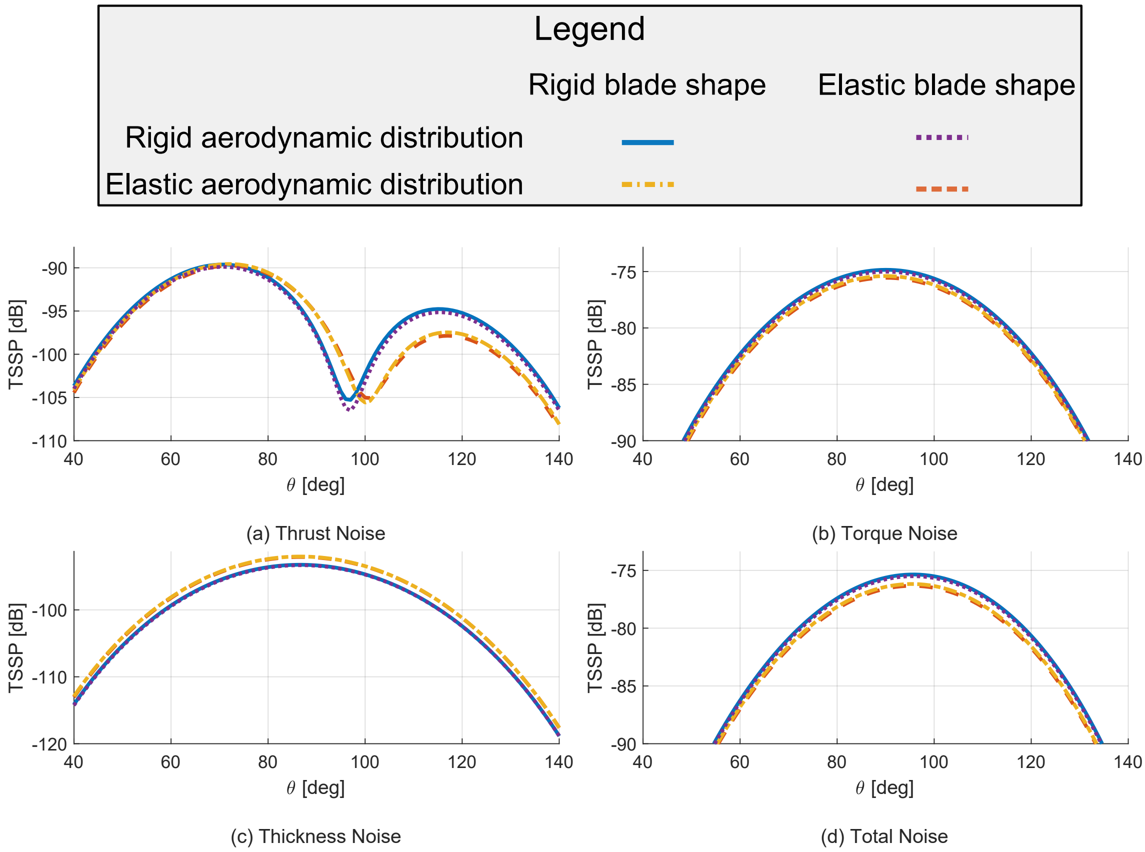

Figure 11.10: Local noise emissions for rigid and elastic propeller configurations with their aerodynamic performances exchanged, for $J = 1.47$. The aerodynamic performance of the elastic propeller is applied to the rigid propeller shape, and vice versa. (a) shows the thrust noise, (b) shows the torque noise, (c) shows the thickness noise and (d) shows the total noise.

11.2. Effects of Blade Sweep on Rigid Blades

The previous section only compared each elastic blade to its direct rigid counterpart, without considering the effects that the blade sweep has compared to a straight blade. The goal is to compare the performances of the elastic swept blades to the elastic straight blades. To be able to make this comparison, the effects that the blade sweep distributions have on the rigid aerodynamic and acoustic performances need to be investigated. In this section, the aerodynamic and acoustic performances of the rigid swept blades will be compared to the rigid straight blade, such that a full analysis of the combined effects of blade sweep and elasticity can be made in Section 11.3. The effect of blade sweep on the aerodynamic and acoustic performance has already been investigated extensively by the likes of Burger [33], De Haan [34] and Keil [35]. The method of sweep application in this study differs from these papers however. In this analysis, the sweep is applied such that the rigid blade remains within the rotational plane for one specific pitch setting. As such, the effects of blade sweep are shortly examined. The straight blades in this section refer to the propeller blade configuration with $\Lambda = 0$. Any blades with $\Lambda > 0$ and $1 \leq d\Lambda \leq 8$ are referred to as swept blades.

11.2.1. Aerodynamic performance changes due to blade sweep

The effects of the blade sweep are analysed on the rigid global aerodynamic performance by comparing the swept blades to the straight blades. Figure 11.11 shows the percentage changes in thrust coefficient, power coefficient and efficiency due to blade sweep, as a function of the tip sweep Λ and the sweep curvature $d\Lambda$ for $J = 1.47$. A complex relation exists between the two sweep parameters and the aerodynamic performance indicators. While Λ increases the aerodynamic forces generated on the blade initially, this effect diminishes as more sweep curvature $d\Lambda$ is added. Increasing the sweep curvature generally decreases the forces generated on the propeller blade. These relations result in a significant difference in performance between the swept and straight designs for the configurations with maximum sweep tip and no sweep curvature. The efficiency, shown in Figure 11.11c, increases ever so slightly when both Λ and $d\Lambda$ are increased. With a maximum of 2%

difference, this means the efficiency changes from $\eta = 0.869$ for the straight blade to $\eta = 0.888$ for the swept blade.

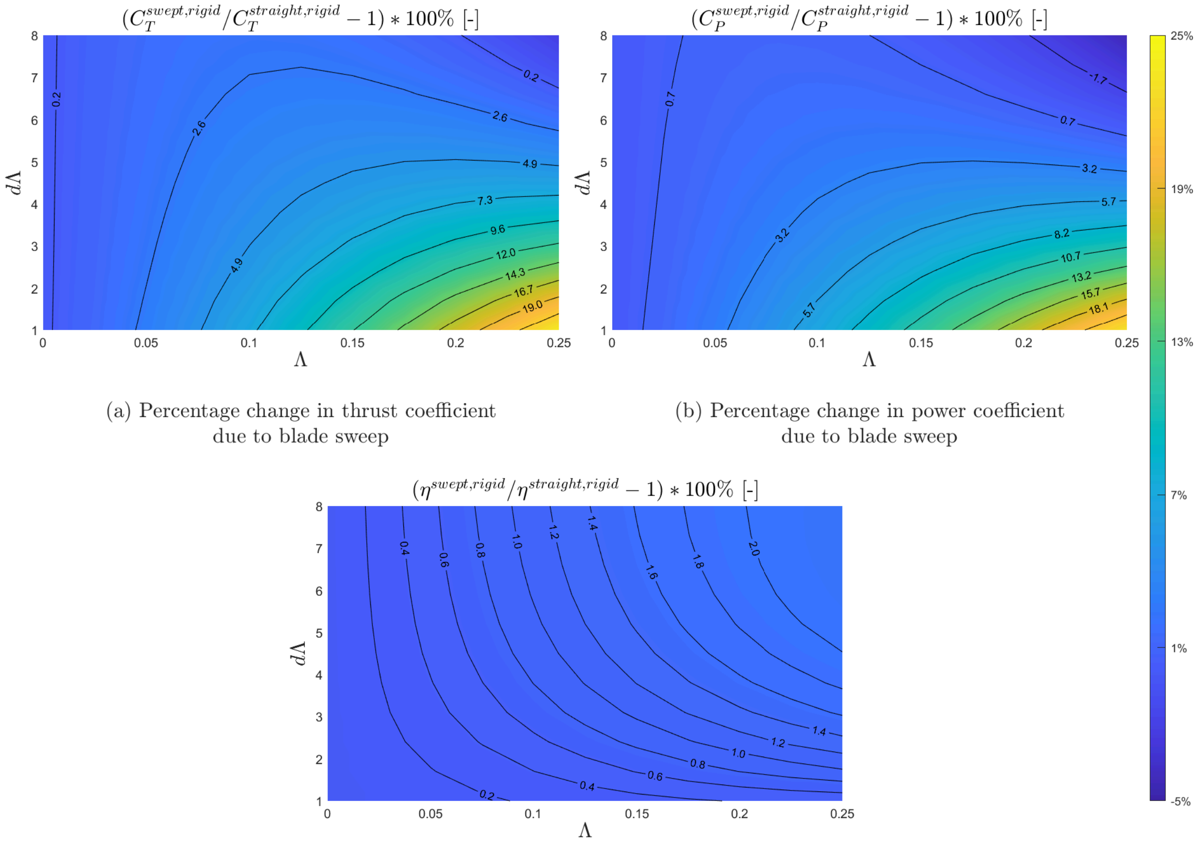

(a) Percentage change in thrust coefficient due to blade sweep

(b) Percentage change in power coefficient due to blade sweep

(c) Percentage change in efficiency due to blade sweep

Figure 11.11: The percentage change in rigid aerodynamic performance due to the application of blade sweep as a function of the sweep parameters Λ and $d\Lambda$, for $J = 1.47$. The swept blades ($\Lambda > 0$, $d\Lambda \geq 1.0$) are compared to the straight blades ($\Lambda = 0.0$). (a) shows the thrust coefficient, (b) shows the power coefficient and (c) shows the aerodynamic efficiency.

The difference between the local angle of attack distribution of the swept blades and straight blades are shown for three blade designs in Figure 11.12. The swept blade with no sweep curvature obtains higher thrust and required power due to an increased local angle of attack along the entire blade. As sweep curvature is added, the local angle of attack is reduced near the root compared to the straight blade. Towards the tip the angle of attack increases, but this effect diminishes as the sweep curvature $d\Lambda$ is increased further. For blades with sweep curvature, the angle of attack is not the only characteristic altering the aerodynamic performance though. Since these blades take a longer path to reach the same tip radius, they effectively have a higher arc length and surface area. This subsequently increases the aerodynamic forces generated, diminishing the loss of performance due to the reduction in the local angle of attack.

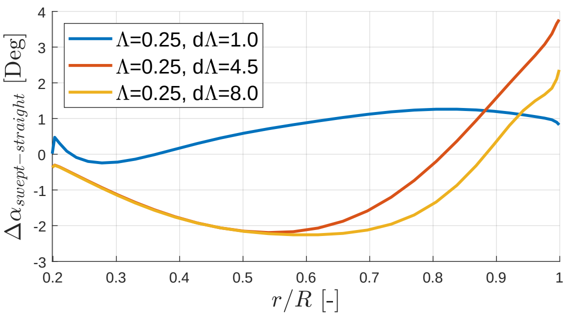

Figure 11.12: The change in local angle of attack due to the application of blade sweep for $J = 1.47$. Multiple blades with different sweep settings are compared to the straight blade.

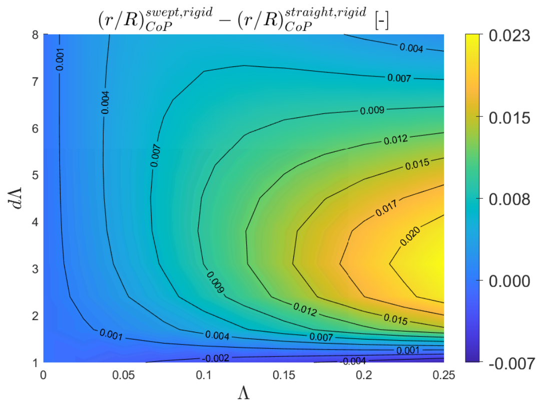

Figure 11.13: The radial shift of the radial centre of pressure due to the application of blade sweep as a function of the sweep parameters Λ and $d\Lambda$, for $J = 1.47$. The radial position of the centre of pressure of the rigid swept blade is compared to the radial position of the centre of pressure of the rigid straight blade.

Finally, the shift of the radial centre of pressure due to sweep is shown in Figure 11.13. It can be seen that the blade sweep mainly results in an outboard shift of the local loading. There is also a region of combinations which undergoes the most significant amount of outboard shift. This is the case for the blades with $\Lambda \approx= 0.25$ and $d\Lambda = 3.1$. The blade with no sweep curvature and the maximum tip sweep experiences an inboard shift of the loading, but this quickly turns into outboard shift as sweep curvature is added.

11.2.2. ACOUSTIC PERFORMANCE CHANGES DUE TO BLADE SWEEP

Significant changes in the aerodynamic loading occur when sweep is added to the base blade design. The effects of the blade sweep distribution on the acoustic performance are now investigated by comparing the results of the rigid swept blades against the rigid straight blades.

Figure 11.14 shows the difference in OSPL and TSSP due to blade sweep as a function of Λ and $d\Lambda$. The OSPL in Figure 11.14a shows a strong correlation with the overall changes in total loading of Figure 11.11. In this case, that means the overall noise levels increase. The 20% increase in thrust and required power corresponds to a 2.5 dB increase in maximum noise. The swept blades with $d\Lambda = 1$ show a slight decreasing trend in overall noise compared to the other swept blade designs. This could be due to the slight inboard shifting of the loading for these configurations, as seen in Figure 11.13.

The noise levels expressed in TSSP are shown in Figure 11.14b. No noise reductions due to sound wave interference caused by blade sweep can be identified. This effect is generally most effective at high Mach numbers, however. Instead, the TSSP again shows a strong correlation with the radial shifting of the local loading. The noise levels actually increase due to this outboard shifting of the loading.

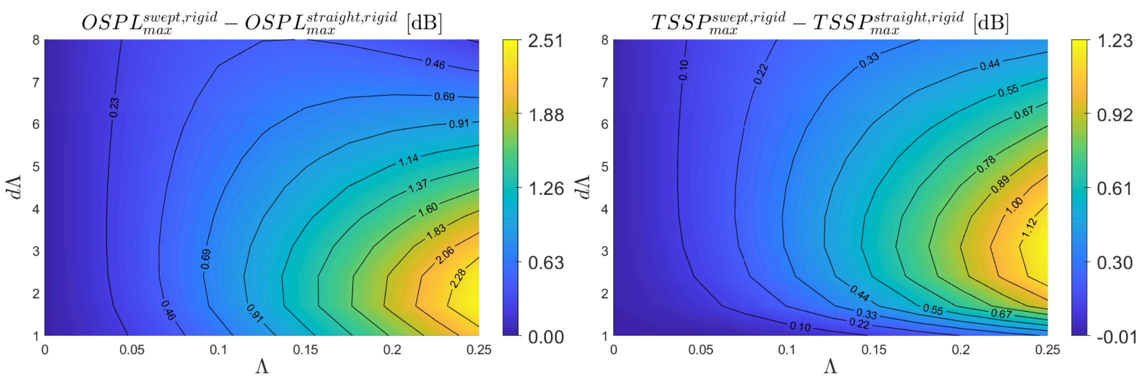

(a) Difference in Overall Sound Pressure Level due to blade sweep.

(b) Difference in Thrust-Specific Sound Pressure Level due to blade sweep

Figure 11.14: The change in noise emissions due to the application of blade sweep as a function of the sweep parameters Λ and $d\Lambda$, for $J = 1.47$. (a) shows the difference in OSPL and (b) shows the difference in TSSP.

11.3. EFFECTS OF ELASTICITY & BLADE SWEEP

The effects of elasticity and blade sweep have now been identified independently in the previous sections. A full comparison can now be made between the elastic swept blades and the elastic straight blades. This comparison will show how the swept blades perform compared to a standard straight blade design, accounting for all the effects that elasticity and blade sweep has. The performance of the elastic straight blade is used instead of the rigid performance since the effects of elasticity are negligible on the straight blade anyway.

11.3.1. AERODYNAMIC PERFORMANCE CHANGES DUE TO ELASTICITY & BLADE SWEEP

Both the blade sweep and elasticity have been shown to significantly alter the aerodynamic performance so far. The elasticity results in significant losses of performance for swept blades, with the local loading shifting inboard. On the contrary, adding blade sweep has increased the performance in some cases, shifting the aerodynamic loading outboard. The comparison between elastic swept blades and elastic straight blades will show how these effects weigh up against each other. Figure 11.15 shows the percentage change of the aerodynamic performance. It can be seen that the extremes of each of the analyses in Sections 11.1 and 11.2 are still apparent. The blade designs with high tip sweep and no sweep curvature still experience significant increases and thrust and required power, partly due to the relatively small structural deformations. The fully swept blade, with maximum Λ and $d\Lambda$, still shows the extreme loss in performance due to the structural deformations, and minimal performance gains due to the effects of sweep. There are also some configurations in which the effects of elasticity and blade sweep cancel each other out, such that the performance remains similar to that of a straight blade design. This is the case for the blades with $d\Lambda \approx 3.1$. In terms of aerodynamic efficiency, the elasticity has minimal impact on this metric, unlike the effects of blade sweep. Therefore, the change in aerodynamic efficiency, in Figure 11.15c, shows similar behaviour to that of the blade sweep.

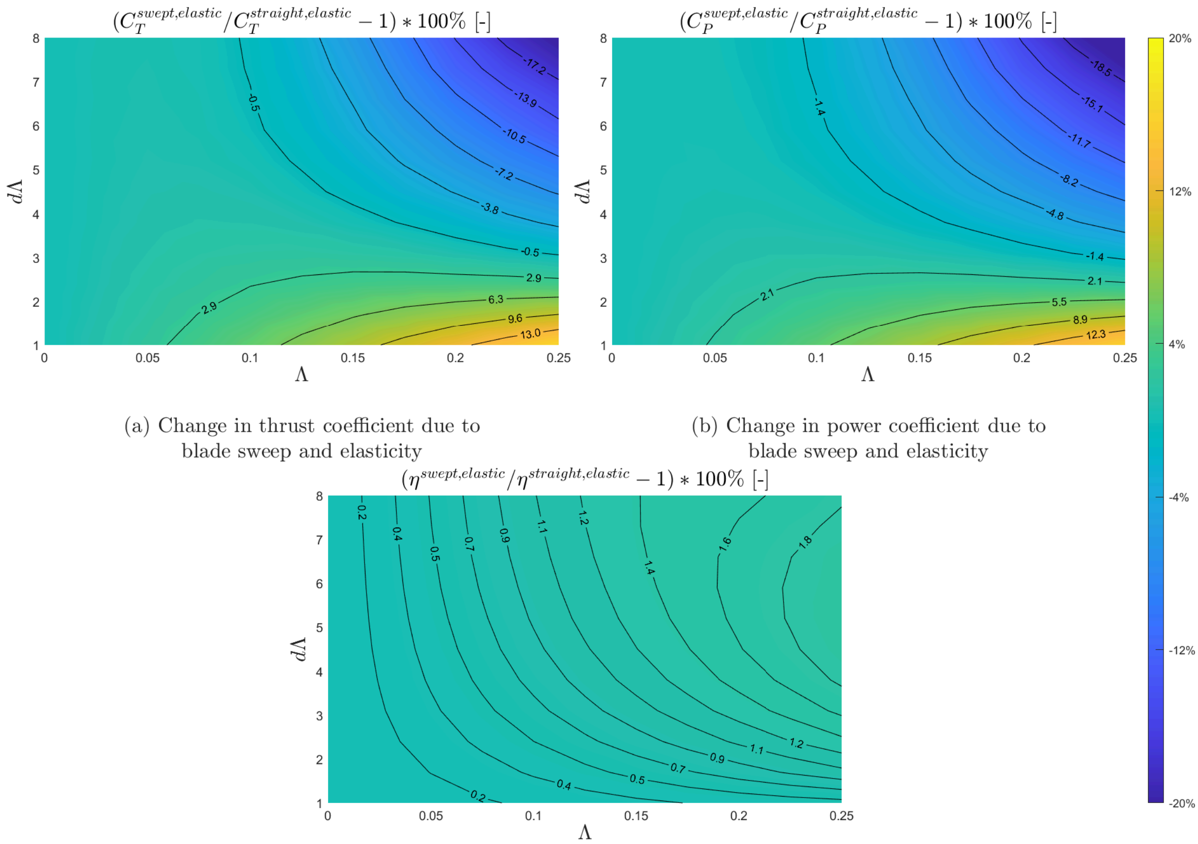

(a) Change in thrust coefficient due to blade sweep and elasticity

(b) Change in power coefficient due to blade sweep and elasticity

(c) Change in efficiency due to blade sweep and elasticity

Figure 11.15: The percentage change in aerodynamic performance due to the combined effects of elasticity and blade sweep, as a function of the sweep parameters Λ and $d\Lambda$, for $J = 1.47$. The elastic swept blades are compared to the elastic straight blade. (a) shows the thrust coefficient, (b) shows the power coefficient and (c) shows the aerodynamic efficiency.

The previously shown changes of local angle of attack distributions for the $\Lambda = 0.25$ and $d\Lambda = 4.5$ blade are shown again in Figure 11.16. The total change in local angle of attack is now also depicted. This distribution perfectly resembles the sum of the two individual angle distributions. Therefore, it seems that the effects of elasticity and blade sweep on the aerodynamic performance are completely independent of each other and can be superimposed.

The effects of elasticity and blade sweep resulted in completely opposing behaviours in terms of the radial shifting of the local aerodynamic forces. Due to the structural deformations being concentrated only near the tip, the aerodynamic loading effectively moved inboard. The blade sweep had the effect of shifting the loading outboard. The net effect of both elasticity and blade sweep on the radial centre of pressure of the torque is now shown in Figure 11.17. It can be seen that the shifting of the aerodynamic loading has been almost completely nullified due to the opposing effects of the elasticity and blade sweep. The outboard shifting has become almost negligible, with the inboard shifting only being prevalent near the extremes of $d\Lambda$ with maximum Λ .

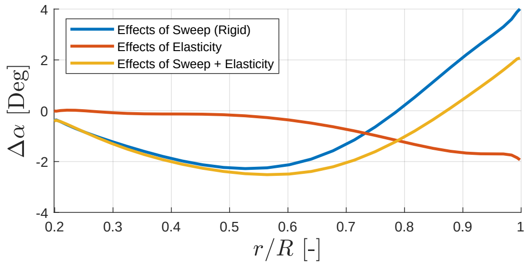

Figure 11.16: The change in local angle of attack due to the effects of elasticity, blade sweep and the combination. The angle of attack distributions of the swept blade ($\Lambda = 0.25$, $d\Lambda = 4.5$) are compared to the angle of attack distribution of the rigid straight blade.

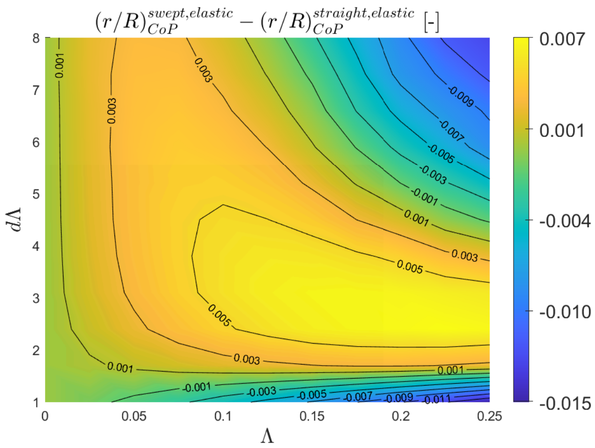

Figure 11.17: The radial shift of the radial centre of pressure due to the effects of elasticity and blade sweep as a function of the sweep parameters Λ and $d\Lambda$, for $J = 1.47$. The elastic swept blades is compared to the elastic straight blade.

11.3.2. ACOUSTIC PERFORMANCE CHANGES DUE TO ELASTICITY & BLADE SWEEP

Changes in the acoustic performance have been predominantly caused by changes in the aerodynamic performance. With both the total forces decreasing, and the radial loading shifting inboard, the elasticity effects have shown to be beneficial in terms of noise levels. On the other hand, the blade sweep has caused increases and outboard shifting of the loads, increasing the noise levels. Combining these two effects may nullify any losses or gains in acoustic performance.

Figure 11.15 shows the difference in noise levels between the elastic swept blades and the elastic straight blades. Again, when defining the noise in terms of overall sound pressure level, the changes in noise levels correlate strongly to the aerodynamic changes. Thus, the fully swept blade with no sweep curvature produces 1.26 dB louder sound waves. The fully swept and curved blade is 2.11 dB less loud due to the 20% loss in thrust and torque.
With the normalised sound levels in Figure 11.18b, the spread of sound level changes has vastly diminished. While the changes in TSSP still resemble the overall shape of the contour in Figure 11.17, the colour gradients have become less similar. Still, there are some blade configurations which are louder and some that are quieter compared to the straight blade. The configurations with maximum tip sweep and $d\Lambda \approx 3.1$ are still almost 0.5 dB louder, with this sound level increase having been reduced from 1.2 dB due to elasticity. The quietest propeller configurations are those with maximum tip sweep and sweep curvature. These blades were originally 0.65 dB quieter compared to their rigid versions, but the effects of blade sweep have decreased the noise reduction to 0.2 dB compared to the straight blade.

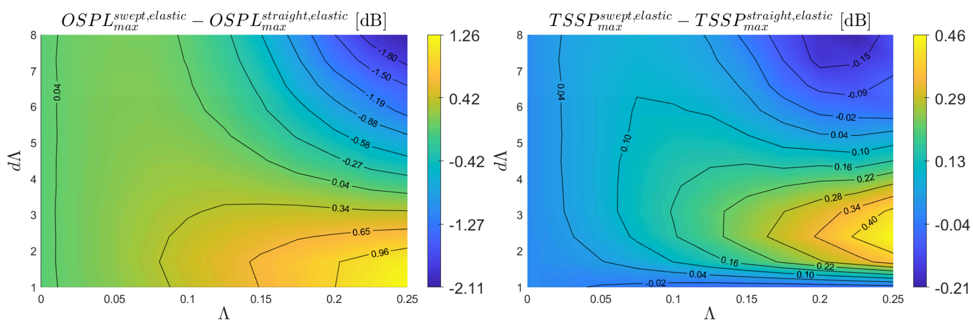

(a) Difference in Overall Sound Pressure Level due to blade sweep and elasticity

(b) Difference in Thrust-Specific Sound Pressure Level due to blade sweep and elasticity

Figure 11.18: The difference in noise emissions due to the effects of elasticity and blade sweep, as a function of the sweep parameters Λ and $d\Lambda$, for $J = 1.47$. The elastic swept blades are compared to the elastic straight blade. (a) shows the OSPL and (b) shows the TSSP

11.4. EFFECTS OF OPERATING CONDITIONS

The analyses of the previous sections have only focused on a singular operating condition so far, namely the setting with the advance ratio J set to 1.47. In this section, the effects of the operating conditions are analysed by changing the advance ratio from 0.90 to 1.90. To limit the amount of data that needs to be shown, this analysis is done only for the straight blade and a singular swept blade with $\Lambda = 0.25$ and $d\Lambda = 4.5$.

11.4.1. STRUCTURAL PERFORMANCE CHANGES DUE TO OPERATING SETTINGS

The bending and twisting deformations for the straight and swept blade are shown in Figure 11.19. Section 11.1.1 showed that the bending deformations are determined by the centrifugal forces for swept blades. This can also be seen in Figure 11.19a, with the bending deformations $\Delta x/R$ and $\Delta z/R$ reducing with increasing advance ratio, as the rotational speed decreases to increase the advance ratio. On the other hand, the straight blade shows bending of the opposite sign compared to the swept blade. This is because the aerodynamic forces are the main contribution of bending for straight blades. The centrifugal forces do not generate a significant bending moment due to the lack of sweep. These bending deformations are highest at high loading but still negligible compared to the bending of a swept blade.
The torsional deformations in Figure 11.19b show that the twisting deformations also increase when the loading is increased. This is due to the increasing aerodynamic forces however, as the twisting deformations are purely a function of the aerodynamic loading. The wash-out of the swept blade increases as the loading increases. For the straight blade, the sign of the twisting deformations changes as the loading increases. The twisting of the straight blade depends on the position of the local centre of pressure relative to the local centre of gravity.

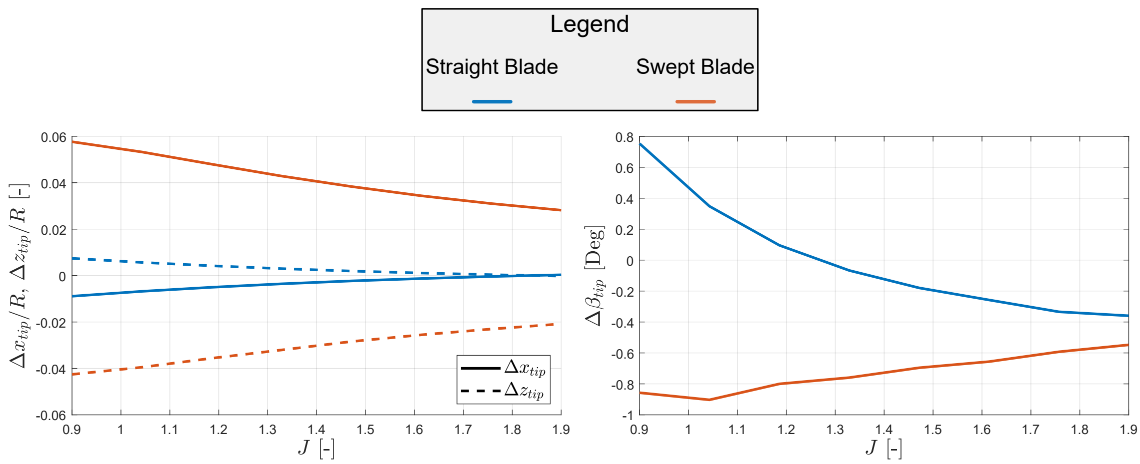

(a) Bending deformations at the tip

(b) Twisting deformations at the tip

Figure 11.19: The structural deformations at the tip of a straight and swept blade, as a function of the advance ratio. The swept blade has $\Lambda = 0.25$ and $d\Lambda = 4.5$. (a) shows the bending deformations in x- and z-direction, (b) shows the twisting deformations.

11.4.2. AERODYNAMIC PERFORMANCE CHANGES DUE TO OPERATING SETTINGS

The three aerodynamic performance indicators, together with the radial centre of pressure position, are shown as a function of the advance ratio for the straight and swept blade in Figure 11.20. Firstly, it can be noted that the difference between the aerodynamic performance of the elastic and rigid straight blade is negligible. Clearly the structural deformations are not significant enough in any operating condition to result in any significant changes in the aerodynamic performance. This is not the case for the swept propeller. A substantial change in performance occurs between the elastic and rigid swept blade. This difference in performance grows as the advance ratio decreases due to the increasing structural deformations. In terms of efficiency, there is no substantial effect in Figure 11.20c.
By comparing the performance of the rigid straight blade and swept blade, it can be seen that the effects of blade sweep are a function of the advance ratio. At low loading conditions the blade sweep increases both the thrust and required power. As the loading increases this benefit diminishes such that the thrust and required power are reduced. Adding the effects of elasticity on top of this, the difference between the straight and swept blade becomes significant. Since the required power is reduced more than the thrust, the efficiency

actually increases.

Finally, the shift of the radial centre of pressure of the torque is shown in Figure 11.20d. Section 11.2.1 showed that adding blade sweep shifted the loading outboard for $J = 1.47$. Figure 11.20d shows that this radial load shifting is actually a function of the advance ratio. At high loading, adding sweep actually moves the loading slightly inboard. This is combined with the structural deformations near the tip effectively moving the loading inboard as well. The result is the elastic swept blades having their loading shifted considerably inboard compared to the straight blade at high loading conditions. With how important the radial centre of pressure has been on the thrust-specific sound pressure levels, this will be reflected in the acoustic performance.

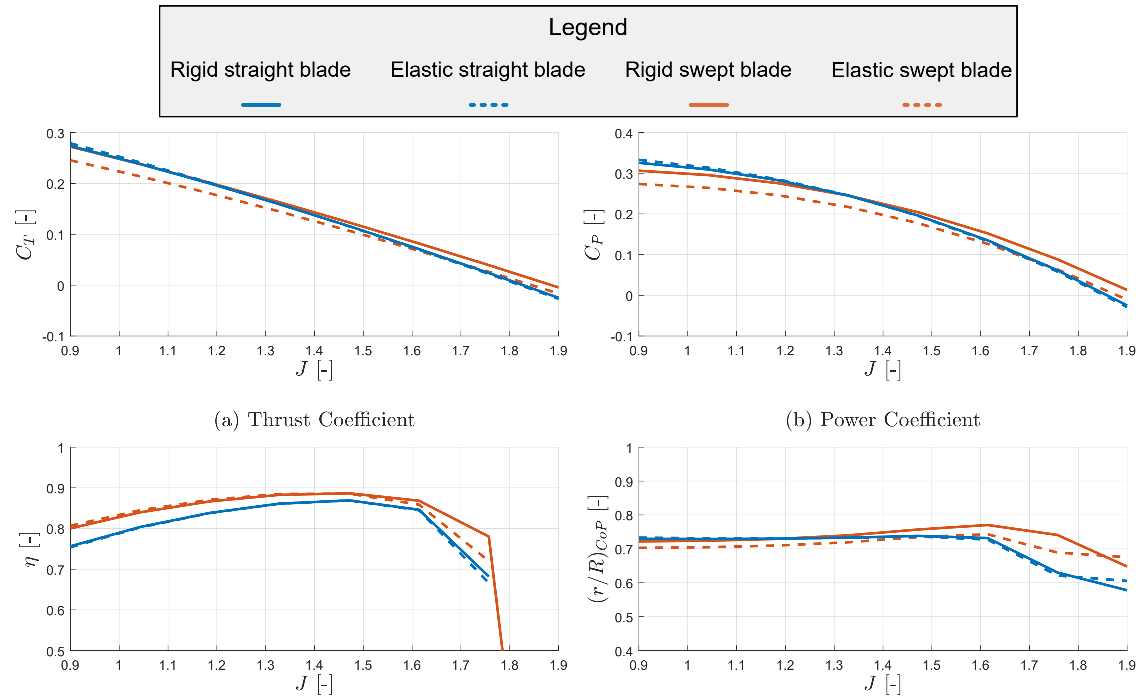

(a) Thrust Coefficient

(b) Power Coefficient

(c) Aerodynamic Efficiency

(d) Radial Centre of Pressure Position

Figure 11.20: The aerodynamic performance of the rigid straight blade, elastic straight blade, rigid swept blade and elastic swept blade as a function of the advance ratio. The swept blade has $\Lambda = 0.25$ and $d\Lambda = 4.5$. (a) shows the thrust coefficient, (b) shows the power coefficient, (c) shows the aerodynamic efficiency and (d) shows the radial position of the centre of pressure.

11.4.3. ACOUSTIC PERFORMANCE CHANGES DUE TO OPERATING SETTINGS

The total noise emissions as a function of the advance ratio, expressed in OSPL and TSSP, are shown in Figure 11.21. Since the changes in noise emissions are small compared to the total noise levels, the differences in noise emissions compared to the rigid straight blade are also plotted in Figure 11.21c and d. Though these changes may seem insignificant against the total noise emissions, they still produce noticeable changes due to the logarithmic scale.

In terms of OSPL, the effect of the advance ratio behaves similarly to aerodynamic performance. As the loading increases, the increasing structural deformations reduce the thrust and required power, decreasing the overall noise levels. At high loading, the elasticity alone almost reduces the noise by 2 dB. Such a significant change in noise levels can not be neglected, proving that elastic deformations are required for the accurate prediction of noise levels of swept blades.
Even when normalising for the changes in thrust using the TSSP in Figures 11.21b and 11.21d, noise reductions of up to 1 dB can be observed due to radial shifting of the local loading. Note that the advance ratio range for the TSSP plots are limited, due to the thrust reaching zero and the TSSP approaching negative infinity. With the trend of outboard load shifting changing to inboard shifting in Figure 11.20d, $\Delta TSSP_{max}$ also changes from increasing to decreasing compared to the straight blade.

It is difficult to identify any effects of noise reductions due to sound wave interference. This sound wave interference is most effective at higher local velocities, which corresponds to the lower advance ratios. While the noise levels do reduce for this flow region, it is most likely due to the extra losses in thrust and required power, and the inboard shifting of the loads.

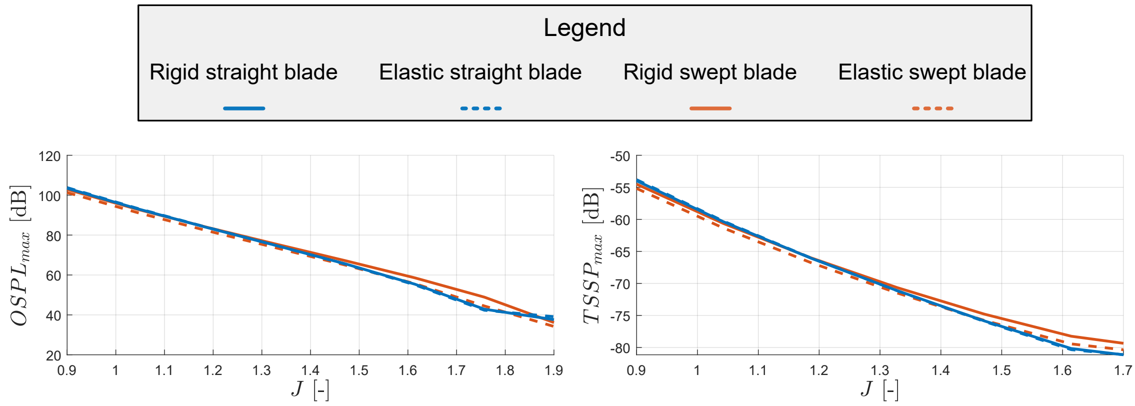

(a) Maximum Overall Sound Pressure Levels (b) Maximum Thrust-Specific-Sound Pressure Levels

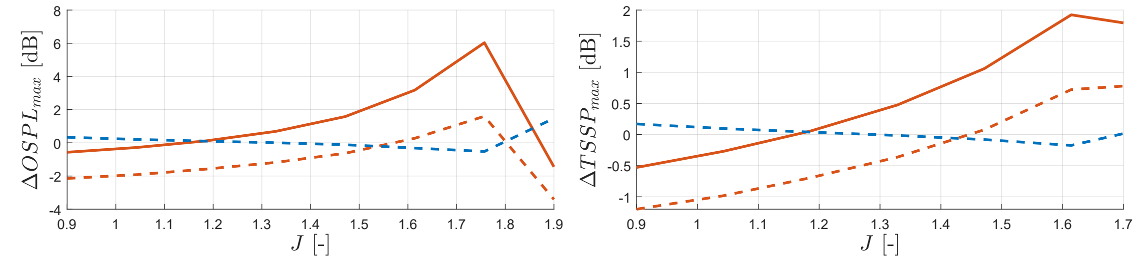

(c) Difference in maximum OSPL compared to the rigid straight blade

(d) Difference in maximum TSSP compared to the rigid straight blade

Figure 11.21: The acoustic performance of the rigid straight blade, elastic straight blade, rigid swept blade and elastic swept blade as a function of the advance ratio. The swept blade has $\Lambda = 0.25$ and $d\Lambda = 4.5$. (a) shows the OSPL and (b) shows the TSSP. The differences in noise emissions compared to the rigid straight blade are shown in (c) for OSPL and (d) for TSSP.

12

Forward-Backward Swept Blade Results

It has been shown that structural deformations result in significant changes in the aerodynamic and acoustic performance. These changes due to elasticity increase as the total sweep is increased. The results of the forward-backwards swept blades are now analysed to determine whether these complex sweep distributions can reduce the structural deformations, and hence, the loss in performance due to elasticity. As was explained in Section 10.3.2, forward sweep parameter κ and the tip sweep parameter Λ are varied, with the sweep curvature being fixed at $d\Lambda = 4.5$. Only the operating condition of $J = 1.47$ is analysed.

12.1. Structural Performance of Forward-Backwards Swept Blades

The structural performance of the forward-backward swept blades should show whether the total deformations reduce in any way by adding some forward sweep between the root and tip of the blade. The global bending deflections are first shown in Figure 12.1. It can be seen that κ does not provide any benefits in terms of reducing the total bending deformations. Instead, the bending deformations actually increase when forward sweep is added between the root and tip.

The torsional deformations at the tip, as a function of κ and Λ are shown in Figure 12.2. This figure shows that adding forward sweep between the root and the tip can decrease the torsional deformations. However, this does not occur by simply increasing κ. Both a significant amount of forward sweep, and backwards tip sweep is required, as initially both parameters increase the torsional deformations. The dashed red line in Figure 12.2 indicates the boundary, after which increasing both parameters will start to decrease the twisting of the blade. This is unlike what one might expect, especially concerning the fact that adding more backwards tip sweep can reduce the twisting. A closer investigation of the local internal moments during the iterative aerodynamics-structures calculations has revealed that it is actually the combination of the centrifugal forces with the bending deformations, which is the leading cause of this phenomenon. The local twisting deformations as a function of κ are shown in Figure 12.3. This shows in detail how the torsional deformations initially get worse from $0 \leq \kappa \leq 0.25$. Increasing κ further decreases by how much the blade twists.
Originally the centrifugal forces do not generate a significant twisting moment, as the blade axis remains within the rotational plane. As the blade bends, a new moment arm appears on which the centrifugal forces act. This effect has been negligible so far for the purely backwards swept blades, but these forward-backwards blade designs are bending up to 50% more than the backwards swept designs. These new twisting moments due to the centrifugal forces are causing positive torsional deformations, increasing the angle of attack. Any forward sweep at the radial centre of the blade does not meaningfully relieve the washout generated by the aerodynamic forces. No twisting deformations occur near this region of the blade anyway. In fact, the twisting deformations originally get worse when κ increases, as the moment arm between the blade axis and the centres of pressure increases between the middle and tip of the blade.

With maximum κ and Λ , the twisting deformations at the tip almost reach $+2^{\circ}$. It may be possible to generate such twisting deformations by implementing dihedral to the blade shape, this is outside the scope of this research however. Furthermore, positive twisting deformations may not be beneficial, as they could bring more complex aeroelastic effects with them. Though such phenomena are not analysed in this research due to the simplicity of the aerodynamic and structural models.

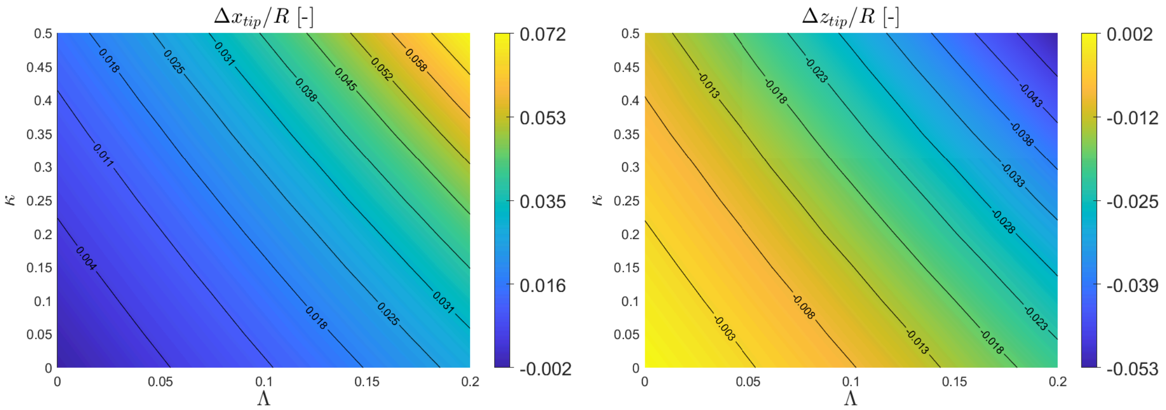

(a) Bending deformations at the tip in x-direction (b) Bending deformations at the tip in z-direction

Figure 12.1: The bending deformations at the tip of the blade as a function of the sweep parameters Λ and κ for $J = 1.47$. (a) shows the bending deformations in x-direction, (b) shows the bending deformations in z-direction.

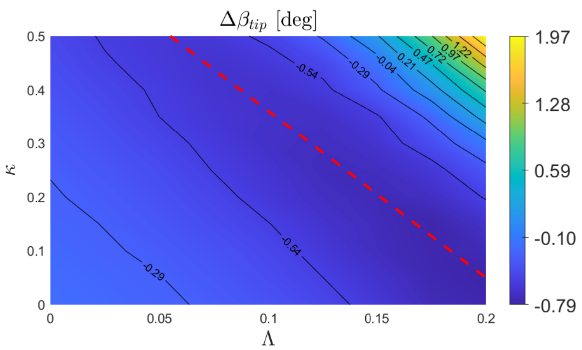

Figure 12.2: The twisting deformations at the tip of the blade as a function of the sweep parameters Λ and κ for $J = 1.47$. The dotted red line indicates a front of minimum torsional deformations.

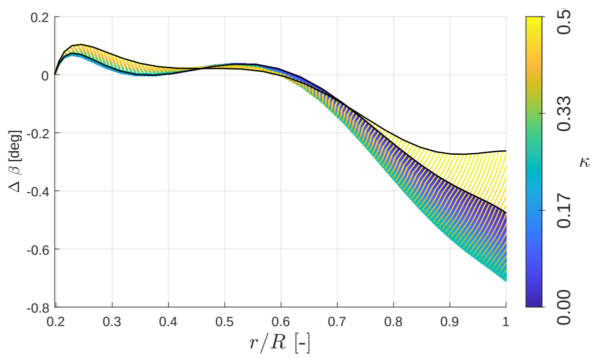

Figure 12.3: The local twisting deformations along the entire blade as a function of κ for $J = 1.47$ ($\Lambda = 0.125$). The blade twist initially increases, decreasing again after $\kappa \geq 0.25$.

12.2. AERODYNAMIC PERFORMANCE OF FORWARD-BACKWARDS SWEPT BLADES

The previous section showed that forward sweep between the root and tip is able to reduce the torsional deformations. The aerodynamic analysis in Section 11.1.2 showed that both the bending and torsional deformations contribute to changes in aerodynamic performance. As such, it is not guaranteed that these reductions in torsional deformations will be reflected in the aerodynamic performance of the elastic forward-backwards swept blades, especially with the significant increase in bending deformations.

Figure 12.4 shows the percentage change in aerodynamic performance due to structural deformations of the forward-backwards swept propeller blades. It can be seen that the forward-backward sweep does recover some of the performance lost due to elasticity. Similar to the torsional deformations, the increase of κ will initially increase the performance loss due to elasticity; by adding even more forward sweep, this performance loss can be recovered. For some blades, a significant amount of the performance loss due to elasticity can be recovered by increasing κ. For example, the swept blade with $\Lambda = 0.20$ and $\kappa = 0.0$ loses approximately 10% of its performance due to elasticity. This loss in performance reduces to only 1% when κ is set to 0.50. Remember however that Figure 12.4 compares the elastic blade performance to their direct rigid counterpart. As such, any performance loss due to the application of this type of blade sweep is not visible. The effects of the blade sweep on the rigid performance can be significant, as was shown in Section 11.2.
In terms of efficiency, shown in Figure 12.4c, there are no significant changes. The trend of the elasticity not

significantly altering the propeller efficiency has been the case for all blade configurations so far. As such, while there is a loss in thrust and required power, the aerodynamic efficiency is unaffected.

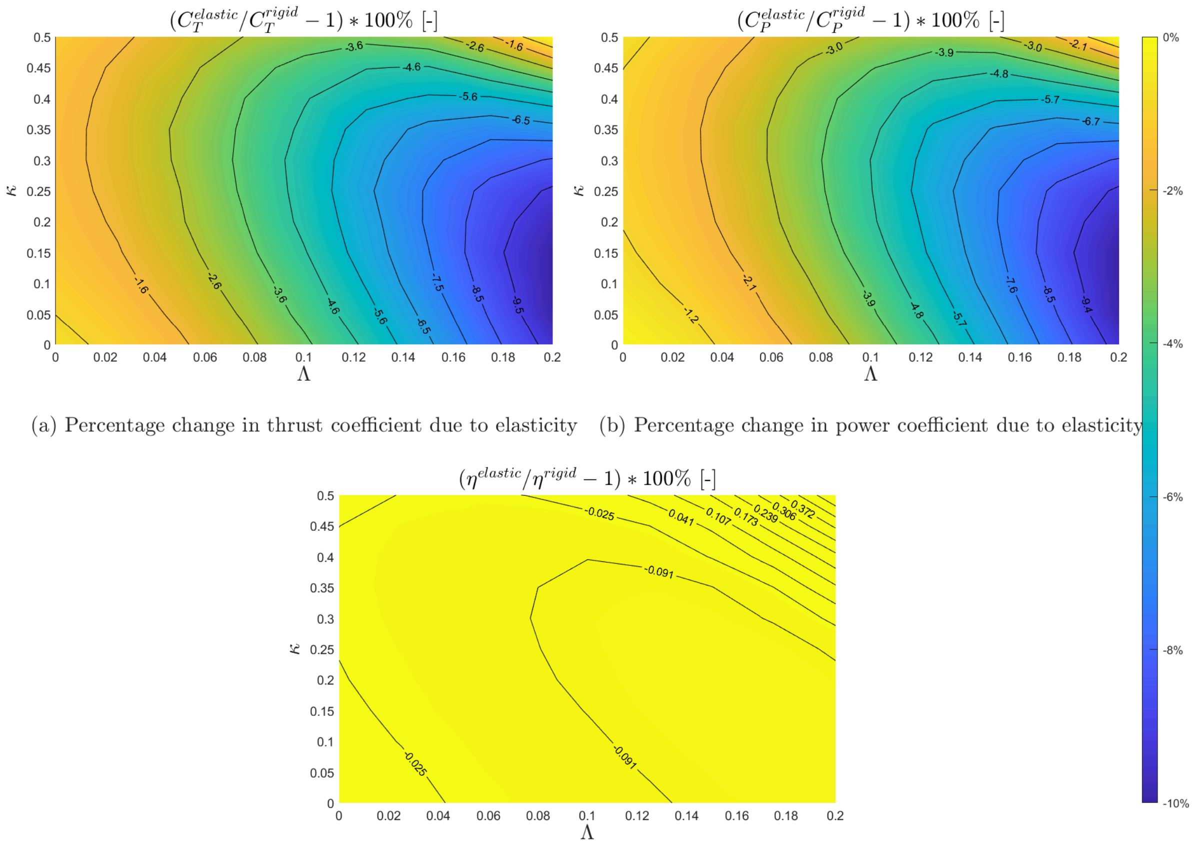

(a) Percentage change in thrust coefficient due to elasticity (b) Percentage change in power coefficient due to elasticity

(c) Percentage hange in efficiency due to elasticity

Figure 12.4: The percentage change in aerodynamic performance due to elasticity as a function of the sweep parameters Λ and κ for $J = 1.47$. Elastic blades are compared to their rigid counterpart. (a) shows the thrust coefficient, (b) shows the power coefficient, (c) shows the aerodynamic efficiency.

Figure 12.5 shows multiple local thrust and torque distributions of both rigid and elastic forward-backward swept blades. The sweep tip Λ is fixed to 0.150, with κ ranging from 0 to 0.50. With this figure, the effects of elasticity and blade sweep can be identified. First of all, the change in sweep distribution significantly reduces the thrust and torque generated. From $\kappa = 0.0$ to $\kappa = 0.50$, the total thrust and torque have both reduced by approximately 17%. Another thing to notice is how the overall shape changes as the sweep distribution becomes more curved. The local loading flattens out and becomes less peaky. The shape of the local distribution is important for the noise emissions, as less peaky distributions may generate less noise [19].
The elasticity initially reduces the loading, when $\kappa = 0$ and $\kappa = 0.25$. When κ increases further, the peak loading increases and shifts significantly inboard. While the inboard shifting will reduce the noise emissions, the increasing local peak may have an adverse effect. The overall elastic loading still remains below that of the rigid loading, but the loss in loading significantly diminishes due to the positive twisting. The effect of blade sweep on the rigid blade is significantly larger than the effect of elasticity though. As such, including a forward-backwards sweep to diminish the effect of elasticity is not worthwhile unless adjustments of other propeller geometries are incorporated to match the thrust of the original propeller.

The shifting of the radial centre of pressure due to the elastic effects is quantified in Figure 12.6a. The elastic effects shift the loading inboard for all configurations. The amount of shifting is similar to that of the purely backwards swept blades. Figure 12.6b shows the difference in the local peak loading. The local loading distributions are normalised such that the total surface adds up to unity. As such, negative values in Figure 12.6b means that the loading distribution is less peaky, and positive values mean the peak is increased. It can be seen that blades that experience positive twisting deformations also produce significantly higher peaks in local loading.

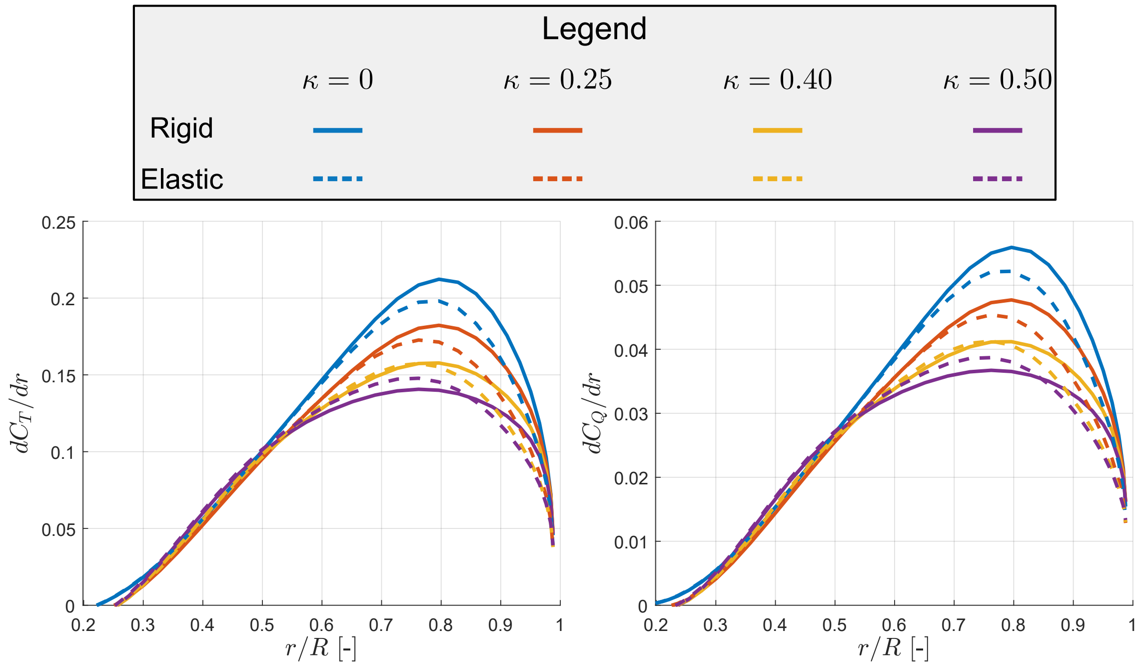

(a) Local thrust distribution

(b) Local torque distribution

Figure 12.5: The local aerodynamic loading distributions of multiple rigid and elastic forward-backwards swept blades for $J = 1.47$. (a) shows the thrust distributions and (b) shows the torque distributions.

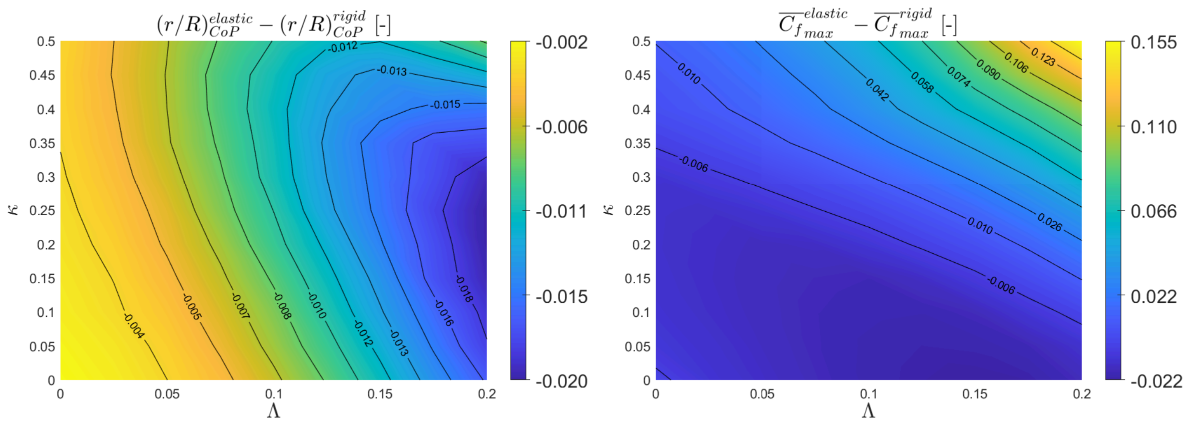

(a) Shift of the thrust radial centre of pressure due to elasticity.

(b) Change in maximum local force of the normalised load distribution due to elasticity.

Figure 12.6: Changes in characteristics of the local loading distributions due to elasticity as a function of the sweep parameters Λ and κ, for $J = 1.47$. (a) shows the radial shift of the radial centre of pressure due to elasticity. (b) shows the difference in maximum, normalised local loading due to elasticity.

12.3. ACOUSTIC PERFORMANCE OF FORWARD-BACKWARDS SWEPT BLADES

The impact of elasticity on the aerodynamic performance is still significant when adding forward-backwards sweep between the root and tip. While some configurations can diminish the effects of elasticity significantly, it is associated with a new adverse side-effect: the increase in the peak local loading. As such, structural deformations of the blade may now start to increase the sound levels of the blades.

Figure 12.7 shows the changes in OSPL and TSSP due to the effects of elasticity. The overall sound pressure levels in Figure 12.7a show decreasing noise levels due to the loss of thrust, similar to the contours of Figure 12.4. The blades with maximum blade sweep and forward sweep ($\Lambda = 0.20$, $\kappa = 0.50$) actually show increasing noise levels, being up to 0.5 dB louder. This is despite a slight loss in aerodynamic performance and the inboard shifting of the centre of pressure. This loss in aerodynamic performance is similar to that of the straight blade ($\Lambda = 0$, $\kappa = 0$), which only experiences a very slight reduction of noise levels (-0.11 dB). The increase in noise emissions by the fully swept blade correlates to the increase in the maximum normalised local loading of the elastic blade, shown in Figure 12.6b.
The TSSP in Figure 12.7b shows a very similar behaviour to the OSPL, this is because the difference in thrust has become minimal for a lot of the configurations. The thrust-normalised sound reduces due to the inboard shifting of the blade. The sound of the fully swept blade is increased due to the increase of the peak loading.

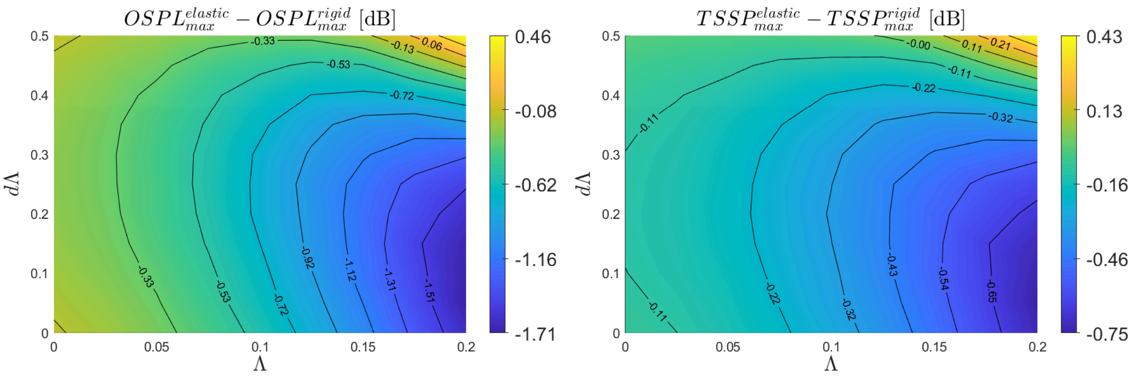

(a) Difference in Overall Sound Pressure Level due to elasticity.

(b) Difference in Thrust-Specific Sound Pressure Level due to elasticity.

Figure 12.7: The difference in noise emissions due to elasticity as a function of the sweep parameters Λ and κ for $J = 1.47$. (a) shows the difference in OSPL and (b) shows the difference in TSSP.

V

CONCLUSIONS

13
Conclusion

This thesis aimed to identify the effects of elasticity on the aerodynamic and acoustic performance of swept, low-noise propeller designs. Aerodynamic, acoustic and structural tools were developed and coupled in a propeller framework to be used in a parametric study of swept propeller designs. The Vortex Lattice Method was chosen to utilise its ability to discretise complex blade shapes. An aerodynamic tool using this methodology was developed for the inviscid, incompressible analysis of propeller configurations. The acoustic tool was based on the Helicoidal Surface Theory, which models blade sweep and dihedral as phase lag effects, such that sound waves destructively interfere. The structural tool was based on the Euler-Bernoulli beam theory, using Saint-Venant's theory to model torsional deformations. Each tool was individually validated, showing good agreement with high-fidelity and experimental data within the applicable operating conditions.

The three tools were coupled such that full rigid and elastic analyses could be quickly performed. The radial blade sweep was parametrised into two variables; the tip sweep Λ and the sweep curvature $d\Lambda$. A parametric study of these two parameters was performed, applying all combinations of sweep distribution to a baseline low-noise propeller design. The rigid and elastic data of the aerodynamic, acoustic and structural performance was obtained to identify any relations between these three disciplines.

Significant bending and torsional deformations were found on swept blades due to the aerodynamic and centrifugal loading. The centrifugal loading straightens the low-noise propeller blades, resulting in in-plane bending, which reduces the applied sweep. In turn, out-of-plane bending is induced in the direction of the freestream flow. This is due to the natural twisting of the blade, coupling the in- and out-of-plane bending deformations. Torsional deformations are caused by the aerodynamic load, resulting in a wash-out. Both these modes of deformation reduce the aerodynamic loads generated on the blade, as they reduce the local angle of attack. This reduction of thrust and torque can be as high as 20% at the operating condition of maximum efficiency. The changes in efficiency are negligible however. Since the structural deformations are concentrated near the tip, the local loading distributions also mainly reduce near the tip. This effectively shifts the loading inboard.
The changes in acoustic performance are in agreement with the changes in aerodynamic performance. Due to the reduction of forces on the blade, the Overall Sound Pressure Level decreases for the elastic blades, with changes of up to 2.5 dB. The difference in Overall Sound Pressure Level correlates with the reductions in thrust and torque due to elasticity. This reliance on the overall thrust level was eliminated by using the Thrust-Specific Sound Pressure. This sound metric showed a clear correlation with the changes in radial loading. The blades with the greatest inboard shift of the loading also experienced the greatest decrease in TSSP, with noise reductions of up to 1 dB in medium loading conditions. As such, structural deformations which are concentrated near the tip mainly reduce the aerodynamic loading near the tip. This reduction and inboard shift of the load reduces the noise emissions.

The comparison of the elastic swept blades to the straight blade showed that not only the elasticity, but also the application of blade sweep significantly alter the propeller performance. Since the sweep was added without any thrust-matching, the application of this blade sweep itself already changed the aerodynamic performance. The main result was an increase and outboard shift of the loading. This, in turn, increased the

OSPL and TSSP noise emissions. With the elasticity and blade sweep causing the opposite response in performance, the overall performance change of the elastic swept blades compared to the straight blade depends heavily on the amount of sweep that is applied. Though regardless of the overall comparison to the straight blade, including the structural deformations to analyse swept propeller blades is essential.

The extent of the structural deformations relies heavily on the advance ratio. As the aerodynamic loading grows, the torsional deformations will increase. The centrifugal forces are a function of the rotational speed. If the advance ratio is altered by changing the rotational speed, the centrifugal forces, and hence the bending deformations will also increase as the advance ratio decreases. These increasing deformations make it such that the impact of the elasticity becomes greater for higher loading conditions. This also means that the reductions in noise emissions grow. This is also true for the thrust-specific sound pressure level as the increased deformations near the tip move the aerodynamic loading further inboard.

An attempt was made to reduce the effect of elasticity on swept propeller blade performance by designing the blade such that the structural deformations may decrease. This was done by implementing forward sweep between the root and tip, while maintaining an overall backwards swept design. By implementing this blade sweep, the goal was to reduce the torsional deformations. These forward-backwards swept blades did experience a reduction in torsional deformation, but not by the mechanism in which they were intended. Instead, the increased bending deformations allowed the moment arm of the centrifugal forces to become significant enough such that they started to reduce the wash-out generated by the aerodynamic forces. By allowing the bending deformations to grow significantly enough, the centrifugal loads were able to overcome the negative twisting moments generated by the aerodynamic loads, resulting in positive twisting deformations.
In terms of aerodynamic response, the loss in loading due to the elasticity can be eliminated almost entirely this way. Locally, the loading moves inboard, but the peakiness of the distribution increases. This peakiness can increase noise emissions. This was actually reflected in the noise emissions both in terms of OSPL and TSSP. The forward-backwards swept blades with no loss in total loading, but an increase of local peakiness were louder compared to the rigid versions of the blades. Most forward-backwards swept blade designs still experienced a reduction in noise emissions due to the overall reduction and inboard shifting of the loading.

Clear connections have been identified between the aerodynamic, acoustic and structural performance of elastic, highly-swept propeller blades. It is clear that highly swept propeller blades may deform enough as to impact the aerodynamic and acoustic performance significantly. With changes in thrust of up to 20%, and an associated 2.5 dB decrease in noise levels, such impacts can not be neglected. Even when accounting for the changes in thrust level, changes in acoustic performance are still present due to the potential inboard or outboard shift of the loading. It is possible to reduce the effect of elasticity by incorporating more complex sweep distributions, as the centrifugal forces are able to generate a sufficient twisting moment when the blade bends significantly, or if dihedral is added.
Any research on the aerodynamic and acoustic performance of swept propeller blades should always consider the structural deformations. The effect of the elasticity will depend on how the blade deforms however. The swept low-noise propeller designs used in this research only deformed near the tip of the blade. This meant that the local aerodynamic loading effectively moved inboard. Blade designs that deform more consistently across the entire blade length may show differences in terms of the aerodynamic and acoustic response to these deformations.

14

Discussion

14.1. Limitations of Research

Due to the scale of this thesis, many limitations were imposed on the methodology and the parametric study. Some of these limitations are highlighted here.

Low-fidelity methods were employed to limit the computation time. It would not have been possible to perform such an extensive parametric study using coupled high-fidelity methods such as CFD and FEM. The usage of the low-fidelity methods significantly imposed on the suitable operating conditions. While it was attempted to stay within the suitable conditions of all three tools, some results are possibly outside the suitable boundaries.

The lack of viscosity and compressibility effects in particular limited the operating conditions and scale of the propeller. While the size and operation of the propeller can often be accounted for using scaling parameters, the involvement of aerodynamics, structures and acoustics makes this very challenging. In fact, Sodja et al. [21] already noted that the advance ratio is not a valid scaling parameter anymore when structures are involved. A flexible propeller will behave differently when the advance ratio is altered by changing the rotor speed, compared to changing the inflow velocity. As such, great care must be taken when scaling up the propeller or changing the operating conditions.

The parameterization of the backwards sweep had the benefit of only consisting of two variables, while being able to represent a significant amount of blade geometries. The parameter $d\Lambda$ did not alter the geometry linearly however. This was often seen in the results, where the contour plots showed changes to low amount of $d\Lambda$, but became constant near the upper limit. Furthermore, $d\Lambda$ was dependent on Λ , as no sweep curvature can be applied if no sweep is present. This means that for low Λ , $d\Lambda$ also has a negligible effect on the blade geometry.

14.2. Recommendation for Future Research

This thesis has only scratched the surface of the interactions between aerodynamics, acoustics and structures of swept propellers. There are many different directions in which a continuation of this research could go. Some ideas for future research are highlighted in this section.

One important aspect which was left unexplored was how the distribution of the structural deformation would impact the response of the aerodynamic and acoustic behaviour of the blade. The swept low-noise propellers had their structural deformations concentrated near the tip, which in turn only affected the local loading distributions near the tip. The flexible blades by Sodja et al. [20, 21] show considerably different deforming behaviour. These blades experience the greatest change in deformation near the root, these deformations then stay constant near the root. Additional research is required to determine if the elasticity effects are considerably different for such deformation distributions.

The implication of the effect of excessive out-of-plane bending, or blade dihedral, also requires further insight. Some blade designs showed that with enough out-of-plane bending, the centrifugal forces will start to generate significant twisting moments. This out-of-plane bending would be the same as adding dihedral to the blade design. Research by Sodja et al. [20, 21] already highlighted the effects that dihedral has on the aerodynamic and structural response. The centrifugal forces respond differently to the blade depending on the dihedral added. It would be interesting to investigate how the structural deformations change due to blade dihedral, and how this interacts with the acoustic performance.

The aerodynamic and structural tools were only connected in a simple aeroelastic coupling. Complex aeroelastic phenomena such as divergence and flutter were not considered. These highly flexible blades could be rendered inapplicable due to such phenomena however. An extensive dynamic aeroelastic study is required that analyses the aerodynamic and structural behaviour of highly swept propeller blades. Combining this with full unsteady aerodynamics and acoustics would allow for a fully time-dependent simulation. Real conditions can be approximated better by analysing non-uniform flow and the interactions between the propeller, pylon and wing.

Finally, research is required to identify the effects that structural deformations have on low-noise propeller design. Clearly the effects of elasticity on the aerodynamic and acoustic performance are too significant to ignore. A heavily swept propeller would have to be designed in such a way that adequate performance is obtained even after the blade has deformed. Design optimisations with structural deformations enabled and disabled should show how the overall propeller design would change. Since the deformations depend on the operating settings, multiple conditions would have to be included. Sodja et al. [20, 21] already attempted to design flexible blades that can be used in any operating condition without changing the pitch angle, by manipulating the elastic deformations. The final results were initial blade designs which would deflect such as to obtain optimal performance when deformed. Such an analysis, including the acoustic performance, may reveal new blade designs that could differ significantly from current low-noise propeller designs. endpart

A

Modelling Method Comparison

A.1. Aerodynamics Modelling Methods

There are several different methods for calculating propeller aerodynamics. With increasing computation time and fidelity, the most common methods are:

1. Blade Element Momentum (BEM)
2. Lifting-Line Theory (LLT)
3. Lifting-Surface Theory (LST)
4. 3D Panel Method
5. Computational Fluid Dynamics (CFD)

These methods are described in more detail further below. For each method, the basics are explained and any limitations are outlined. Although Computational Fluid Dynamics (CFD) is mentioned in this list, it is considered not suitable for a Multi-Disciplinary Analysis & Optimisation (MDAO) application, due to its computation time being considerably longer than the other methods. As such, it is not further elaborated upon.

A.1.1. Blade Element Momentum Method

The blade element momentum method is one of the most commonly used methods for calculating propeller performance, as it is one of the most simple and cheap methods. It works by dividing the propeller blade into many small elements in the radial direction [36]. These small segments are then evaluated as 2D airfoil sections, each with a chord length, airfoil shape and angle of attack. Airfoil polar data is used for the characteristics of each 2D airfoil section. The induced velocities of the propeller change the effective angle of attack and thus need to be calculated. This is done by combining the base blade element methodology with another model. The most commonly induced velocity calculation uses the momentum model [36]. The momentum model replaces the propeller with an actuator disk, adding axial and circumferential momentum to the flow. An iterative process between the blade element method and the momentum model converges towards an induced velocity distribution, and thus the loading distribution of the propeller [36].

The BEM method is computationally very cheap, but suffers from several drawbacks. Nonlinear flow effects such as flow separation, viscosity, and compressibility are not inherently included in the method. Instead, they can be accounted for via the airfoil polar data. Due to the evaluation of the propeller in 2D sections, complex flow phenomena such as crossflow and leading edge vortices cannot be modelled. The presence of tip vortices and multiple blades is merely accounted for using a tip factor, no interaction between blades is calculated. Finally, the BEM method is traditionally only applicable for simple straight wings. Modifications to analyse swept wings have been proposed by the likes of Gur & Rosen [36] and Bergmann et al [5] by applying simple sweep theory or correcting the force directions.

BEM results have been extensively compared with experimental data [36, 5, 8]. Generally, BEM is very accurate for simple propeller designs under low loading conditions. The accuracy diminishes at high blade loading due to the onset of non-linear flow effects. For swept blades, only low sweep angles under low loading conditions can be accurately predicted using BEM. Figure A.1 shows a comparison of BEM and test results of a swept propeller design by Geng et al [8]. It can be seen that the thrust predictions are accurate at low advance ratios, but the dominance of radial forces at low J makes the method less reliable there. For the power coefficient, viscous forces are underestimated at low J according to Geng et al [8].

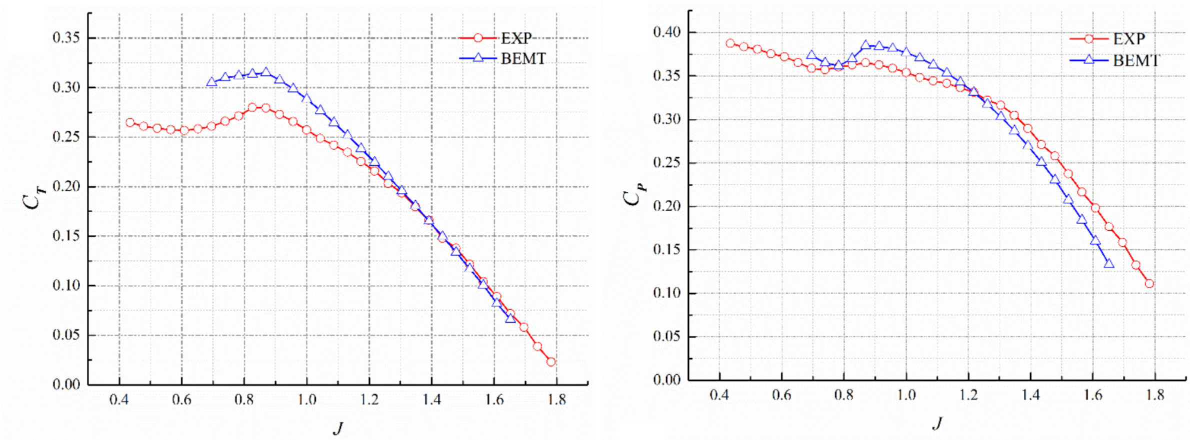

(a) Thrust coefficient at varying advance ratios.

(b) Power coefficient at varying advance ratio.s

Figure A.1: Comparison of BEM results and experimental data of a 6-bladed swept propeller. (from Geng et al [8])

A.1.2. LIFTING LINE THEORY

The lifting line theory is a method used to estimate the lift distribution of an unswept 3D wing. Using this theory, the wing is represented as a bound vortex filament, called the lifting line. Free vortices are placed at the ends of the bound vortex, generating a downwash on the entire wing [37]. The combination of a bound vortex with two free vortices at each of the tips is called a horseshoe vortex. The lift distribution cannot be accurately modelled with a single horseshoe vortex, as such a large number of horseshoe vortices are superimposed, each with a different length and vortex strength. This is shown in Figure A.2.

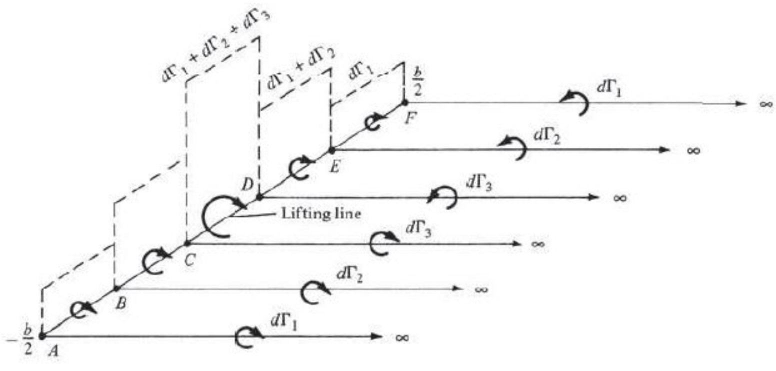

Figure A.2: Lifting Line representation of a wing using three horseshoe vortices. (from Anderson [37])

The circulation distribution of the bound vortices is found by solving the *fundamental equation of Prandtl's lifting-line theory* for Γ [37]:

$$\alpha(y_0) = \frac{\Gamma(y_0)}{\pi V_\infty c(y_0)} + \alpha_{L=0}(y_0) + \frac{1}{4\pi V_\infty} \int_{-b/2}^{b/2} \frac{(d\Gamma/dy)dy}{y_0 - y} \tag{A.1}$$

This circulation distribution is then used to find the induced angle of attack along the wing span. Similarly to the BEM method, airfoil polar data or thin airfoil theory may be used to solve for the sectional lift and drag coefficients, from which the lift and drag distributions are constructed. The lifting line theory can be applied to propellers by modelling each blade as a lifting line and accounting for the rotational velocity as a function of the local radius. Modelling each blade as a lifting line ensures that any interaction effects between the blades are taken into account. Thus, this method is more accurate than the blade element method, but also has an increased computational cost.

The LLT suffers from limitations similar to BEM. Viscosity, compressibility, and nonlinear flow phenomena are not modelled. Furthermore, the classical Lifting-Line Theory (LLT) only works for high-aspect ratio, unswept and untwisted wings. Although there have been several modifications to address this limitation by the likes of Phillips & Snyder [38] and Goates & Hunsaker [39]. They showed that with these modifications, the LLT may be used for small sweep angles. At higher sweep angles (> 30°), the precision decreases.

Validation of the LLT applied to propellers has shown that this method is adequate for the prediction of aerodynamic performance in hover and forward flight conditions [36, 40, 41]. It is also widely used in the maritime sector. Figure A.3 shows a comparison of multiple LLT implementations and experimental results of a maritime propeller by Epps & Kimball [41]. The LLT models show good agreement with the test data across the entire operating conditions.

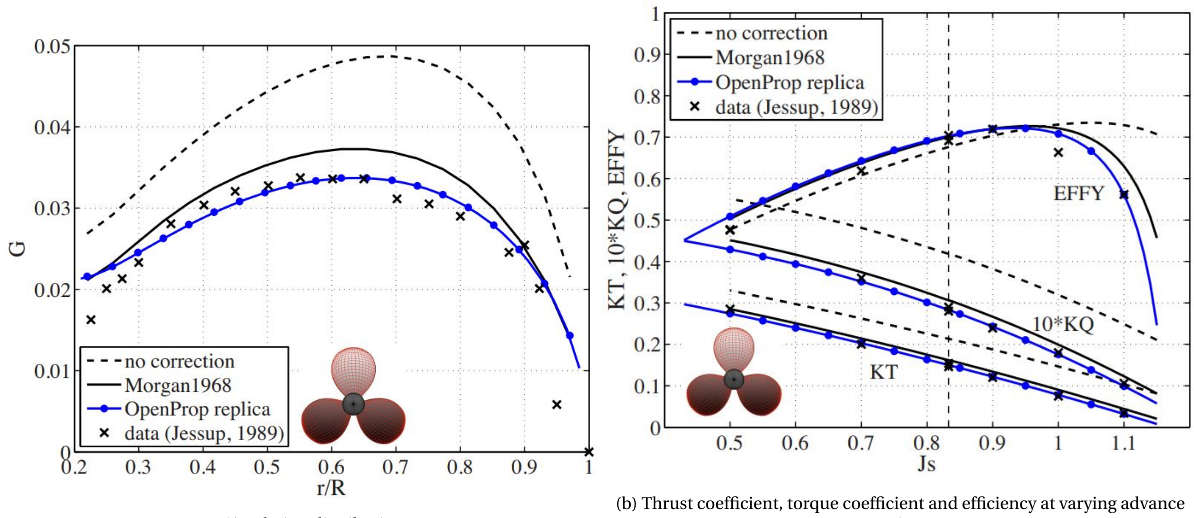

(a) Circulation distribution

(b) Thrust coefficient, torque coefficient and efficiency at varying advance ratios.

Figure A.3: Comparison of LLT results and experimental data of a maritime propeller. (from Epps & Kimball [41])

A.1.3. LIFTING SURFACE THEORY & VORTEX LATTICE METHOD

The previous methods only discretised the wing spanwise. It is possible to discretise the wing chordwise as well by adding multiple lifting lines in chordwise direction. This is called the Lifting-Surface Theory. Lifting lines in both spanwise and chordwise directions results in two vortex sheets, where their strength is a function of both spanwise and chordwise positions. Together, these two vortex sheets form a lifting surface. From the trailing edge onwards, the vortex sheet of the trailing vortices forms the wake vortex sheet [37].

The Vortex Lattice Method (VLM) is a type of implementation of lifting surface theory. In VLM, the wing is split into quadrilateral panels, on which horseshoe vortices with strength Γ_i are placed. The key difference from classical LST is that horseshoe vortices do not overlap, making VLM computationally more efficient. A panel with a horseshoe vortex is shown in Figure A.4. Each panel has a control point P, at which the flow tangency must be satisfied. Placing these panels across the entire wing results in a vortex-lattice system, shown in Figure A.5. The Biot-Savart law and the flow tangency condition are applied to solve for each vortex strength. The lift and drag distribution can then be determined.

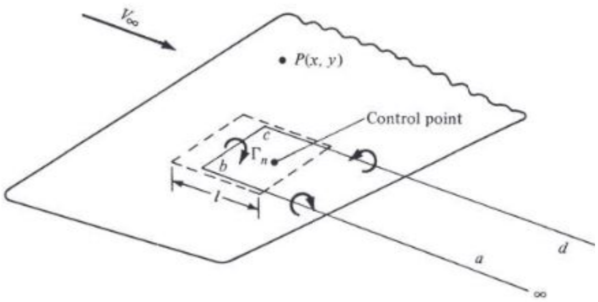

Figure A.4: A single panel with a horseshoe vortex. (from Anderson [37])

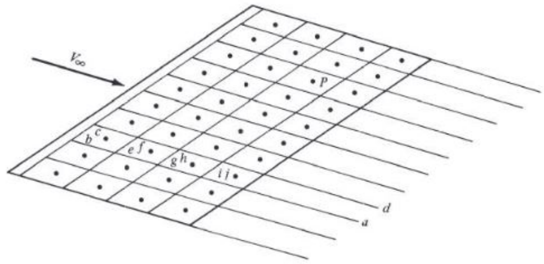

Figure A.5: Vortex Lattice system on a finite wing. (from Anderson [37])

Due to the discretisation of the wing in both spanwise and chordwise directions, any wing shape can be geometrically represented. No airfoil polar data is required either. These are major advantages over BEM and LLT, though computational costs are higher. The limitations of VLM are that the thickness of the wing is neglected. Compressibility, viscosity, and nonlinear flow phenomena are not inherently accounted for in VLM either. Modifications have been developed to account for many of these effects [40].

VLM is widely used due to its simplicity and low computational costs. Comparisons with experimental data have shown that Vortex Lattice Method for propeller applications are accurate when minimal nonlinear flow effects occur [42, 43]. Even the performance of advanced propfan designs with thin blades and high sweep angles can be accurately calculated using VLM, as can be seen in Figure A.6. This figure shows the predictions of the efficiency and power coefficient of two advanced turboprop designs with eight blades. The predictions of the SR-1 propeller on the left show very good agreement with the experimental data. The more highly swept SR-3 propeller predictions on the right are less accurate. This is due to centrifugal forces distorting the SR-3 propeller shape according to Kobayakawa & Onuma [42].

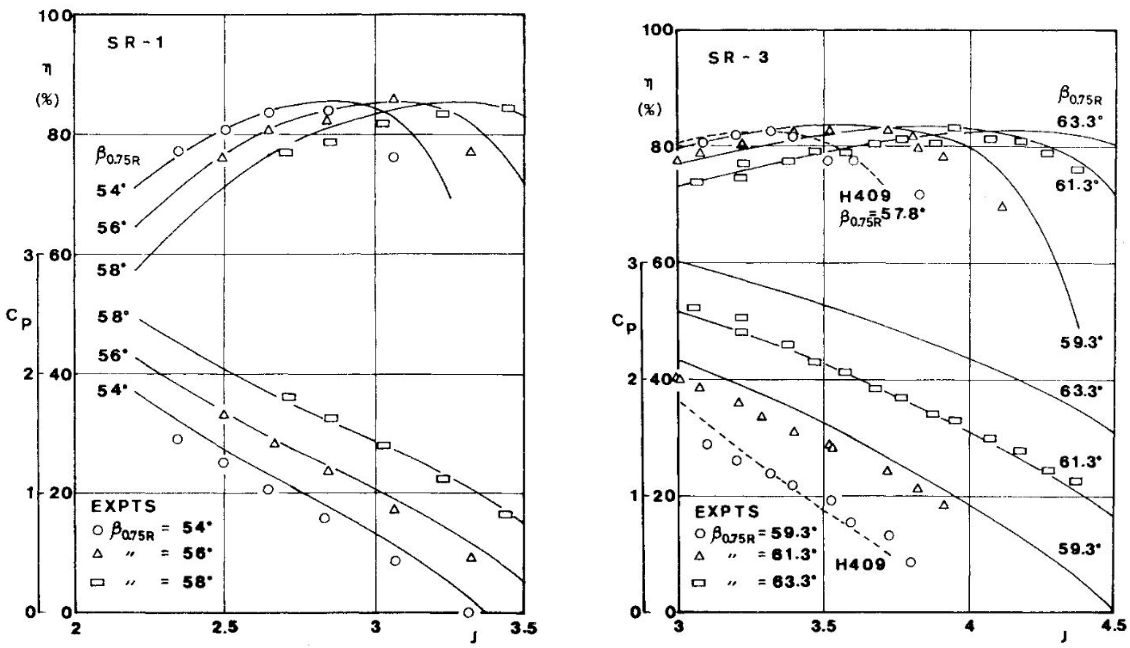

(a) Efficiency and power coefficient at varying advance ratios for the SR-1 propeller.

(b) Efficiency and power coefficient at varying advance ratios for the SR-3 propeller.

Figure A.6: Comparison of VLM results and experimental data of advanced turboprop blades. (from Kobayakawa & Onuma [42])

A.1.4. 3D PANEL METHOD

Panel methods allow for the aerodynamic analysis of any shape, 2D or 3D. They function by covering a surface in singularities such as vortices, sources, and doublets. The strengths of these singularities are solved by applying flow tangency on each panel, which implies that the flow may not go through the body. This makes the body surface a streamline of the flow. Figure A.7 shows a body surface covered in panels, each with a control point in the middle where the normal velocity is solved to be zero.

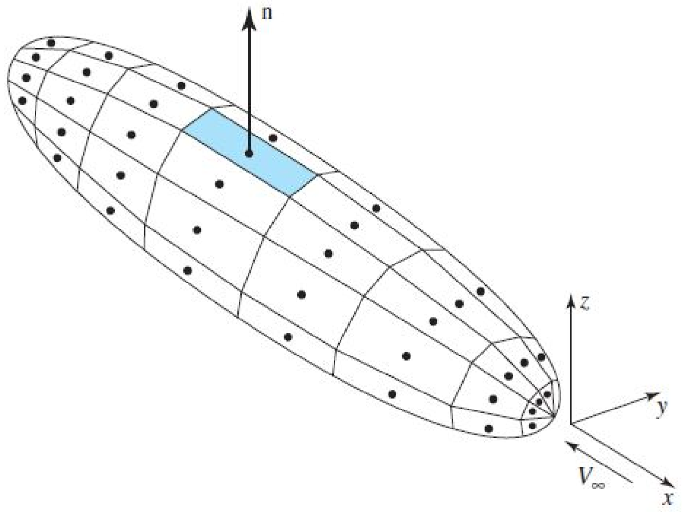

Figure A.7: Panel distribution of a general non-lifting body. (from Anderson [37])

Panel methods are more computationally expensive, but they allow for the evaluation of any body shape, and can also be applied to propellers. Nevertheless, panel methods are also considerably more complex, as the distribution of panels on the body is a non-trivial problem, which can significantly impact the results. Shown in Figure A.8 is the analysis of a 6-bladed propeller [35]. The results are not as accurate as one might expect from a panel method. Keil claims this is partly due to inaccuracies of the airfoil shape in FlightStream compared to the propeller model. Other issues such as improper meshing and inaccurate viscosity modelling may also reduce the accuracy.

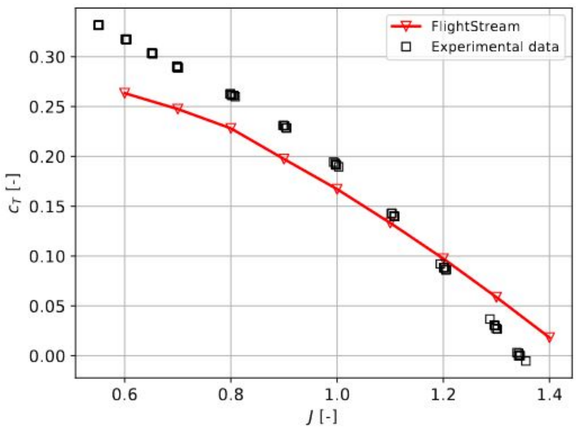

(a) Thrust coefficient at varying advance ratios.

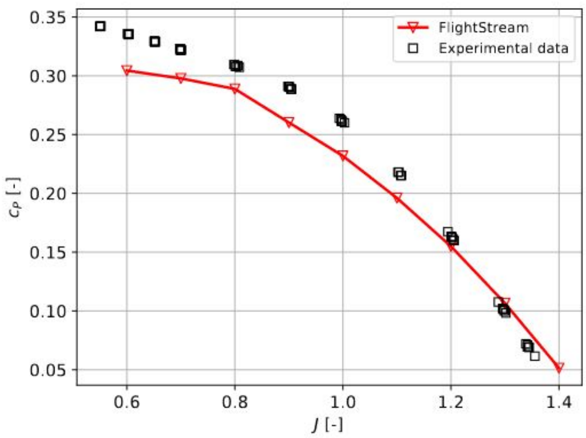

(b) Power coefficient at varying advance ratios.

Figure A.8: Comparison of FlightStream results and experimental data of 6-bladed propeller. (from Keil [35])

A.1.5. COMPARISON AERODYNAMIC MODELLING METHODS

Validation cases for each aerodynamic modelling method were shown. It is difficult to assign an order of accuracy based on these validation cases though. Each case pertains to a different propeller and experimental data. The magnitudes of error for both experimental and modelling results will differ. Instead, to truly showcase the accuracy of each method, an analysis using multiple different methods is required that encompasses wide operating conditions and propeller designs. In this section, some comparisons made in current literature are shown to provide more context on the accuracy of the different methods.

GUR & ROSEN - 2008

Gur & Rosen [36] compared different blade element methods for three propeller designs, a two-bladed system, a four-bladed system, and a two-swept-blade system. The methods used are BEM, LLT and vortex theory. All of these models were applied as methods of blade element, meaning that the induced velocities are only calculated to obtain the effective angle of attack at each blade segment. A database of 2D airfoil data is then used to find the sectional lift and drag coefficients. Note that the vortex theory is not the same as the Vortex Lattice Method. This method is not discussed as it is not as commonly applied.

The results of the four-bladed propeller are shown in Figure A.9. The models to consider are the Simplified Momentum and Lifting Line with Prescribed Wake. It can be seen in Figure A.9 that BEM slightly underestimates thrust and power, while LLT slightly overestimates these parameters. Both are less accurate at the lower limit of advance ratio for each pitch setting, as this is where flow separation starts to occur. Another detail that can be noted from the paper by Gur & Rosen [36] is that from the two-bladed system (not shown here) to the four-bladed system, BEM clearly loses accuracy, while LLT does not. This could be due to BEM only accounting for the number of blades with a simple tip factor, while LLT models the interference between the blades. However, the two- and four-bladed experiments are completely unrelated, and thus this can not be stated with complete certainty, as other factors might be at play.

The results of the swept propeller system are shown in Figure A.10. Interestingly, the results of BEM are quite accurate. Meanwhile LLT overestimates the thrust and power. Gur & Rosen [36] note that due to elastic torsion of the experimental blade, which is not accounted for in the numerical models, the results are generally overpredicted. Although the BEM model is relatively accurate here, validation of the same or similar sweep corrections in other studies such as by Geng et al [8] and Bergmann et al [5] have shown poorer accuracy. As such, it may be possible to obtain accurate results for swept blades for some cases with BEM, but it is not a reliable method.

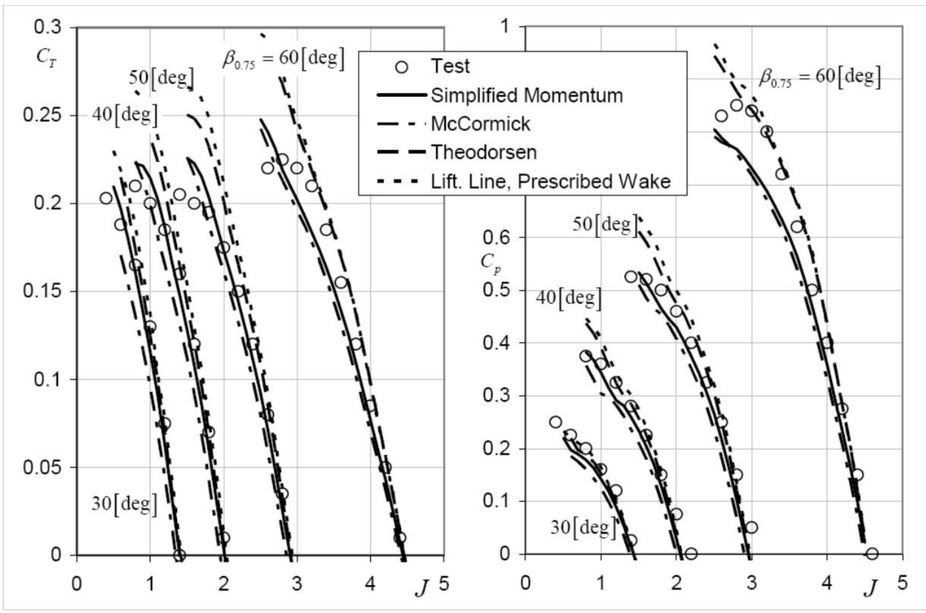

Figure A.9: Comparison of different blade element models and test results of a four-bladed propeller. (from Gur & Rosen [36])

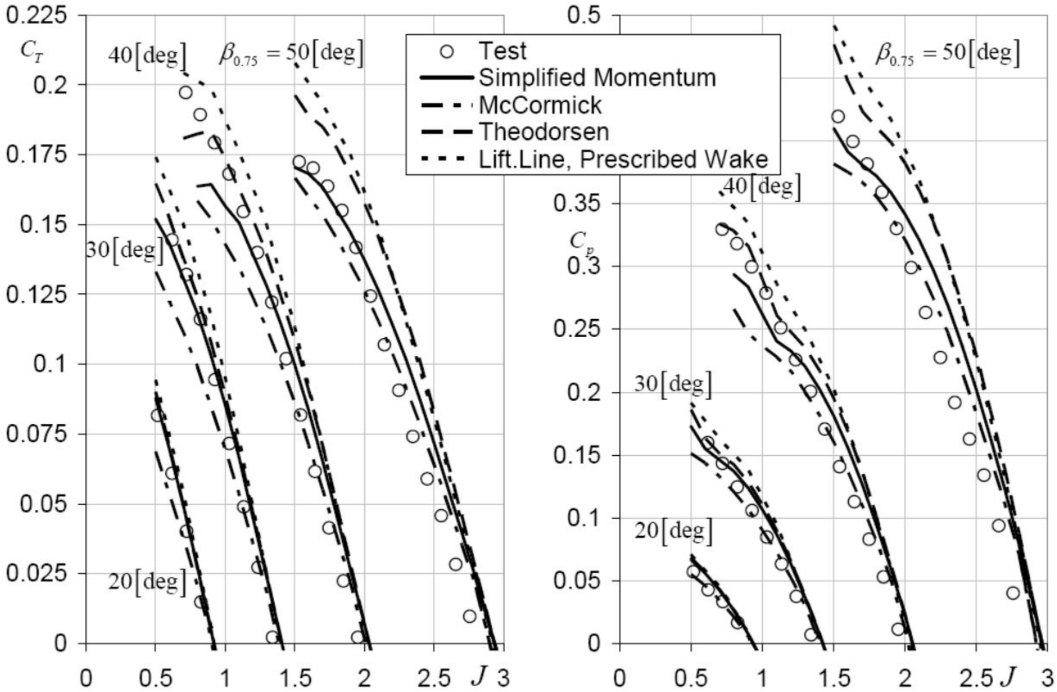

Figure A.10: Comparison of different blade element models and test results of a propeller with two swept blades. (from Gur & Rosen [36])

BURGER ET AL - 2007

Another comparison including the Vortex Lattice Method is required to show the advantages of this method. Burger et al [44] compared experimental data of a propeller with a lifting line and vortex lattice solution, shown in Figure A.11. The lifting line and vortex lattice solutions are almost identical. This is due to the propeller being straight with no camber. Thus the lifting surface method provides no advantage in accuracy. Compared to the experimental data, the numerical predictions are underestimated. Though for the power coefficient predictions, viscous drag is neglected.

Other comparisons of LLT and VLM such as by Karali et al [45] also show almost identical results. In this case, the lifting surfaces of a simple unmanned aerial vehicle were evaluated. Again, the simple geometry of the design does not require the increased fidelity that VLM provides. Instead, an analysis of a complex wing or propeller is required to truly show the increased accuracy of VLM, the author of this literature study is unaware of such a paper though.

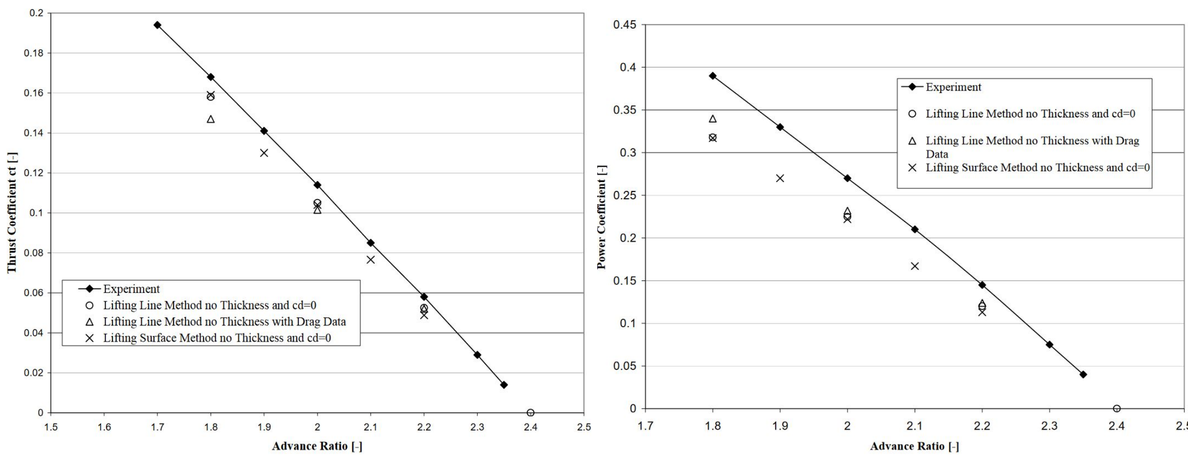

(a) Thrust coefficient at varying advance ratios.

(b) Power coefficient at varying advance ratios.

Figure A.11: Comparison of LLT and VLM with experimental data of a three-bladed propeller. (from Burger et al [44])

A.1.6. AERODYNAMIC MODEL SELECTION

Based on the tools available and the discussion of each of the aerodynamic modelling methods in Part I, the most suitable method is chosen. The four methods under consideration are:

- Blade Element Momentum
- Lifting-Line Theory
- Vortex Lattice Method
- 3D Panel Method

BEM and LLT tools compatible with the propeller MDAO framework are already available. Furthermore, it was shown that these methods are accurate and cheap for simple propeller designs. For low-noise propellers, their applicability greatly diminishes due to their decreased accuracy. Besides, significant modifications are required to even allow for the discretisation of these complex shapes. Instead, a new aerodynamic tool, based on either VLM or a panel method will need to be developed. Theoretically, the VLM and panel method should be more appropriate to analyse low-noise propellers. Their usage of quadrilateral panels allows for the representation of any blade shape. The panel method achieves the highest accuracy in discretising the propeller due to it also modelling the thickness, while this is ignored with VLM. In fact, a panel method might have been the most suitable method for a purely aerodynamic analysis. The added computational costs are considered too great of a drawback to include it in a MDAO framework. Besides, increased accuracy is not guaranteed due to the complexity of meshing and nonlinear flow effects. While the increased fidelity of the VLM compared to BEM and LLT could not be shown numerically, the underlying principles should prove this methodology to be the most suitable for this research. It also has the benefit of ease of development and integration due to its similarity with the existing LLT tool.

A.2. NOISE MODELLING METHODS

Noise prediction methods are often based on the Fwowcs Williams and Hawkings equation, the linear form of which is shown in Equation (A.2) [4]. The left side of this equation is the linear wave operator acting on the acoustic pressure p. The right side of the equation contains the source terms. The first term represents the thickness noise, and the second term represents the loading noise. The two methods for solving this equation are the time-domain methods and the frequency-domain methods. Each of these methods are explained further below.

$$\nabla^2 p - \frac{1}{c^2}\frac{\delta^2 p}{dt^2} = -\frac{\delta}{\delta t}\left[\rho_0 v_n |\nabla f| \delta(f)\right] + \frac{\delta}{\delta x_i}\left[l_i |\nabla f| \delta(f)\right] \tag{A.2}$$

A.2.1. TIME-DOMAIN METHODS

Time-domain methods solve the Fwowcs Williams and Hawkings equation directly in terms of space-time variables. They allow for the evaluation of the blade geometry with any level of precision. The result is the acoustic pressure waveform as a function of time, $p(t)$.

FARASSAT 1975 - 1992

Farassat published many papers between 1975 and 1992 on the modelling of noise. He developed multiple formulations to solve the Fwowcs Williams and Hawkings equation, dubbing them Formulations 1, 1A, 2 and 3. For subsonic propeller blades, Formulation 1A is recommended, the derivation of which can be found in Farassat's paper [46].

Farassat's Formulations have been modified and adapted into several commonly used programmes such as NASA's Aircraft Noise Prediction Program (ANOPP) [47]. Extensive validation by the likes of Weir and Nguyen has shown good agreement for propeller acoustic predictions in level and climb configurations [47]. The dive attitude configurations show a poor correlation.

A.2.2. FREQUENCY-DOMAIN METHODS

Frequency-domain methods use Fourier transformations to remove time from the wave equation. This is advantageous because it eliminates the need for time-accurate solutions, reducing computational time. Nevertheless, due to the Fourier transformations, some precision in blade geometry is lost as the thin-blade assumption is applied.

HANSON 1976 - 1992

Hanson developed a theory for the prediction of propeller noise between 1976 and 1992. His solution for the Fwowcs Williams and Hawkings equation in the frequency domain, the Helicoidal Surface Theory, has become one of the most widely used methods [24]. The Helicoidal Surface Theory approximates that the thickness and loading sources act on an advance helix, which is a surface swept out by a radial line rotating at angular speed n and translating at flight speed V_∞ [4]. The complete derivation of the method can be found in Hanson's paper [24]. The theory allows for the evaluation of swept and bent blades, appearing as phase lag effects [24]. These blade parameters, in addition to others, appear explicitly. Thus, their effects on noise amplitude and phase can be easily evaluated.

Hanson's prediction method has been extensively validated since its conception [47]. More recently, Kotwicz Herniczek et al [48] compared different frequency-domain methods, including the Hanson method. The 14 experimental test cases consisted of a range of propeller geometries, blade numbers, microphone locations, tip speeds and forward Mach speeds. Note that the acoustic models were coupled with a BEM model. Though any aerodynamic error was considered to have little impact on the acoustic solution according to Kotwicz Herniczek et al. [48]. From all the test cases, Hanson's model had the lowest average error of 5.9 dB. In particular, Hanson's model underpredicts low-speed swept propellers. These errors are not insignificant, but the low computational time and the ability to predict acoustic trends are still of great value for MDAO purposes.

A.2.3. ACOUSTIC METHOD SELECTION

Two acoustic solvers have been identified, namely the time-domain method by Farassat [46] and the frequency-domain method by Hanson [24]. Both methods have been widely applied for low-noise propeller design. At the FPP department, a tool based on Hanson's helicoidal surface theory has already been developed. The advantage of this method is the fact that it allows for the evaluation of swept and bent blades. Validation of this method has shown that while it may produce errors in acoustic calculations, design trends are generally predicted well. On the basis of these advantages, and the fact that a tool is already available, Hanson's helicoidal surface theory will be used as the acoustic analysis tool for this research.

A.3. STRUCTURAL ANALYSIS METHODS

Structural analysis methods are required to calculate the internal stresses and deflections discussed in the previous section. While numerical Finite Element Modelling (FEM) is highly accurate, its high computational time is a major drawback. As such, FEM is not considered any further. Instead, simpler structural methods are evaluated, in the form of solid mechanics theory of beams. The solid mechanics theory of beams is a simple tool that allows for the structural analysis of numerous structures. Several beam theories have been developed, each with different levels of accuracy. The Euler-Bernoulli beam theory is highly suitable for long, slender beams and is thus most commonly used for the analysis of propeller blades. Besides the Euler-Bernoulli beam theory, there is also the Timoshenko-Ehrenfest theory, which is also suitable for short, thick beams. Both methods are discussed and an application to propeller structural design is referenced.

A.3.1. EULER-BERNOULLI BEAM THEORY

The Euler-Bernoulli beam theory describes the behaviour of slender beams subject to bending. Important beam parameters such as bending distribution, deflections, and internal stresses can be obtained with it. The Euler-Bernoulli beam theory makes three major assumptions [49]:

- The cross-section is infinitely rigid in its own plane.
- The cross-section of a beam remains plane after deformation.
- The cross-section remains normal to the deformed axis of the beam.

These assumptions are valid for long, slender beams of isotropic material with solid cross-sections. Additionally, deflections should remain small. Any deviation from these restrictions will result in a loss of accuracy [49]. The Euler-Bernoulli beam theory does not account for any twisting. Therefore, it is combined with a theory of torsion. Specifically, Saint-Venant's theory of torsion allows for the analysis of a beam with an arbitrary cross-sectional shape, placed under torsion [49].

SODJA ET AL 2014 - 2018

The Euler-Bernoulli beam theory has been used for propeller structural analysis by Sodja et al [20]. A mathematical model for the design of flexible propellers, based on the Euler-Bernoulli beam theory and Saint-Venant theory of torsion, was constructed. This structural model was coupled with an extended Blade Element Momentum (BEM) model to evaluate the aerodynamic performance. The structural analysis tool, and its coupling with the BEM model, has been extensively validated using straight, swept forward and swept backward blades. Some of the results are shown in Figure A.12. Comparison with FEM simulations for a backwards swept blade in Figures A.12a to A.12c shows very good agreement for in- and out-of-plane bending. Torsional deformations are underestimated. Compared to the experimental data in Figure A.12d, the blade deflections are underpredicted. This error may be attributed to an error in the aerodynamic prediction (BEM), which would also reflect in the structural predictions. In fact, Sodja et al [21] state that this is in fact the case for the straight and backwards swept blade.

Though obviously, errors are present within the Euler-Bernoulli beam theory, it can correctly predict the trend of all the blade deflections. This, in combination with its low computational costs, make this a suitable method for the structural analysis of low-noise propellers.

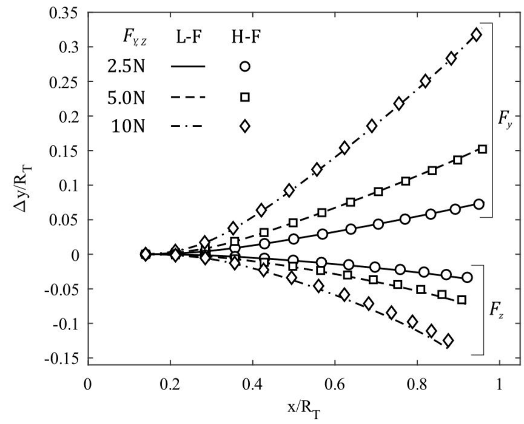

(a) Euler-Bernoulli and FEM predictions of blade deflections in y direction due to a tip force on a backwards swept blade.

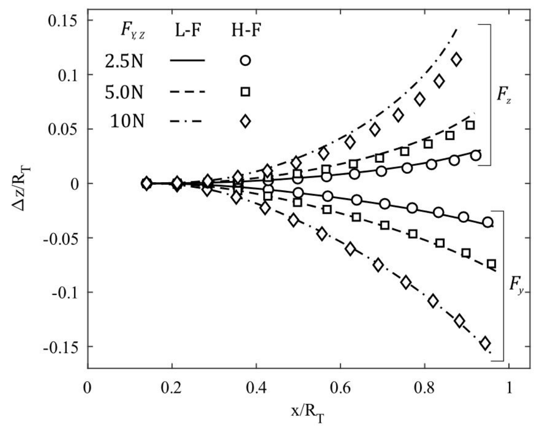

(b) Euler-Bernoulli and FEM predictions of blade deflections in z direction due to a tip force on a backwards swept blade.

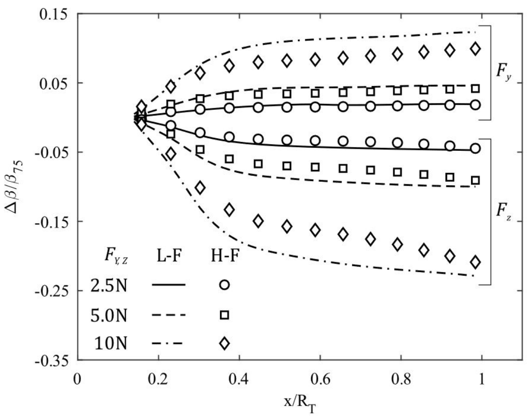

(c) Euler-Bernoulli and FEM predictions of torsional deformations due to a tip force on a backwards swept blade.

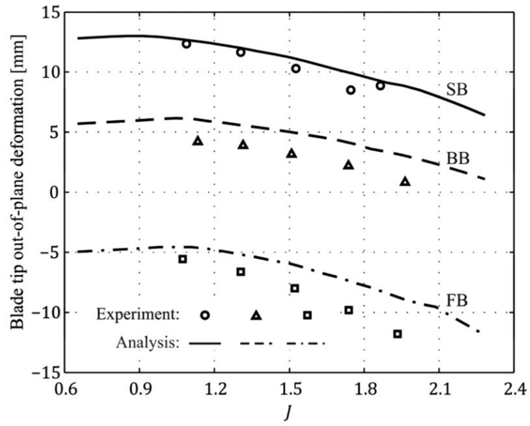

(d) Euler-Bernoulli predictions and experimental data of out-of-plane deformations on multiple (swept) blades.

Figure A.12: Validation of Euler-Bernoulli beam theory implementation. (from Sodja et al [20, 21])

A.3.2. TIMOSHENKO-EHRENFEST BEAM THEORY

The Timoshenko-Ehrenfest beam theory uses the same physical principles as the Euler-Bernoulli beam theory. The difference is that shear deformations are not neglected. The assumption that the cross-section remains normal to the deformed axis of the beam no longer holds. This makes the Timoshenko-Ehrenfest beam theory more suitable for short, thick beams.

MÖHREN ET AL - 2023

The Timoshenko-Ehrenfest beam theory has been applied to propeller structural analysis by Möhren et al [50]. In this study, anisotropic materials are used for a backwards swept blade. The elastic axis of the blade is represented by straight beam elements between the shear centres of each cross-section. These beam elements have twelve degrees of freedom. The structural model was compared against FEM, shown in Figure A.13. Predictions of deformations in the z-direction are almost identical in Figure A.13a. In y-direction, the deformations become nonlinear at higher applied loads. This is not captured by the linear beam theory and, as such, is inaccurate for larger deflections. The torsional deformations in Figure A.13c are almost consistently underestimated compared to the FEM data. A more accurate bending-torsion coupling might improve this fitting according to Möhren et al [50].
Similar to the Euler-Bernoulli beam theory, the Timoshenko beam theory correctly predicts the linear trends of all the deflections in the propeller blades. As such, it may also be considered a suitable low-noise propeller structures analysis tool.

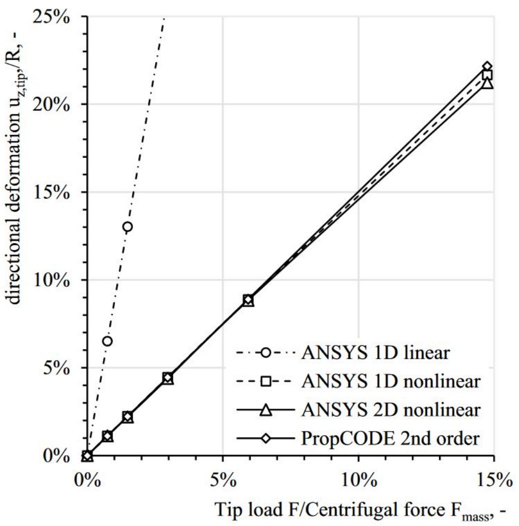

(a) Timoshenko and FEM predictions of blade deflections in z direction due to a tip load.

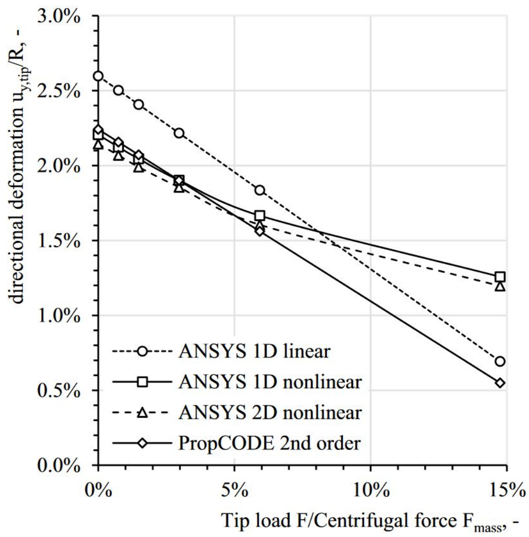

(b) Timoshenko and FEM predictions of blade deflections in y direction due to a tip load.

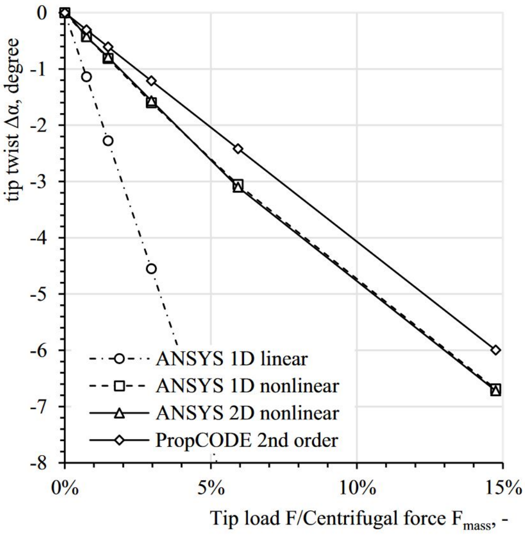

(c) Timoshenko and FEM predictions of torsional deformations due to a tip load.

Figure A.13: Validation of Bergmann et al Timoshenko-Ehrenfest beam theory implementation. (from Möhren et al [50])

A.3.3. STRUCTURAL MODEL SELECTION

Two low-fidelity structural modelling methods suitable for propellers have been identified; the Euler-Bernoulli beam theory and the Timoshenko-Ehrenfest beam theory. The Euler-Bernoulli beam theory is only suitable for slender beams, while the Timoshenko-Ehrenfest model also allows for short, thick beams. The remaining underlying physics of the two models are identical. Propeller blades are usually thin and slender, thus the Euler-Bernoulli beam theory is perfectly suitable for a low-fidelity structural analysis. Furthermore, a structural tool based on the Euler-Bernoulli beam theory has already been developed at the FPP department. As such, the structural analysis in this research is performed using an Euler-Bernoulli beam theory and the Saint Venant theory of torsion.

References

[1] *Aircraft Technology Roadmap to 2050*. International Air Transport Association, 2019.

[2] K. d. Waal. *Low-noise propeller design for future regional aviation - NLR News*. Royal Netherlands Aerospace Centre. Oct. 25, 2022. URL: https://www.nlr.org/news/low-noise-propeller-design-for-future-regional-aviation/ (visited on 05/25/2023).

[3] *New airport charges at Schiphol encouraging cleaner, quieter aircraft*. New airport charges at Schiphol encouraging cleaner, quieter aircraft. Oct. 31, 2018. URL: https://news.schiphol.com/new-airport-charges-at-schiphol-encouraging-cleaner-quieter-aircraft/ (visited on 03/14/2024).

[4] H. H. Hubbard. *Aeroacoustics of Flight Vehicles: Theory and Practice. Volume 1: Noise Sources*. WRDC-TR-90-3052-VOL-1. NTRS Author Affiliations: NASA Langley Research Center NTRS Document ID: 19920001380 NTRS Research Center: Legacy CDMS (CDMS). Aug. 1, 1991. URL: https://ntrs.nasa.gov/citations/19920001380 (visited on 04/06/2023).

[5] O. Bergmann, F. Möhren, C. Braun, and F. Janser. *AERODYNAMIC ANALYSIS OF SWEPT PROPELLER WITH BET AND RANS*. Sept. 1, 2021.

[6] O. Bergmann, F. Götten, C. Braun, and F. Janser. “Comparison and evaluation of blade element methods against RANS simulations and test data”. In: *CEAS Aeronautical Journal* 13.2 (Apr. 1, 2022), pp. 535–557. ISSN: 1869-5590. DOI: 10.1007/s13272-022-00579-1. URL: https://doi.org/10.1007/s13272-022-00579-1 (visited on 05/09/2023).

[7] O. Bergmann, F. Möhren, C. Braun, and F. Janser. “On the influence of elasticity on swept propeller noise”. In: *AIAA SCITECH 2023 Forum*. AIAA SCITECH 2023 Forum. National Harbor, MD & Online: American Institute of Aeronautics and Astronautics, Jan. 23, 2023. ISBN: 978-1-62410-699-6. DOI: 10.2514/6.2023-0210. URL: https://arc.aiaa.org/doi/10.2514/6.2023-0210 (visited on 05/02/2023).

[8] X. Geng, T. Hu, P. Liu, T. Sinnige, and G. Eitelberg. “Analysis of Thrust-Scaled Acoustic Emissions of Aircraft Propellers and Their Dependence on Propulsive Efficiency”. In: *32nd Congress of the International Council of the Aeronautical Sciences*. ICAS 2021 (2021). Publisher: International Council of the Aeronautical Sciences.

[9] X. Geng, P. Liu, T. Hu, Q. Qu, J. Dai, C. Lyu, Y. Ge, and R. A. D. Akkermans. “Multi-fidelity optimization of a quiet propeller based on deep deterministic policy gradient and transfer learning”. In: *Aerospace Science and Technology* 137 (June 1, 2023), p. 108288. ISSN: 1270-9638. DOI: 10.1016/j.ast.2023.108288. URL: https://www.sciencedirect.com/science/article/pii/S1270963823001852 (visited on 04/11/2023).

[10] B. Marinus, M. Roger, and R. Braembussche. *Aeroacoustic and Aerodynamic Optimization of Aircraft Propeller Blades*. June 7, 2010. DOI: 10.2514/6.2010-3850.

[11] B. Marinus, M. Roger, R. Braembussche, and W. Bosschaerts. “Multidisciplinary Optimization of Propeller Blades: focus on the aeroelastic results”. In: 47th AIAA/ASME/SAE/ASEE Joint Propulsion Conference and Exhibit 2011. July 31, 2011. DOI: 10.2514/6.2011-6059.

[12] B. Marinus, M. Roger, R. Braembussche, and W. Bosschaerts. *Multidisciplinary Optimization of Propeller Blades: focus on the aeroacoustic results*. June 5, 2011. DOI: 10.2514/6.2011-2801.

[13] B. Marinus. “Comparative study of effects of sweep and humps on high-speed propeller blades”. In: *AIAA Journal* 52.4 (2014), pp. 739–746. ISSN: 0001-1452. DOI: 10.2514/1.J052833.

[14] L. L. M. Veldhuis. “Propeller Wing Aerodynamic Interference”. In: (2005). URL: https://repository.tudelft.nl/islandora/object/uuid%3A8ffbde9c-b483-40de-90e0-97095202fbe3 (visited on 04/06/2023).

[15] T. Sinnige. "Aerodynamic and Aeroacoustic Interaction Effects for Tip-Mounted Propellers: An Experimental Study". PhD thesis. Delft University of Technology, 2018. DOI: 10.4233/UUID:214E1E9A-C53E-47C7-A12C-B1EB3EC8293B. URL: http://resolver.tudelft.nl/uuid:214e1e9a-c53e-47c7-a12c-b1eb3ec8293b (visited on 04/06/2023).

[16] E. Schülein, H. Rosemann, and S. Schaber. "Transition Detection and Skin Friction Measurements on Rotating Propeller Blades". In: 28th AIAA Aerodynamic Measurement Technology, Ground Testing, and Flight Testing Conference 2012. June 27, 2012. DOI: 10.2514/6.2012-3202.

[17] T. Sinnige, T. C. A. Stokkermans, D. Ragni, G. Eitelberg, and L. L. M. Veldhuis. "Aerodynamic and Aeroacoustic Performance of a Propeller Propulsion System with Swirl-Recovery Vanes". In: *Journal of Propulsion and Power* 34.6 (Nov. 2018). Publisher: American Institute of Aeronautics and Astronautics, pp. 1376–1390. ISSN: 0748-4658. DOI: 10.2514/1.B36877. URL: https://arc.aiaa.org/doi/10.2514/1.B36877 (visited on 05/23/2023).

[18] F. E. Weick. *Aircraft Propeller Design*. Google-Books-ID: 63ZTAAAAMAAJ. McGraw-Hill Book Company, Incorporated, 1930. 320 pp. ISBN: 978-0-598-63087-2.

[19] D. B. Hanson. "Influence of Propeller Design Parameters on Far-Field Harmonic Noise in Forward Flight". In: *AIAA Journal* 18.11 (Nov. 1980). Publisher: American Institute of Aeronautics and Astronautics, pp. 1313–1319. ISSN: 0001-1452. DOI: 10.2514/3.50887. URL: https://arc.aiaa.org/doi/10.2514/3.50887 (visited on 05/22/2023).

[20] J. Sodja, R. Drazumeric, T. Kosel, and P. Marzocca. "Design of Flexible Propellers with Optimized Load-Distribution Characteristics". In: *Journal of Aircraft* 51.1 (Jan. 2014). Publisher: American Institute of Aeronautics and Astronautics, pp. 117–128. ISSN: 0021-8669. DOI: 10.2514/1.C032131. URL: https://arc.aiaa.org/doi/10.2514/1.C032131 (visited on 04/14/2023).

[21] J. Sodja, R. De Breuker, D. Nozak, R. Drazumeric, and P. Marzocca. "Assessment of low-fidelity fluid–structure interaction model for flexible propeller blades". In: *Aerospace Science and Technology* 78 (July 1, 2018), pp. 71–88. ISSN: 1270-9638. DOI: 10.1016/j.ast.2018.03.044. URL: https://www.sciencedirect.com/science/article/pii/S1270963817319417 (visited on 04/13/2023).

[22] J. Goyal. *Hanson's Model in Frequency Domain - Tonal Noise of Rotors in Uniform Inflow*. In collab. with TU Delft, Faculty Of Aerospace Engineering, Department Of Flow Physics And Technology. Version 1. Mar. 4, 2024. DOI: 10.4121/7DA5AA45-E44B-4FA3-9407-8BF61E835D99.V1. URL: https://data.4tu.nl/datasets/7da5aa45-e44b-4fa3-9407-8bf61e835d99/1 (visited on 03/04/2024).

[23] J. Katz and A. Plotkin. *Low-Speed Aerodynamics*. 2nd ed. Cambridge Aerospace Series. Cambridge: Cambridge University Press, 2001. ISBN: 978-0-521-66552-0. DOI: 10.1017/CBO9780511810329. URL: https://www.cambridge.org/core/books/lowspeed-aerodynamics/077FAF851C4582F1B7593809752C44AE (visited on 06/15/2023).

[24] D. B. Hanson. "Helicoidal Surface Theory for Harmonic Noise of Propellers in the Far Field". In: *AIAA Journal* 18.10 (Oct. 1980). Publisher: American Institute of Aeronautics and Astronautics, pp. 1213–1220. ISSN: 0001-1452. DOI: 10.2514/3.50873. URL: https://arc.aiaa.org/doi/10.2514/3.50873 (visited on 04/20/2023).

[25] N. van Arnhem. "Unconventional Propeller–Airframe Integration for Transport Aircraft Configurations". PhD thesis. Delft University of Technology, Mar. 16, 2022. DOI: 10.4233/uuid:4d47b0db-1e6a-4f38-af95-aafd33c29402.

[26] T. C. A. Stokkermans and L. L. M. Veldhuis. "Propeller Performance at Large Angle of Attack Applicable to Compound Helicopters". In: *AIAA Journal* 59.6 (2021). Publisher: American Institute of Aeronautics and Astronautics _eprint: https://doi.org/10.2514/1.J059509, pp. 2183–2199. ISSN: 0001-1452. DOI: 10.2514/1.J059509. URL: https://doi.org/10.2514/1.J059509 (visited on 04/01/2024).

[27] Q. Li, K. Öztürk, T. Sinnige, D. Ragni, G. Eitelberg, L. Veldhuis, and Y. Wang. "Design and Experimental Validation of Swirl-Recovery Vanes for Propeller Propulsion Systems". In: *AIAA Journal* 56.12 (2018). Publisher: American Institute of Aeronautics and Astronautics _eprint: https://doi.org/10.2514/1.J057113, pp. 4719–4729. ISSN: 0001-1452. DOI: 10.2514/1.J057113. URL: https://doi.org/10.2514/1.J057113 (visited on 04/01/2024).

[28] N. v. Arnhem, R. Vos, and L. L. Veldhuis. "Aerodynamic Loads on an Aft-Mounted Propeller Induced by the Wing Wake". In: *AIAA Scitech 2019 Forum*. _eprint: https://arc.aiaa.org/doi/pdf/10.2514/6.2019-1093. American Institute of Aeronautics and Astronautics, 2019. DOI: 10.2514/6.2019-1093. URL: https://arc.aiaa.org/doi/abs/10.2514/6.2019-1093 (visited on 04/01/2024).

[29] R. Nederlof, D. Ragni, and T. Sinnige. "Experimental Investigation of the Aerodynamic Performance of a Propeller at Positive and Negative Thrust and Power". In: *AIAA AVIATION 2022 Forum*. AIAA AVIATION Forum. American Institute of Aeronautics and Astronautics, June 15, 2022. DOI: 10.2514/6.2022-3893. URL: https://arc.aiaa.org/doi/10.2514/6.2022-3893 (visited on 08/16/2023).

[30] J. Goyal, T. Sinnige, F. Avallone, and C. Ferreira. "Aerodynamic and Aeroacoustic Characteristics of an Isolated Propeller at Positive and Negative Thrust". In: Aug. 2, 2021. DOI: 10.2514/6.2021-2187.

[31] J. Goyal, T. Sinnige, C. Ferreira, and F. Avallone. "Aerodynamics and Far-field Noise Emissions of a Propeller in Positive and Negative Thrust Regimes at Non-zero Angles of Attack". In: June 8, 2023. DOI: 10.2514/6.2023-3217.

[32] R. C. Hibbeler. *Mechanics of materials*. 5th ed. OCLC: 50693383. Upper Saddle River, N.J.: Pearson Education, 2003. 848 pp. ISBN: 978-0-13-008181-0.

[33] S. Burger. *Multi-Fidelity Aerodynamic and Aeroacoustic Sensitivity Study of Isolated Propellers*. 2020. URL: https://repository.tudelft.nl/islandora/object/uuid%3A7abef8ee-c15c-4e36-ade6-33daa3262386 (visited on 04/21/2023).

[34] W. de Haan. *Impact of Blade Sweep on Aerodynamic and Aeroacoustic Performance Optimization of Isolated Propellers*. 2021. URL: https://repository.tudelft.nl/islandora/object/uuid%3A09137b04-f499-47f5-9c17-7334d0ef92ac (visited on 04/14/2023).

[35] T. Keil. *A sensitivity study on the effect of blade sweep on the trade-off between propeller efficiency and noise with panel method analysis*. 2021. URL: https://repository.tudelft.nl/islandora/object/uuid%3A39e67ba0-3409-4069-be3e-f1f12443a9ff (visited on 05/16/2023).

[36] O. Gur and A. Rosen. "Comparison between Blade-Element models of propellers". In: *The Aeronautical Journal* 112 (Dec. 1, 2008), pp. 689–704. DOI: 10.1017/S0001924000002669.

[37] J. D. Anderson. *Fundamentals of Aerodynamics*. Mar. 21, 2016. ISBN: 978-1-259-12991-9. URL: https://www.mheducation.com/highered/product/fundamentals-aerodynamics-anderson/M9781259129919.html (visited on 05/11/2023).

[38] W. F. Phillips and D. O. Snyder. "Modern Adaptation of Prandtl's Classic Lifting-Line Theory". In: *Journal of Aircraft* 37.4 (July 2000). Publisher: American Institute of Aeronautics and Astronautics, pp. 662–670. ISSN: 0021-8669. DOI: 10.2514/2.2649. URL: https://arc.aiaa.org/doi/10.2514/2.2649 (visited on 05/12/2023).

[39] C. Goates and D. Hunsaker. *Practical Implementation of a General Numerical Lifting-Line Method*. Jan. 11, 2021. URL: https://arc.aiaa.org/doi/10.2514/6.2021-0118.

[40] H. Lee, B. Sengupta, M. S. Araghizadeh, and R. S. Myong. "Review of vortex methods for rotor aerodynamics and wake dynamics". In: *Advances in Aerodynamics* 4.1 (May 2, 2022), p. 20. ISSN: 2524-6992. DOI: 10.1186/s42774-022-00111-3. URL: https://doi.org/10.1186/s42774-022-00111-3 (visited on 06/06/2023).

[41] B. Epps and R. Kimball. "Unified Rotor Lifting Line Theory". In: *Journal of Ship Research* 57 (Dec. 1, 2013), pp. 181–201. DOI: 10.5957/JOSR.57.4.110040.

[42] M. Kobayakawa and H. Onuma. "Propeller aerodynamic performance by vortex-lattice method". In: *Journal of Aircraft* (1985). DOI: 10.2514/3.45181. URL: https://arc.aiaa.org/doi/10.2514/3.45181 (visited on 05/04/2023).

[43] D. Ingraham. "Low-Noise Propeller Design with the Vortex Lattice Method and Gradient-Based Optimization". In: AIAA SciTech Forum. NTRS Author Affiliations: Glenn Research Center NTRS Document ID: 20220018313 NTRS Research Center: Glenn Research Center (GRC). National Harbor, MD, 2022. URL: https://ntrs.nasa.gov/citations/20220018313 (visited on 05/04/2023).

[44] C. Burger, R. Hartfield, and J. Burkhalter. "Performance and Noise Optimization of a Propeller using the Vortex Lattice Method and a Genetic Algorithm". In: *48th AIAA/ASME/ASCE/AHS/ASC Structures, Structural Dynamics, and Materials Conference*. Structures, Structural Dynamics, and Materials and Co-located Conferences. American Institute of Aeronautics and Astronautics, Apr. 23, 2007. DOI: 10.2514/6.2007-1883. URL: https://arc.aiaa.org/doi/10.2514/6.2007-1883 (visited on 05/18/2023).

[45] H. Karali, G. Inalhan, M. Demirezen, and M. Yükselen. "A new nonlinear lifting line method for aerodynamic analysis and deep learning modeling of small unmanned aerial vehicles". In: *International Journal of Micro Air Vehicles* 13 (Jan. 1, 2021), p. 175682932110168. DOI: 10.1177/17568293211016817.

[46] F. Farassat. *Derivation of Formulations 1 and 1A of Farassat*. L-19318. NTRS Author Affiliations: NASA Langley Research Center NTRS Document ID: 20070010579 NTRS Research Center: Langley Research Center (LaRC). Mar. 1, 2007. URL: https://ntrs.nasa.gov/citations/20070010579 (visited on 05/22/2023).

[47] F. B. Metzger. *A review of propeller noise prediction methodology: 1919-1994*. NASA-CR-198156. NTRS Author Affiliations: Metzger Technology Services NTRS Document ID: 19960008819 NTRS Research Center: Legacy CDMS (CDMS). June 1, 1995. URL: https://ntrs.nasa.gov/citations/19960008819 (visited on 05/24/2023).

[48] M. T. Kotwicz Herniczek, D. Feszty, S.-A. Meslioui, J. Park, and F. Nitzsche. "Evaluation of Acoustic Frequency Methods for the Prediction of Propeller Noise". In: *AIAA Journal* 57.6 (2019). Publisher: American Institute of Aeronautics and Astronautics _eprint: https://doi.org/10.2514/1.J056658, pp. 2465–2478. ISSN: 0001-1452. DOI: 10.2514/1.J056658. URL: https://doi.org/10.2514/1.J056658 (visited on 05/22/2023).

[49] O. A. Bauchau and J. I. Craig. "Euler-Bernoulli beam theory". In: *Structural Analysis*. Ed. by O. A. Bauchau and J. I. Craig. Solid Mechanics and Its Applications. Dordrecht: Springer Netherlands, 2009, pp. 173–221. ISBN: 978-90-481-2516-6. DOI: 10.1007/978-90-481-2516-6_5. URL: https://doi.org/10.1007/978-90-481-2516-6_5 (visited on 05/23/2023).

[50] F. Möhren, O. Bergmann, F. Janser, and C. Braun. "On the influence of elasticity on propeller performance: a parametric study". In: *CEAS Aeronautical Journal* (Mar. 21, 2023). ISSN: 1869-5590. DOI: 10.1007/s13272-023-00649-y. URL: https://doi.org/10.1007/s13272-023-00649-y (visited on 04/11/2023).